THE UNIVERSITY OF CHICAGO

MOLECULAR ENGINEERING OPTICALLY ADDRESSABLE SPIN QUBITS

A DISSERTATION SUBMITTED TO
THE FACULTY OF THE PRITZKER SCHOOL OF MOLECULAR ENGINEERING
IN CANDIDACY FOR THE DEGREE OF
DOCTOR OF PHILOSOPHY

BY
PETER JAMES MINTUN

CHICAGO, ILLINOIS
DECEMBER 2022

To Catie, without whom none of this would have been possible.

CONTENTS

LIST OF FIGURES

LIST OF TABLES

ACKNOWLEDGMENTS

The saying “it takes a village” certainly holds true for a PhD, and I am indebted to many people for helping me make it out to the other end.

First, I would like to acknowledge my advisor, David Awschalom for his unwavering support of our research and for cultivating an incredible lab of scientists. The molecular spins project was always going to be bold and ambitious, and David continued supporting us through essentially two years of failure or null results. In addition, he deserves credit for assembling an exceptional group of not only fine scientists, but also great people, who I was fortunate to count not as just colleagues but also friends over the years. Outsiders have observed that that our group is often “somewhat cult-like”, but a more straightforward explanation is that we genuinely enjoy each others’ company. I have greatly missed both the (often absurd) lunch discussions covering myriad topics, and whiteboard sessions to discuss both interesting physics or experimental concepts.

Second, I would like to acknowledge now-Professor Sam Bayliss for his outstanding mentorship working together on the molecules project. In addition to teaching many of the practical lab skills, Sam imparted a wealth of knowledge on many topics, spanning molecular photophysics to the finer points of British culture (“banter” and “cheeky Nando’s”, for example). Through his mentorship, I was able to develop into a “good” scientist, from merely okay before. Sam was instrumental in leading the UChicago end of the broader molequles project alongside others in our group such as Berk Diler, Leah Weiss, Pratiti Deb, and Benjamin Soloway. The molecules project would of course not have been a success without our chemistry counterparts from the Freedman Group at Northwestern (and now MIT). I am grateful for their willingness to jump in on this ambitious effort with both feet, for entertaining us on our visits to Northwestern’s campus / Coffee Lab / Tomate, for their patience in bridging the gap between spin physics and chemistry, and for synthesizing just about any compound we could dream of. Majed Fataftah was a pioneer in early experiments and did much of the initial thinking on molecular design, Dan Laorenza was instrumental in making the Cr^{4+} work a success, and others like Kelsey Collins and Mikey Wojnar

supported many other efforts to try and develop optically-addressable compounds beyond those mentioned in this thesis.

Partially a consequence of taking too long to finish my PhD, I had the good fortune of interacting with several generations of graduate students and postdocs who brought light to our group:

1. The UCSB old guard: Will Koehl (who is due credit for making our first efforts in molecular spins), Andrew Yeats (who mentored me when I joined the group), Christopher Yale, David Christle, Paolo Andrich, Charles des las Casas, Paul Klimov, Abram Falk, and Joe Heremans

2. My generation: Chris Anderson, Kevin Miao, Alexander Crook, Berk Diler, and Sam Whiteley

3. The next generation: Alexandre Bourassa, Paul Jerger, Masaya Fukami, and Erzsebet Vincent

4. And the folks following: Pratiti Deb, Elena Glen, Joseph Blanton, Grant Smith, Jonathan Karsch, Cyrus Zeledon, Benjamin Soloway, and Jacob Feder

I also benefitted from overlapping with a number of talented postdocs who brought best scientific practices and knowledge to our group: Sam Bayliss, Leah Weiss, Gary Wolfowicz, Brian Zhou, Yeghishe Tsaturyan, Nazar Delegan, Sean Sullivan, and Joost van Bree. Finally, I was fortunate to work with a number of talented undergraduates, all of whom have gone on to even greater things: Darius Choksy (whom I had the good fortune of mentoring), Hope Bretscher, Agnetta Cleland, Hope Lee, Marie Wesson, Seung Hwan Lee, and Michael Haas.

I would like to thank many of the folks who worked tirelessly, often behind the scenes, to keep the wheels on the research train at PME. In addition to their great works during normal times, the COVID-19 pandemic introduced many unique and unprecedented challenges, and these folks were able to smooth out the shocks and disruption. I am deeply grateful to the stellar staff in ERC like Mary Pat McCullough, Amanda Dennis, and Diana Morgan on the administrative end; Paul Julson and Jennifer Robles from facilities; Maurice Perry, Marco Calderon, Oscar Hernandez, and Joshua

Lopez from the dock; Peter Duda and Sally Wolcott (who sadly, has since passed) from the PNF; and finally Kimberly Mormann (also unfortunately passed) and Krista Dillingham from research safety.

Additionally, I would like to thank my now-colleagues at ARCH Venture Partners, namely Keith Crandell, Sean Kendall, Corey Ritter, Nilay Thakar, and Reetika Bhardwaj, who provided insights that contributed to the scientific and commercial outlook presented in this work.

Finally, I would like to thank my parents Mike and Sony, my brother Michael, grandma, grandpa, and Sundri for their support during the bumps in the road along the way. Having gotten married during this process, I have also been fortunate to bring the Isroff family in as well: Brian, Louise, Ben, Noah, and Briana (soon-to-be family). Most of all, I am forever indebted to my wife Catie, without whom none of this would have been possible. She has always been able to pick me up after days (or months!) of failed experiments in the lab or to take away doubts I had about my ability to make it through. I am truly blessed to have her as my life partner and could not imagine going through this chapter of my life without her.

ABSTRACT

The field of quantum information processing aims to leverage the unique physics of quantum mechanics to develop new strategies for applications such as computation, communications, and sensing. Two subfields have emerged as compelling platforms: (i) optically-addressable defect spins in the solid-state (which offer an optical interface, but limited chemical control) and (ii) molecular spin qubits (which offer chemical control, but lacked an optical interface). In this thesis, we aim to extend the optical spin initialization and readout schemes developed for spin defects in solid-state crystals to the class of chemically-synthesized molecular spin qubits.

We begin by providing a brief historical context on motivations for the field of quantum information, and highlight a few parallel developments within the fields of optically-addressable defect spins and molecular spin qubits. In Chapter 2, we provide theoretical background on the electronic strucutre of metal ions in solids and organometallic coordination complexes, and discuss considerations specific to the cases of both the transition metal and lanthanide series. By doing so, we aim to build an intuitive picture to model the electronic structure of the ground and first few excited states of these metal ion systems in distinct chemical environments. In Chapter 3, we discuss the temporal dynamics of these systems, briefly covering both molecular photophysics and spin dynamics, with the aim of outlining the necessary conditions to develop a spin-photon interface for molecules.

Next, we present experimental results that deliver on our objective of creating optically-addressable molecular spin qubits. Chapter 4 presents optical initialization and readout of an ensemble of Cr^{4+} molecular spins through a spin-selective optical pumping scheme, which represents the first (to our knowledge) optical readout of a molecular ground state spin qubit. Additionally, we show that this strategy applies to multiple compounds, and that chemical design allows control of the intrinsic spin properties. Chapter 5 covers our efforts to develop an off-resonant readout scheme for these tetravalent chromium complexes, which leverages polarization selection rules to yield spin-selective pumping. Finally, Chapter 6 discusses a strategy to push down to the single spin

level, outlining an approach by which single molecular Ce^{3+} spins could be probed optically via polarization selection rules.

Finally, we conclude by discussing general outlook on unique opportunities that optically-addressable molecular spins might present, and suggest future research directions that may prove fruitful.

CHAPTER 1

INTRODUCTION

In this chapter, I aim to offer a broader perspective on the evolution of the field of quantum information and quantum technologies. I discuss the first generation of quantum technologies and the broad range of applications that have been enabled due to innovations in these areas. Next, I discuss our current era: the "second quantum revolution" where we aim to control these quantum phenomena down to the single particle limit and gain access to new phenomena, such as entanglement.

1.1 Quantum Technologies and Applications

Quantum information processing has attracted significant theoretical and experimental interest ever since proposals for quantum computation in the early 1980s [1,2]. There is now significant interest in commercializing quantum technologies based on application of the principles of quantum physics. In addition, this has led to considerable discussion over when (and even if) quantum technologies will be useful or commercially viable [3–5]. I would argue, however, that these technologies are merely the continuation of a history of successful innovation based on quantum phenomena, such as magnetic resonance imaging, atomic clocks, lasers, quantum materials, and semiconductor technologies [6] which are based on quantum phenomena at the ensemble level. These "Quantum 1.0" technologies have already introduced substantial societal benefits and applications far outside the scope anticipated by their original inventors. The second generation of quantum technologies aims to extend our control over these phenomena down to the single particle limit, where additional phenomena such as entanglement offer additional features. I anticipate that the next generation of quantum technologies will bear similar fruit, enabling a variety of applications well beyond those anticipated today in the long term.

1.1.1 Quantum 1.0 Technologies - quantum phenomena at the ensemble level

The first generation of quantum technologies described above typically rely on discretized phenomena: charges, energy levels, and transitions, but at the ensemble level. For example, in nuclear magnetic resonance (NMR) / magnetic resonance imaging, we drive transitions between nuclear spin sublevels of large ensembles of nuclei. Although spin is inherently a quantum variable, we can think about these processes semi-classically, as they average over a macroscopic number of particles. A similar argument could be made to describe lasers, where stimulated emission drives coherent emission of a macroscopic number of emitters, or integrated circuits, where macroscopic numbers of dopants introduce additional electrons or holes shared within the host material.

These ideas once existed merely on paper, but several decades of scientific innovations and economic improvements have pushed many of these into relatively mature technologies. Dramatic cost reductions through miniaturization [7] and accumulated experience [8] have been crucial to democratizing these technologies and opening secondary and tertiary applications far beyond the vision of their early inventors. As an example, lasers now power a diverse range of technologies, such as high-throughput gene sequencing [9], fiber-optic communications [10], and advanced manufacturing [11], none of which would have been anticipated at the time of their invention.

1.1.2 Quantum 2.0 Technologies - pushing down to the single particle limit

The next generation of quantum technologies currently in development are focused on pushing these quantum phenomena down to their natural limits: that of the single particle. Pushing down to this limit is crucial to harness emergent phenomena such as quantum entanglement, where the state of several individual particles exhibit non-separable correlations. In particular, generating high-dimensionality entangled systems, spatially distributed entanglement, and long-lived coherence are key pieces for applications such as quantum computation, quantum communications, and quantum sensing. To this end, a variety of platforms have emerged as potential building blocks for quantum technologies, such as superconducting circuits [12,13], isolated ions [14] or atoms [15], optical photons [16], acoustic modes [17,18], and charges or spins in the solid state [19]. Several of these

systems are beginning to reach interesting regimes where they may become challenging to simulate classically [20,21]. In addition, improvements in our control of quantum systems at this level have led to advances in our ability to distribute entanglement between spatially-separated systems, now up to macroscopic distances [22,23]. Continued advances will extend early demonstrations in areas such as quantum simulation of materials [24], quantum networks [25], and quantum sensing [26] beyond the reach of classical technologies.

1.2 Spin qubits in semiconductors

One platform for second generation quantum technologies that has emerged is spin qubits in semiconductors. Ever since Bloch's work on nuclear spins in 1946 [27], and the discovery of the spin echo by Hahn in 1950 [28], we have known that spins in the solid state can have potentially very long relaxation times and have been able to develop strategies to protect spins against relaxation due to their local environment. Early experiments were based on electron spin resonance, which probes a thermal polarization of a large spin ensemble ($\sim 10^{13}$ spins/$\sqrt{\text{Hz}}$). During the experiment, microwave pulses coherently drive magnetic dipole transitions when the microwave frequency is resonant with the energy splitting between the spin sublevels, and the state of the macroscopic spin ensemble can be sensitively determined by measuring the coupling between the spin ensemble and a resonant cavity. This method, known as electron spin resonance, can be used to study the properties of unpaired electron spins (and transient radical species) in a broad range of materials and molecular systems. Initial studies of spin relaxation in solids aimed to better understand the underlying mechanisms of relaxation and the interaction between paramagnetic centers and their host materials. However, the emergence of the quantum information field has motivated the development of strategies to preserve and extend spin coherence. However, as these experiments rely on measuring a Boltzmann polarization of spins, they typically lack the ability to probe single spins. Techniques such as single electron transistors [29] and scanning tunneling microscopy [30] have reached the single spin limit, but optical detection provides a straightforward strategy to address and control individual spins.

1.2.1 Optically addressable spins in semiconductors

Though a plethora of defects in semiconductors exist, only a subset have optical activity and emit luminescence. These systems are known as color centers, and the emitted luminescence serves as a spectroscopic fingerprint characteristic of the defect. Even fewer defects in semiconductors have luminescence that depends on the spin state of the electrons localized to the defect. This spin-dependent luminescence provides additional information, as the energy splittings of the spin sublevels can be measured directly through optically detected magnetic resonance (ODMR) [31], providing additional insights into the electronic structure of the system. These optically addressable spins offer several key features. First, the optical interface provides a handle which can be used to both initialize and readout the spin state, a key requirement for quantum technologies. Second, this interface pushes the detection signal into the optical domain, where thermal noise is substantially reduced (compared to the spin-only energy level splittings which usually lie in the microwave or millimeter-wave regime). Third, individual spins can be selectively addressed using frequency-selective or spatially selective methods) using conventional microscopy techniques. These features in conjunction enabled the first experimental demonstration of optically-detected magnetic resonance (ODMR) at the single (ground state) spin limit [32] for negatively-charged nitrogen vacancy (NV^-) centers in diamond, opening proposals to use these systems for quantum sensing or information processing.

Since this first demonstration, optical interfaces for a variety of spins in semiconductors have been developed and engineered. In addition to providing a mechanism to address single spins, the optical interface of some spin qubits has introduced some interesting novel applications such as remote entanglement [33] and all-optical sensing [34,35]. In addition, significant work is ongoing towards identifying candidate materials and defect structures that might support long-lived spins with a suitable optical interface [36,37]. In particular, optical initialization and readout has been performed for transition metals in semiconductors, such as Cr:SiC [38], Mo:SiC [39], and V:SiC [40]. Transition metals are an attractive platform for quantum science, as their d-orbitals are well-isolated from the environment, which gives them electronic properties that are largely con-

sistent across different host materials. One limitation of this approach, however, is the electronic structure of these systems cannot be controlled – the crystal lattice provides a high-symmetry local environment, and the limited number of transition metals and viable solid state matrices limits the scope of what can be reasonably explored.

Optically addressable rare earth ions in solids have been similarly explored for quantum information applications. These systems have extremely well screened $4f$-wavefunctions and can host nuclei with extraordinarily long-lived spin coherence [41]. However, these systems do not interact strongly with light, as most systems only have $4f - 4f$ magnetic dipole transitions with long radiative lifetimes. To reach the single spin limit, the radiative lifetime can be decreased through Purcell enhancement [42] or by considering electric dipole allowed $4f \rightarrow 5d$ transitions [43,44]. Even so, the phase space of potential optically addressable spins in solids remains largely unexplored, and the ability to design and engineer these systems is limited. In this work, we aim to create a framework to develop molecular analogs of various optically addressable spins. These systems can be readily engineered through synthetic chemistry, and in principle can be adapted to different material device platform architectures.

1.3 Molecular quantum systems

This molecular approach to quantum information is not really a new idea: molecular systems were one of the first proposed platforms for quantum computing with early developments in the field of nuclear magnetic resonance (NMR) quantum computing [45–47]. NMR quantum computers offered several appealing properties, namely:

1. Nuclear spins are well-isolated from environmental noise and have slow relaxation rates
2. Ability to scale to larger number of qubits through controllable molecular structures
3. Ability to control and measure specific nuclear spins via frequency-selective methods

In addition, the relative maturity of NMR technology made it a prime system for initial demonstrations. These advantages allowed NMR quantum computing to be used for the first proof-of-

concept demonstration of Grover's search [48] and Shor's algorithm [49]. A major limitation of NMR quantum computing, however, is the absence of an efficient initialization and readout mechanism. As a result, the nuclear spins cannot be initialized and read out at the single spin limit, and therefore experimental realizations typically probe a thermal ensemble average, rather than a pure state [50]. Scaling the number of qubits becomes problematic, as eventually qubits in thermally excited states dominate the signal. These initial efforts were successful, however, in motivating a chemical approach to building quantum information systems, and additional fields such as single molecule quantum optics and molecular spin qubits have emerged to push some of these ideas further.

1.3.1 Molecular spin qubits

The subfield of molecular spin qubits has grown as a means to study the impact of material design on spin coherence in a more systematic way. A variety of experiments have demonstrated how molecular design can be used to extend the coherence time for molecular spins and tailor their properties accordingly [51–53]. In addition, in the spirit of NMR quantum computing, molecular qubits can be scaled up into larger registers hosting individually addressable qubits [54], or into ordered arrays of spins [55,56], through chemical synthesis.

In addition to ground state electron spin resonance, the properties of excited state molecular spins have been widely studied in the context of molecular spectroscopy and optoelectronics. In fact, the first optically detected magnetic resonance experiments to reach the single spin limit were performed at cryogenic temperatures [57,58] on the triplet excited state of pentacene (predating the measurement of individual NV^- centers by several years)! However, an optical interface for ground state spin qubits had remained elusive. The ground state portion is particularly crucial for quantum information, as decay out of molecular excited states poses a fundamental limitation on many information processing and sensing schemes.

1.3.2 Single molecule quantum optics

Finally, the field of single molecule quantum optics provides some interesting context for our work as well. Several experimental works have shown that molecular systems can match many of the physical properties of solid state emitters: lifetime limited emission [59] and photon indistinguishability [60,61]. In addition, these systems can be readily integrated into plasmonic [62], nanophotonic [63] or electronic devices [61]. Our work has focused primarily on designing molecular systems with long-lived spins in order to realize a spin photon interface, but future work will likely also focus on improving the quality of the optical interface. For example, improvements such as eliminating sources of spectral diffusion or broadening, tailoring the far field emission through coupling with photonic structures, and increasing the radiative efficiency of our complexes should all be possible. Thus, we anticipate that optically addressable molecular spins may be a feasible platform for the range of applications currently targeted by their solid-state cousins.

1.4 Overview of this thesis

This thesis aims to bridge the gap between the realm of optically addressable spins in semiconductors and molecular spin qubits. Specifically, we aim to extend methods to optically initialize and readout spins to molecular systems and demonstrate that this approach introduces novel functionality and potential advantages. In Chapter 2, we discuss in greater detail the electronic structure of the transition metal and rare earth ions investigated in this work. To inform the design of new optically-addressable molecular spins, we provide a general overview of the principles that determine the electronic structure of metal-organic complexes and how their properties can be tuned through synthetic chemistry. We then specialize to discuss the electronic structure of tetrahedrally-coordinated Cr^{4+} ions and Ce^{3+} molecular complexes. Chapter 3 provides an general overview of molecular photophysics and spin relaxation. We then blend these two disciplines to outline the criteria necessary to implement a viable spin-photon interface. Next, we specialize to discuss

spin-photon interfaces in tetrahedrally-coordinated Cr^{4+} ions and Ce^{3+} molecular complexes in greater detail.

In Chapter 4, we present the first (to our knowledge) experimental demonstration of an optical interface for molecular spin qubits. We use a spin-selective optical pumping technique to optically initialize and readout an ensemble of molecular Cr^{4+}. Furthermore, we show that atomistic changes to the ligands coordinating the metal center allow tunability of the optical and spin properties of the qubit, introducing a novel degree of control unavailable to defect centers in semiconductors. Chapter 5 outlines our experimental efforts towards off-resonant initialization and readout of a Cr^{4+} molecular spin system. Chapter 6 discusses our approach to push towards the single spin limit by designing optically addressable molecular spin complexes based on $4f \rightarrow 5d$ transitions in trivalent Cerium complexes.

Finally, in Chapter 7, we discuss our conclusions and outlook for future developments in the field.

CHAPTER 2

ELECTRONIC STRUCTURE OF METAL ION COMPLEXES

In this section, we outline the electronic structure of transition metal and rare earth ions in solids and organometallic complexes, attempting to provide a unified framework to describe these two classes of materials. We start with a general discussion to inform future efforts to design transition metal and rare earth ion complexes with specific spin and optical properties. We first discuss the free metal ion in isolation and how combinatorial considerations lead to the emergence of spectral multiplets with distinct quantum numbers. Next, we outline the various terms in the Hamiltonian for a metal ion within the framework of crystal field theory. Having outlined the various interactions, we separate our discussion into two specific cases to account for the transition metal and rare earth series respectively. For the transition metal ion case, we discuss how the introduction of a lower symmetry ligand field splits these spectral multiplets. We also discuss the role of hybridization between the bonding ligands and metal center in determining the electronic properties of these complexes. Finally, we conclude with discussion of the rare earth ion case, where strong spin-orbit coupling splits the energy levels into distinct J multiplets, which are then weakly split by interaction with the ligand field.

The purpose of this chapter is to provide a practical guide for thinking about and computing the electronic structure of mononuclear metal-organic complexes. This can be broken down into roughly the following recipe:

1. Determine all valid (i.e. obeying Pauli exclusion) configurations of n electrons put into $2l+1$ orbital and $\uparrow / \downarrow$ spin configurations.

2. Decompose these configurations into $|\nu SL\rangle$ atomic terms.

3. Determine the Coulomb interaction between these $|\nu SL\rangle$ terms.

4. Next, our procedure changes for the transition metals and lanthanides, respectively:

1st and second row transition metals	Lanthanides
Apply high-symmetry ligand field to $\|vSL\rangle$ multiplets	Determine $\|vSLJ\rangle$ multiplets. Split based on spin-orbit interaction
Reduce symmetry add SOC	Apply crystal field to $\|vSLJ\rangle$ multiplets

5. Apply Zeeman splitting based on **B**.

Though the first / second row transition metal and lanthanide series are often discussed separately and by different research communities, their physics are largely determined by the same interactions, just in different parameter regimes. Thus, we hope that this guide can provide a unified framework to design molecular complexes based on these ions.

2.1 Theoretical background

Starting with the seminal paper outlining the crystal field theory by Hans Bethe in 1929 [64], significant theoretical and experimental work has been performed to understand the properties of metal ions in crystalline solids and metal-organic complexes. We start with a brief outline of the crystal field theory as an approximate model for the electronic structure of transition metal and rare earth metal-organic complexes. One of the central assumptions of crystal field theory is that the outermost shell of the metal ion is only partially filled, and these outermost electrons do not significantly interact with the coordinating ligands (with the valence electrons responsible for bonding). Thus, the electronic structure is determined by the different electronic configurations of these outer shell electrons. For the case of first/second row transition metal (rare earth) ions, the outermost shell is comprised of $3d/4d$-electrons ($4f$-electrons). Thus we consider electron states of the form $[Ar]3d^n$ /[Kr]$4d^n$ / [Xe]$4f^n$ respectively. By considering possible configurations of these electrons into distinct spin-orbitals (subject to the Pauli exclusion constraint), we can determine the approximate electronic structure for a given system. Crystal field theory builds up the the multi-electron wavefunction by recursively coupling the nth electron to a system of $n-1$ electrons, that is $\Psi_n = \psi_n \otimes \Psi_{n-1}$.

2.1.1 Free ion case

To start, we neglect the ligands and consider just the free ion in isolation. In this situation, each of the $d-$ ($f-$) orbitals are degenerate.

Depending on the specific metal center and the oxidation state of the metal ion, we are now responsible for placing n electrons into these orbitals. For a given value of orbital angular momentum l, there are $2l+1$ possible microstates (i.e. $-l, -l+1, ..., l-1, l$). In addition to orbital occupation, we are also free to choose the spin state of each electron, so an individual electron is free to be placed in $2(2l+1)$ possible spin-orbitals. However, all valid configurations are constrained by the Pauli exclusion principle, whereby we cannot put two electrons into identical orbital and spin states. Thus, the number of valid atomic microstates is given by [65]:

$$N_{\text{microstates}} = \begin{pmatrix} N_{SO} \\ n \end{pmatrix} = \frac{N_{SO}!}{n!(N_{SO}-n)!} \tag{2.1}$$

where $N_{SO} = 2(2l+1)$ = 10 (14) is the number of possible spin-orbitals for d (f) electrons, n is the number of outer shell electrons, and $\begin{pmatrix} N_{SO} \\ n \end{pmatrix}$ is the binomial coefficient (i.e. "N_{SO} choose n").

For a given microstate, we can compute the orbital angular momentum $M_L = \sum_i m_{l,i}$ and spin angular momentum $M_s = \sum_i m_{s,i}$ where the summation runs over all electrons in the microstate. The complete set of microstates can then be decomposed into a set of atomic terms with quantum numbers L and S using the procedure outlined by [66]. For complexes with larger numbers of electrons, there is an additional complication introduced by the existence of multiple terms with the same values of L and S, which are then distinguished by the Racah seniority parameter v.

Though this procedure may at first seem abstract, we discuss it in more detail for a few reasons. First, this decomposition reduces the complexity of a multi-electron wavefunction into a set of interacting effective atomic terms. Second, this simple model can predict electronic properties of these compounds, and the system behavior under various perturbations, such as ligand fields,

Electron configuration	M_L, M_S	Valid atomic terms
$m_l=-2$ $m_l=-1$ $m_l=0$ $m_l=+1$ $m_l=+2$	$M_L=+3, M_S=+1$	${}^3F(L=3,S=1)$
$m_l=-2$ $m_l=-1$ $m_l=0$ $m_l=+1$ $m_l=+2$	$M_L=-4, M_S=0$	${}^1G(L=4,S=0)$
$m_l=-2$ $m_l=-1$ $m_l=0$ $m_l=+1$ $m_l=+2$	$M_L=0, M_S=0$	${}^1G, {}^1D, {}^1S$
$m_l=-2$ $m_l=-1$ $m_l=0$ $m_l=+1$ $m_l=+2$	$M_L=0, M_S=0$	${}^3F, {}^3P, {}^1G, {}^1D, {}^1S$

Figure 2.1. Example of various two-electron configurations of $d-$orbitals.

spin-orbit coupling, or magnetic fields. As an example, Hund's rule prescribes that the lowest energy atomic term maximizes the total spin angular momentum S and then the total orbital angular momentum L. Finally, this procedure is sufficiently general and explains the properties of the first and second row transition metals and the lanthanide series with relatively few free parameters, making it a useful framework for the design of metal-organic complexes.

2.1.1.1 Cr^{4+} case

Our prior discussion has focused on the general considerations for transition metal and rare earth ions in solids and metal-organic complexes without regard to any specific complex. A significant portion of this thesis will cover Cr^{4+} complexes, so we specialize to discuss this example in more detail here. Chromium is a transition metal, and the $4+$ oxidation state implies that $n=2$. Thus, we need to consider configurations of two d electrons (each with $l=3 \rightarrow m_l: -3,...,+3$ and $s=1/2 \rightarrow m_s=-1/2(\downarrow),+1/2(\uparrow)$). We depict a few of these possible microstates in Figure 2.1.

Using Equation 2.1, we can calculate that there are 45 possible electronic configurations for an $n=2$ transition metal. These can be decomposed into the atomic multiplets: ${}^3F$, ${}^3P$ (spin triplet), and ${}^1D, {}^1G, {}^1S$ (spin singlet). By Hund's rule, the ground state (in the free ion case) originates from a ${}^3F$ atomic multiplet as it has the maximal S and maximal L for that value of S. Later on in this

	Relative interaction strengths	Prescription
1st/2nd transition series Sc - Zn, Y - Cd	$H_{\text{Coulomb}} \approx H_{\text{LF}} > H_{\text{SO}}$	(Free ion $\leftrightarrow$ strong field) $\rightarrow$ Spin orbit $\rightarrow$ Zeeman
Lanthanides La - Lu	$H_{\text{Coulomb}} > H_{\text{SO}} > H_{\text{LF}}$	Free ion $\rightarrow$ J multiplets $\rightarrow$ Ligand field $\rightarrow$ Zeeman
Actinides Ac - Lr	$H_{\text{Coulomb}} \gtrsim H_{\text{SO}} \gtrsim H_{\text{LF}}$	Exercise for the reader (?)
3rd transition series Hf - Hg	$H_{\text{Coulomb}} \approx H_{\text{LF}} \approx H_{\text{SO}}$	

Table 2.1: Relative interaction strengths by metal series.

chapter, we will compute the splitting of these atomic terms and their response to the perturbation of the ligand field of the metal ion complex.

2.2 Hamiltonian for d^n and f^n ions

In this section, we discuss the various interaction terms relevant for determining the electronic structure of metal ion complexes. Following the discussion of [67], we take a step back to consider the relative strengths of interactions for different classes of metal ions, as these relative strengths determine which interactions are dominant, and which can be treated perturbatively. We outline the rough interaction strengths in Table 2.1.

The first and second transition metal series are characterized by a Coulomb interaction strength comparable to the ligand field. For this reason, we must consider two limiting cases: the weak field, where the ligand field acts as a small perturbation to the Coulomb-split free ion states, and the strong field, where the ligand field dominates over the Coulomb interaction.

In contrast, the lanthanides are actually in some ways more straightforward. The strong spin-orbit interaction acts to split the $|\nu SL\rangle$ multiplets into distinct J manifolds. Thus, the total angular momentum $J = L + S$ is the natural multiplet to consider for the free ion case. In addition, the ligand field strength becomes significantly weaker relative to the transition metal ion case. As a result, the J manifolds are then split perturbatively by the ligand field interaction.

For the actinides and third transition metal series, the situation becomes much more complicated as these different interactions become comparable in strength.

2.2.1 Spherical tensor formalism

One of the most useful assumptions made by the ligand field theory is the separability of the electronic wavefunctions into radial and angular components:

$$\Psi(r,\theta,\phi) = \psi_{radial}(r)\psi_{\text{angular}}(\theta,\phi) \tag{2.2}$$

Often, the strength of various interactions can be encapsulated into an experimental parameter, which takes into account the radial dependence of the interaction (for example, the Racah parameters, Slater-Condon parameters, or spin-orbit coupling constant). These parameters depend on the radial density function for a particular ion, but remain fairly consistent between complexes of the same ion. The angular dependence can be calculated directly using the theory of spherical tensor operators, allowing for a semi-quantitative understanding of the impact of different perturbations. Performing these calculations in practice, however, introduces several pitfalls which I outline here. There are several different quantum numbers that must be accounted for (and not confused inadvertently!). These quantum numbers are outlined in Table 2.2.

In addition, it is important to know which basis is the "correct" one to use for the computations, as the correct choice of basis is helpful for an intuitive physical interpretation of results. For the first and second transition row metals, we work in the $|\nu SLM_S M_L\rangle$ basis, where the total *orbital* magnetic quantum number M_L, and total *spin* magnetic quantum number M_S are good quantum numbers. For the lanthanides, the spin-orbit coupling means that M_L and M_S are not good quantum numbers, so we work in the $|\nu SLJM_J\rangle$ basis, where we instead have *total* angular momentum J and *total magnetic* quantum number M_J.

Having outlined the different quantum numbers and bases, to understand the interactions between various states, we will need to compute matrix elements of the form: $\langle \nu\, jm_j|T_q^{(k)}|\nu'\, j'm_j'\rangle$,

	Quantum number	Description	Note
Multi-electron atomic	n	Number of electrons (holes)	N (less than half-filled); $2(2l+1)-N$ holes (more than half-filled)
	ν	Racah seniority parameter	Label to differentiate between atomic terms with same $\|SL\rangle$ values
	S	Total spin angular momentum	
	M_S	Total spin magnetic number	$M_S : -S, -S+1, ..., S-1, S$
	L	Total orbital angular momentum	
	M_L	Total orbital angular momentum magnetic number	$M_L : -L, -L+1, ..., L-1, L$
	J	Total angular momentum	$\|L-S\| \leq J \leq \|L+S\|$
	M_J	Total angular momentum magnetic number	$M_J : -J, -J+1, ..., J-1, J$
Single-particle	$s = 1/2$	Electron spin quantum number	
	m_s	Single particle orbital angular momentum magnetic number	$m_s : -1/2(\downarrow), +1/2(\uparrow)$
	l	Electron orbital angular momentum	d-orbital: $l = 2$ f-orbital: $l = 3$
	m_l	Single particle orbital angular momentum magnetic number	$m_l : -l, -l+1, ..., l-1, l$

Table 2.2: Quantum numbers for metal ions.

where a spherical tensor operator $T_q^{(k)}$ acts on some angular momentum eigenstates $\langle jm_j|$ and $|j'm'_j\rangle$. Although this seems initially daunting, the Wigner-Ekart theorem allows these matrix elements to be calculated efficiently:

$$\langle \nu jm_j|T_q^{(k)}|\nu' j'm'_j\rangle = (-1)^{j-m_j} \begin{pmatrix} j & k & j' \\ -m_j & q & m'_j \end{pmatrix} \underbrace{\langle \nu j|T^{(k)}|\nu' j'\rangle}_{\text{reduced matrix element}} \tag{2.3}$$

where $\begin{pmatrix} j & k & j' \\ -m_j & q & m'_j \end{pmatrix}$ is the Wigner $3j$ symbol and $\langle \nu j|T^{(k)}|\nu j'\rangle$ is the reduced matrix element of the tensor operator $T^{(k)}$. Note that in this case, j/m_j and j'/m'_j refer to a generic angular momentum state (e.g. L, S, or $J = L+S$) that the tensor operator $T_q^{(k)}$ acts on, and ν/ν' account for any additional quantum numbers unaffected by the action of the tensor operator $T^{(k)}$. The value of this theorem comes from the fact that once the reduced matrix element $\langle \nu j|T^{(k)}|\nu' j'\rangle$ (which

may be hard to calculate) is obtained, all components of the operator can be calculated directly. This theorem also has a more intuitive interpretation: by applying the selection rules inherent to the $3j$ symbol (most importantly, that $-m_j + q + m_{j'} = 0$), the various tensor operator components that will act on a state can be seen directly. To show the value of this framework, we present a more concrete example of this type of calculation in Section 2.2.3.

There are a few important reduced matrix elements that we use in our analysis, which we present briefly. These are tabulated directly by [68], but can also be calculated given the coefficients of fractional parentage tabulated in the same reference. For a more pedagogical introduction to a variety of spherical tensor operators, and the derivation of these reduced matrix elements, we refer the reader to Chapter 2 of [69].

The unit tensor operator of order k, $\mathbf{U}^{(k)}$ acts on the total orbital angular momentum L and arises in computations of the crystal field interaction (and also the Coulomb interaction, in some cases). The reduced matrix elements of the kth-order orbital unit tensor operator $\mathbf{U}^{(k)}$ are given by [70]:

$$\begin{aligned}\langle l^n \nu LS|\mathbf{U}^{(k)}|l^n \nu' L' S'\rangle &= n\delta_{S,S'}\sqrt{(2L+1)(2L'+1)} \\ &\sum_{\nu_1,L_1,S_1} (G^{n,\nu,L,S}_{n-1,\nu_1,L_1,S'_1})^* (G^{n,\nu,'L',S'}_{n-1,\nu'_1,L'_1,S'_1})(-1)^{L_1+L+l+k} \begin{Bmatrix} L & L' & k \\ l & l & L_1 \end{Bmatrix}\end{aligned} \tag{2.4}$$

where the summation runs over the parent states of the n electron states $|n\nu LS\rangle$ and $|n\nu' L' S'\rangle$, $G^{n,\nu,L,S}_{n-1,\nu_1,L_1,S'_1}$ and $G^{n,\nu,'L,'S'}_{n-1,\nu_1,L_1,S'_1}$ are the coefficients of fractional parentage (as tabulated by [68]), and $\begin{Bmatrix} L & L' & k \\ l & l & L_1 \end{Bmatrix}$ is the Wigner $6-j$ symbol. Note that the $\delta_{S,S'}$ term implies that this interaction exists only between states with the same total spin angular momentum S (i.e. it is spin-conserving). Our next ingredient for these calculations is the reduced matrix element for the k-th order Racah operator $\langle l|\mathbf{C}^{(k)}|l\rangle$, which is used in computation of the crystal field interaction (where it acts on the total angular momentum L) as well as the Coulomb interaction (where it acts on the single

particle angular momentum):

$$\langle l|\mathbf{C}^{(k)}|l'\rangle = (-1)^l \sqrt{(2l+1)(2l'+1)} \begin{pmatrix} l & k & l' \\ 0 & 0 & 0 \end{pmatrix}. \tag{2.5}$$

Finally, in computation of the spin-orbit coupling, we have the spin-orbit tensor operator $\mathbf{V}^{(1x)}$. As the spin-orbit interaction has the form $\mathbf{L}\cdot\mathbf{S}$, this depends on both the total orbital angular momentum and total spin angular momentum and is given by [70]:

$$\begin{aligned} \langle l^n \nu LS|\mathbf{V}^{(1x)}|l^n \nu' L'S'\rangle \quad &= N\sqrt{s(s+1)(2s+1)(2S+1)(2L+1)(2S'+1)(2L'+1)} \\ &\sum_{\nu_1,L_1,S_1} (G^{n,\nu,L,S}_{n-1,\nu_1 L_1,S'_1})^* (G^{n,\nu',L',S'}_{n-1,\nu_1 L_1,S'_1})(-1)^{S_1+L_1+S+L+s+l+x+1} \\ &\begin{Bmatrix} S & S' & 1 \\ s & s & S_1 \end{Bmatrix} \begin{Bmatrix} L & L' & x \\ l & l & L_1 \end{Bmatrix} \end{aligned} \tag{2.6}$$

where an additional factor of $(-1)^x$ is included for the situation of a greater than half filled shell (i.e. the spin orbit interaction reverses sign in the hole picture).

Although these formulae appear complex, their power lies in that they only need to be computed once for interactions between a pair of atomic terms $|\nu SL\rangle$ and $|\nu' S' L'\rangle$, and can be used in subsequent calculations. Furthermore, by seeing which of these reduced matrix elements are nonzero, we can determine which atomic terms will interact under various perturbations.

2.2.2 Coulomb interaction

The first relevant interaction in determining the properties of metal-organic complexes is the Coulomb interaction, which is due to electrostatic repulsion between pairs of electrons. For this reason, the Coulomb interaction only applies for multi-electron systems (i.e. $n \geq 2$). As a matter of convention, the Coulomb interaction for transition metals are typically parameterized by the Racah parameters A, B, C, while the rare earths are described by the Slater-Condon parameters

F^0, F^2, F^4, F^6. They are directly related using the correspondence (there is no F^6 term for the $l = 2$ transition metals):

$$\begin{aligned} F^4 &= \tfrac{63}{5}C \\ F^2 &= 49(B + \tfrac{5}{441}F_4) \\ F^0 &= A + F_4/9 \end{aligned} \tag{2.7}$$

For two atomic terms $|l^n \nu LS\rangle$ and $|l^n \nu' L' S'\rangle$, the Coulomb interaction mixes terms with the same total angular momentum L and spin angular momentum S under the form:

$$\delta_{L,L'}\delta_{S,S'} \sum_{k=0,2,4} F^k c^k(\nu\nu' LS) \tag{2.8}$$

where:

$$c^k(\nu\nu' LS) = \frac{1}{2}\langle l|\mathbf{C}^{(k)}|l\rangle^2 \left\{ \begin{array}{c} \underbrace{\frac{1}{2L+1}\sum_{\nu'' L''} \langle l^n \nu LS|\mathbf{U}^{(k)}|l^n \nu'' L'' S\rangle \langle l^n \nu' L' S|\mathbf{U}^{(k)}|l^n \nu'' L'' S\rangle}_{\sim \mathbf{C}_i^{(k)} \cdot \mathbf{C}_j^{(k)}} \\ \underbrace{-\frac{n}{2l+1}\delta_{\nu,\nu'}}_{\text{same seniority}} \end{array} \right\} \tag{2.9}$$

2.2.3 Crystal field interaction

The crystal field interaction splits the degeneracy of the eigenstates of some angular momentum multiplet J. For transition metal complexes, where the interaction with the ligands is strong, the crystal field interaction operates directly on the orbital angular momentum momentum basis L. For lanthanide ions, the spin-orbit coupling is much stronger such that the spin-orbit interaction splits the SL states into distinct J manifolds. The crystal field interaction then breaks the degeneracy of these J-multiplets.

The crystal field interaction is given by:

$$V_{\mathrm{CF}} = \sum_{k,q} B_q^k C_q^{(k)} \tag{2.10}$$

where the B_q^ks are the crystal field parameters and $C_q^{(k)}$ is the k-th order spherical tensor operator. These crystal field parameters emerge from any asymmetry in the distribution of charges surrounding the metal ion. Ligand field theory additionally considers the possibility that the energies of different orbitals are shifted due to covalent interactions between the metal center and ligands. An intuitive picture is that overlap between the ligands and the orbitals of a metal center state generally the overall energy of the state. In any case, these crystal field parameters serve as a measure of how much the charge distribution surrounding the metal ion deviates from spherical symmetry.

For the transition metals, we work in the $|LS\rangle$ basis, where the crystal field operator acts naturally on orbital angular momentum L. Using the Wigner-Eckhart theorem, we can expand the expectation values of $\langle \nu SLM_S M_L | H_{\mathbf{CF}} | \nu' S' L' M_S' M_L' \rangle$ as:

$$\begin{aligned}
\langle \nu SLM_S M_L | C_q^{(k)} | \nu' S' L' M_S' M_L' \rangle &= (-1)^{L-M_L} \begin{pmatrix} L & k & L' \\ -M_L & q & M_L' \end{pmatrix} \\
&\quad \delta_{M_S, M_S'} \underbrace{\langle \nu SL | C^{(k)} | \nu' S' L' \rangle}_{\text{reduced matrix element}} \\
&= (-1)^{L-M_L} \begin{pmatrix} L & k & L' \\ -M_L & q & M_L' \end{pmatrix} \\
&\quad \delta_{M_S, M_S'} \underbrace{\left[\delta_{\nu,\nu'} \delta_{S,S'} (-1)^L \sqrt{(2L+1)(2L'+1)} \begin{pmatrix} L & k & L' \\ 0 & 0 & 0 \end{pmatrix} \right]}_{\text{reduced matrix element} \langle \nu SL | C^{(k)} | \nu' S' L' \rangle}
\end{aligned} \tag{2.11}$$

Orbital	Representation	$\langle\phi_i\|H_{\mathrm{CF}}\|\phi_i\rangle$
d_{z^2}	$\|2,0\rangle$	$-6\|Dq\|$
$d_{x^2-y^2}$	$\frac{\sqrt{2}}{2}(\|2,-2\rangle+\|2,2\rangle)$	$-6\|Dq\|$
d_{xy}	$\frac{-\sqrt{2}}{2}(\|2,-2\rangle-\|2,2\rangle)$	$4\|Dq\|$
d_{yz}	$\frac{\sqrt{2}}{2}(\|2,-1\rangle+\|2,1\rangle)$	$4\|Dq\|$
d_{xz}	$\frac{\sqrt{2}}{2}(-\|2,-1\rangle+\|2,1\rangle)$	$4\|Dq\|$

Table 2.3: d-orbital splittings for a tetrahedrally-symmetric ligand field. The d_{z^2} and $d_{x^2-y^2}$ orbitals are shifted downwards in energy by $6|Dq|$ while the d_{xy}, d_{yz}, and d_{xz} orbitals are shifted upwards by $4|Dq|$. A single particle excitation into the excited state therefore requires $10|Dq|$ of energy.

where the reduced matrix element $\langle \nu SL|C^{(k)}|\nu' S' L'\rangle$ can be computed (as in Equation 2.5):

$$\delta_{\nu,\nu'}\delta_{S,S'}(-1)^L\sqrt{(2L+1)(2L'+1)}\begin{pmatrix} L & k & L' \\ 0 & 0 & 0 \end{pmatrix}. \tag{2.12}$$

From the form of this interaction, we note that the crystal field only couples atomic terms with the same spin multiplicity S ($\delta_{S,S'}$) and within the same spin sublevel M_S ($\delta_{M_S,M_S'}$), which has the important consequence that any spin-dependent behavior can only be mediated through the spin-orbit coupling.

As a quick example, we can calculate the crystal field splitting on the d-orbitals induced by a tetrahedral ligand field. For an electron with $l=2$, a T_d-symmetric ligand field has $B_4^0=-21|Dq|$ with $B_4^4=\sqrt{\frac{5}{14}}B_4^0$. We note the reduced matrix element is the same for each of the d-orbitals and equal to:

$$\langle 1D|C^{(4)}|1D\rangle=(-1)^2\sqrt{((2(2)+1)(2(2)+1)}\begin{pmatrix} 2 & 4 & 2 \\ 0 & 0 & 0 \end{pmatrix}=\frac{\sqrt{70}}{7} \tag{2.13}$$

To determine the splitting of each of the orbitals, we can then compute the expectation value of $\langle\phi_i|V_{\mathrm{CF}}|\phi_i\rangle$ using the definition of the d-orbitals and evaluating Equation 2.11 to obtain the results in Table 2.3.

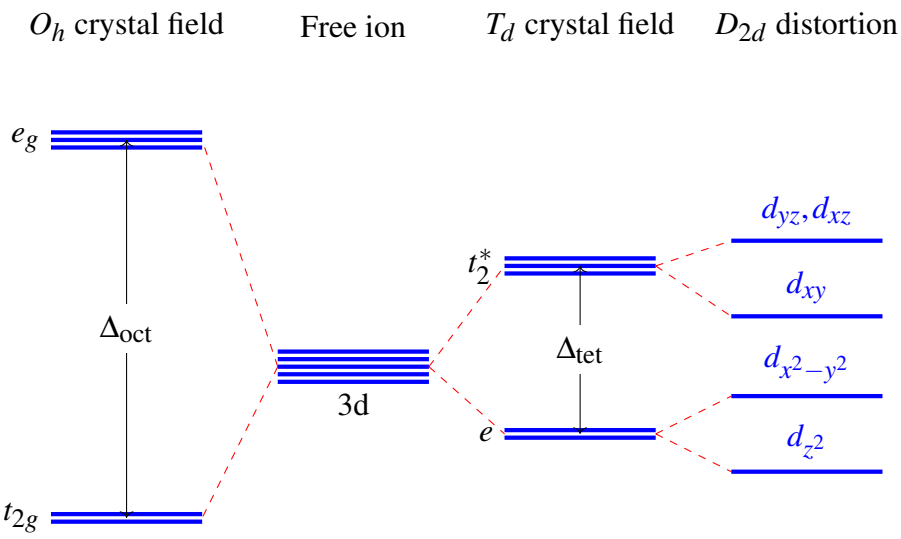

Figure 2.2. Splitting of d-orbitals under various ligand fields. For an octahedral field, the t_{2g} orbitals shift downwards while the e_g orbitals increase in energy for a total splitting Δ_{oct}. For a tetrahedral field, the situation is reversed and the two e non-bonding orbitals are lowered in energy, while the t_2^* orbitals are increased in energy. In addition, due to the breaking of inversion symmetry, the orbitals lose their gerade subscript. The energy splitting is reduced for a tetrahedral field relative to an octahedral field: $\Delta_{\text{tet}} = \frac{4}{9}\Delta_{\text{oct}}$. Lowering the symmetry further breaks the degeneracy of these orbital levels.

Thus, the impact of a tetrahedral ligand field is to lower the energy of the d_{z^2} and $d_{x^2-y^2}$ orbitals, while increasing the energy of the d_{xy}, d_{xz}, and d_{yz} orbitals, as shown in Figure 2.2. For context, the same considerations apply to octahedral complexes, though the sign of the interaction is reversed and the splitting is higher in the octahedral case.

For the rare earth ions, the strong spin orbit coupling forces us to work in the $|JM_J\rangle$ basis, where the crystal field interaction takes on the form given by Equation 15-33 of [69]:

$$\begin{aligned}\langle \nu SLJM_J|C_q^{(k)}|\nu' S'L'J'M_J'\rangle =& (-1)^{J-M_J}\begin{pmatrix} J & k & J' \\ -M_J & q & M_J' \end{pmatrix}(-1)^{S+L'+J+k} \\ & \sqrt{(2J+1)(2J'+1)}\begin{Bmatrix} J & k & J' \\ L' & S & L \end{Bmatrix}\langle \nu SL|C^{(k)}|\nu' S'L'\rangle \end{aligned} \tag{2.14}$$

In general, there is a deeper relation between the non-zero crystal field parameters and the symmetry of the charge distribution produced by the surrounding ligands [71].

2.2.4 Spin-orbit coupling

Although typically disregarded for the transition metals, for our purposes, spin-orbit coupling is an absolutely vital effect. It is necessary to fully explain both the spin properties of our metal-organic complexes, and account for some of the spin-dependent optical processes required for a spin-photon interface. The spin-orbit interaction is given by:

$$V_{\mathrm{SO}} = \lambda \hat{L} \cdot \hat{S} = \tfrac{1}{2}\lambda_{\perp}(L_{+}S_{-} + L_{-}S_{+}) + \lambda_{\parallel} L_z S_z \tag{2.15}$$

where $L_{\pm}$ and L_z are the orbital angular momentum operators, $S_{\pm}$ and S_z are the spin angular momentum operators, and $\lambda_{\perp}$ and $\lambda_{\parallel}$ denote the transverse and longitudinal components of this interaction respectively.

For the first and second row transition metals, we can express this interaction in the spherical tensor formalism in the $|\nu SLM_S M_L\rangle$ basis as:

$$\begin{aligned}\langle \nu SLM_S M_L | H_{\mathrm{SO}} | \nu' S' L' M_S' M_L' \rangle = \quad & \sqrt{l(l+1)(2l+1)}\langle \nu SL | \mathbf{V}^{11} | \nu' S' L' \rangle \\ \sum_{q=-1}^{+1} \kappa_q^1 \quad & (-1)^{L-M_L} \begin{pmatrix} L & 1 & L' \\ -M_L & q & M_L' \end{pmatrix} \\ & (-1)^{S-M_S} \begin{pmatrix} S & 1 & S' \\ -M_S & -q & M_S' \end{pmatrix}\end{aligned} \tag{2.16}$$

where $\langle \nu SL | \mathbf{V}^{11} | \nu' S' L' \rangle$ is the reduced matrix element for the orbit-spin operator and $\kappa^1 \rightarrow \kappa_{xy}^1 = \kappa_{\pm 1}^1, \kappa_z^1 = \kappa_0^1$ are the orbital reduction factors. Note that the form of this operator enforces the same selection rules as the spin-orbit operator above (as $q = 0 \rightarrow M_L = M_L', M_S = M_S'$ and $q = \pm 1 \rightarrow M_L = M_L' \pm 1, M_S = M_S' \mp 1$). As the ligand field interaction only acts directly on

orbital angular momentum, a combination of both lowered symmetry and spin-orbit coupling is necessary to explain the zero-field splitting between spin sublevels observed in the tetrahedral Cr^{4+} complexes studied in this thesis.

For the lanthanides, the spin-orbit coupling takes on an even more crucial role, as it is sufficiently strong that M_L and M_S are no longer good quantum numbers. The total angular momentum $\mathbf{J} = \mathbf{L} + \mathbf{S}$ commutes with the spin-orbit interaction and thus we treat lanthanides in the $|JM_J\rangle$ basis instead. In this basis, the spin-orbit interaction takes on the form given by [65], Equation (19):

$$\langle \nu SLJ|H_{\mathrm{SO}}|\nu' S' L' J'\rangle = \zeta(-1)^{J+L+S'}\sqrt{l(l+1)(2l+1)} \begin{Bmatrix} S & S' & 1 \\ L' & L & J \end{Bmatrix} \langle l^n \nu SL|\mathbf{V}^{(11)}|l^n \nu' S' L'\rangle \tag{2.17}$$

2.2.5 Zeeman effect

Finally, we consider the Zeeman interaction, which acts as a small perturbation in both the transition metal and rare earth ion cases. This effect is particularly important for half integral values of J, as Kramer's theorem requires that $|JM_J\rangle$and $|JM_{-J}\rangle$ are energetically degenerate for $B = 0$.

$$V_{\mathrm{Zeeman}} = V_{\mathrm{Zeeman,L}} + V_{\mathrm{Zeeman,\ S}} = \mu_B \mathbf{B} \cdot (\kappa \mathbf{L}^{(1)} + g\mathbf{S}^{(1)}) \tag{2.18}$$

where $\mathbf{B}$ is the magnetic field vector, μ_B is the Bohr magneton, g is the electron g-factor. We convert the Cartesian magnetic field into spherical tensor components as: $\mathbf{B} \rightarrow B^1_0 = B_z, B^1_{\pm 1} = \frac{\mp}{\sqrt{2}}(B_x \pm iB_y)$.

In the $|vSLM_SM_L\rangle$basis, we can separate the orbital and spin parts and calculate the Zeeman interaction matrix elements as:

$$\begin{aligned}\langle vSLM_SM_L|H_{\text{Zeeman,L}}|v'S'L'M_S'M_L'\rangle =&\delta_{v,v''}\delta_{L,L'}\delta_{S,S'}\delta_{M_S,M_S'}\mu_B\sqrt{L(L+1)(2L+1)}\\ &(-1)^{L-M_L}\sum_{q=-1}^{+1}(-1)^q B^1_{-q}\kappa^1_q\begin{pmatrix} L & 1 & L' \\ -M_L & q & M_L'\end{pmatrix}\end{aligned} \tag{2.19}$$

where $\kappa^1_{\pm 1}=\kappa_{xy}, \kappa^1_0=\kappa_z$ are the orbital reduction factors, and

$$\begin{aligned}\langle vSLM_SM_L|H_{\text{Zeeman,S}}|v'S'L'M_S'M_L'\rangle =&\delta_{v,v''}\delta_{L,L'}\delta_{S,S'}\delta_{M_L,M_L'}\mu_B g\sqrt{S(S+1)(2S+1)}\\ &(-1)^{S-M_S}\sum_{q=-1}^{+1}(-1)^q B^1_{-q}\begin{pmatrix} S & 1 & S' \\ -M_S & q & M_S'\end{pmatrix}\end{aligned} \tag{2.20}$$

respectively.

For the lanthanides we can express this interaction in the $|vSLJM_J\rangle$ basis as:

$$\langle vSLJM_J|H_{\text{Zeeman}}|v'S'L'J'M_J'\rangle =\langle vSLJ|L+gS|v'S'L'J\rangle\sum_{q=-1}^{+1}B^1_q\begin{pmatrix} J & 1 & J' \\ M_J & q & M_J'\end{pmatrix} \tag{2.21}$$

where the reduced matrix element $\langle vSLJ|L+gS|v'S'L'J'\rangle$ is given by:

$$\begin{aligned}\langle vSLJ|L+gS|v'S'L'J\rangle &= \delta_{v,v''}\delta_{L,L'}\delta_{S,S'}g_J\sqrt{J(J+1)(2J+1)} \qquad (J=J') \\ \langle vSLJ|L+gS|v'S'L'(J-1)\rangle &= (g_J-1)\sqrt{\tfrac{(S+L+J+1)(J+L-S)(J+S-L)(S+L-J+1)}{4J}} \quad (J'=J-1)\end{aligned} \tag{2.22}$$

The $J=J'$ case corresponds to the Zeeman splitting within J multiplets, and the $J'=J-1$ case corresponds to the magnetic dipole moment between different J multiplets (which is responsible for the magnetic dipole allowed $4f-4f$ transitions).

2.3 Transition metal ions

Having outlined the various interaction terms, we specialize to the case of the 3*d* transition metal ions. For these complexes, the ligand field is a strong perturbation and acts to split the free ion states. This splitting is sufficiently strong such that the relative ordering of the different energy levels can vary depending on the ligand field strength. Though the comparable strengths of the Coulomb interaction and the ligand field may initially seem complicated, the Tanabe-Sugano diagram framework allows the electronic properties of octahedral or tetrahedral complexes in different ligand field strength regimes to be quickly determined. This analysis also provides a convenient starting point when considering the impact of a reduced-symmetry ligand field.

2.3.1 Tanabe-Sugano diagrams

These diagrams were first tabulated by Tanabe and Sugano in 1954 [72]. The left side of the diagram is equivalent to the free ion case ("weak field limit"), where only the Coulomb interaction contributes to the spacing of energy levels. The right side of the diagram is the "strong field limit" where the energy scale is dominated by interaction with the ligands. Energies are plotted relative to the ground state. These Tanabe-Sugano diagrams are computed directly from the code in the Appendix C. Note that, in contrast to some diagrams presented in the literature where the active space is truncated, our diagrams plot energy level structure for the full set of atomic terms and appear to be in good agreement with other numerical results [73,74].

2.3.2 Cr4+ - ground state

As a substantial portion of this work focuses on tetrahedral Cr^{4+} complexes, we will outline their electronic structure in more detail here. Cr^{4+} has $n = 2$, so we have the following $|\nu SL\rangle$ multiplets: $|1G\rangle, |3F\rangle, |1D\rangle, |3P\rangle, |1S\rangle$. Our ground state (in the free ion case) will be the one that maximizes the total spin (and then orbital multiplicity), and is therefore $|3F\rangle$.

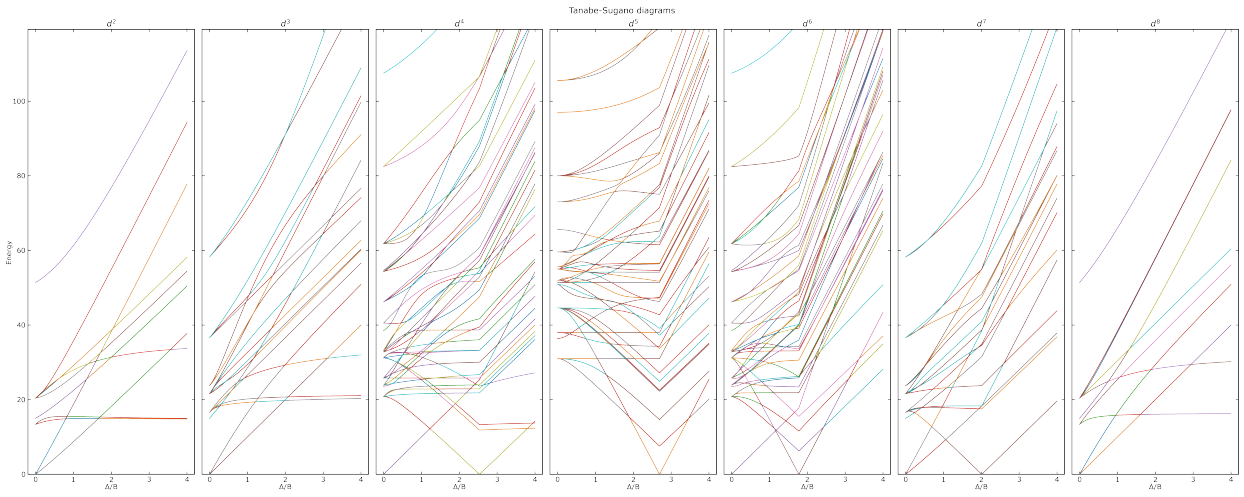

Figure 2.3. Tanabe-Sugano diagrams for transition metal complexes, depicting the energy level structure for octahedral complexes. The left side of the diagram corresponds to the free ion limit, where the energies are determined solely by the Coulomb interaction between the free ion states ($A = 0$). Moving along the x-axis corresponds to increasing the ligand field strength Δ. Rather than plotting absolute energies, the diagram plots the energy separation between each of the levels and the ground state (i.e. the ground state is always fixed at $y = 0$).

As chromium is a transition metal, we first take the ligand field perturbation and then consider other perturbations such as symmetry lowering relative to T_d and the spin-orbit interaction. For a tetrahedral complex (as in Figure 2.2), the ligand field lowers the energy of the non-bonding e orbitals ($d_{x^2-y^2}$ and d_{z^2}) while raising the energy of the t_2^* orbitals (d_{xy}, d_{xz}, d_{yz}). For any non-zero ligand field strength, the ground state populates the two e orbitals and thus the ground state is always $3F$.

Following the discussion of [75], in the molecular orbital picture, the e d-orbitals are non-bonding and are thus do not have significant mixing with the ligand σ orbitals. In contrast, the t_2 d-orbitals form both bonding and antibonding orbitals, which are free to hybridize with the ligand orbitals. As we will see in the next chapter, this hybridization is responsible for the strong electric dipole absorption for tetrahedral complexes and a key piece of enabling optical addressability for molecular spins.

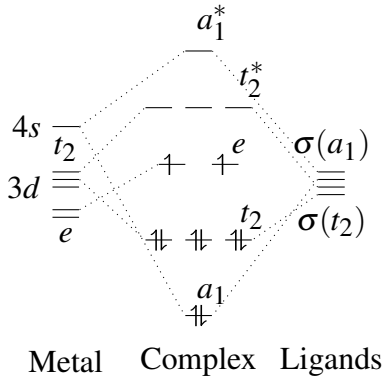

Figure 2.4. Molecular orbital diagram for a tetrahedral d^2 complex. The spin triplet ground state consists of occupation of two lowest energy orbitals ($d_{x^2-y^2}$ and d_{z^2}). These orbitals are non-bonding e orbitals and thus do not significantly hybridize with the ligands. The t_2^* ligands hybridize with the ligands, which introduces a small amount of p-character, increasing the strength of electric dipole transitions to the first triplet excited state, where one of the electrons is promoted to the t_2^* orbitals.

2.3.3 Cr4+ - Optical energy levels

Due to the equivalence between n electrons and $2l-n$ holes, the optical energy levels of tetrahedrally-coordinated Cr^{4+} complexes are given by the d^8 Tanabe-Sugano diagram. For some ligand field strengths, the first excited state is the orbital doublet spin-singlet state, emerging primarily from the $|1D\rangle$ terms with some admixture of $|1G\rangle$ parentage. In the ligand field theory picture, this state emerges from spin pairing of electrons occupying the two e orbitals. For this work, we focused primarily on complexes with ligand field strengths such that the singlet state is intermediate in energy between the two triplet states, as this serves to be a good analog of Cr^{4+}:SiC, an optically addressable spin.

We also have two triplet excited states of interest, which can be easily seen in the electron configuration picture. The first triplet excited state emerges from promotion of a single electron from $e \rightarrow t_2^*$. There are ~ 6 different orbital configurations that are valid, whereby one of the two e orbitals remains occupied and one of the three t_2^* orbitals is occupied. The third excited state comes from the situation where both electrons are promoted out of e into the t_2^* orbitals. There are

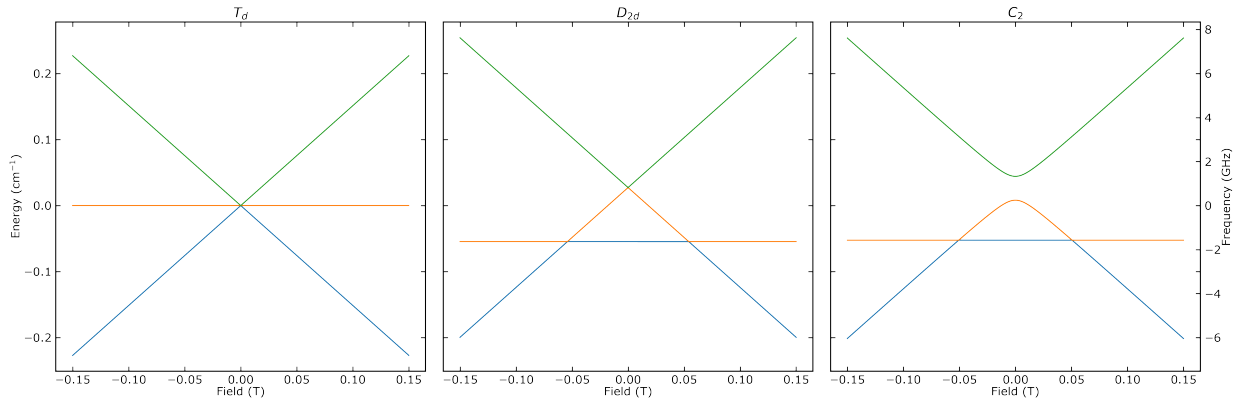

Figure 2.5. Zero field splitting for the $S = 1$ ground state of d^2 ligand fields of various symmetries. The leftmost figure depicts ideal T_d-symmetry, where the spin sublevels remain degenerate at $B = 0$. Deviations from perfect T_d symmetry introduce the zero-field splittings $|D|$ (center and right) and $|E|$ (right panel only). Since the crystal field interaction acts only on the orbital degree of freedom, this splitting in the spin sublevel energies is mediated through the spin-orbit interaction. The $^3A_2$ spin-triplet ground state is an orbital singlet, and thus the zero-field splitting is mediated through spin-orbit mixing with higher excited states.

three valid configurations for this second excited state, where each one leaves one of the t_2^* orbitals unoccupied.

2.3.4 Cr4+ - Spin levels

Finally, we discuss briefly the ground state spin sublevels of the Cr^{4+} complexes studied in this work. As mentioned before, the spin sublevels are a spin-triplet, and thus split according to the Zeeman interaction under a magnetic field. Less straightforward is the existence of the zero-field splitting, by which the sublevels have unequal energies at zero magnetic field. In particular, the ligand field is a spin-conserving interaction due to the $\delta_{M_S,M_S'}$ terms. Therefore, the crystal field interaction cannot break the degeneracy of the spin sublevels on its own. The form of the spin-orbit coupling has both spin conserving ($\lambda_z L_z S_z$) and non-conserving $\frac{1}{2}\lambda_{xy}(L_+S_- + L_-S_+)$ terms. We will see that the zero field splitting emerges from non spin-conserving terms in the spin-orbit coupling, which causes the ground state to get some degree of admixture with various orbital excited states.

2.4 Rare earth ions

In this section, we briefly discuss the electronic structure of rare earth ion metal complexes. In contrast to the transition metal case, the strong spin-orbit coupling in the lanthanide series forces us to consider the spin-orbit interaction first, then consider the crystal field interaction as a small perturbation. This has the important consequence that the electronic energy level structures for rare earth ions are fairly consistent across host materials, as they do not depend strongly on the ligand field strength. This allowed Dieke and colleagues to construct the famous Dieke diagram, which depicts the different energy levels for various rare earth ions [76] as depicted in Fig 2.6.

2.4.1 Electronic structure of Ce^{3+}

In this section, we briefly describe the electronic structure of Ce^{3+} in crystalline materials and molecular complexes. The outer shell of trivalent cerium has a single f-electron, so we just need to consider a single particle with $l = 3 \rightarrow L = 3$ and $s = 1/2 \rightarrow S = 1/2$. Due to the strong spin-orbit coupling of lanthanides, we take the spin-orbit interaction first and obtain the allowed values of $J : |L-S| \leq J \leq |L+S| \rightarrow J = 5/2, 7/2$. Hund's third rule requires that the lowest value of J has the lowest energy (for a subshell that is less than half filled), so the ground state is the $J = 5/2$ and the first excited state is $J = 7/2$. Therefore, we only expect a single magnetic dipole transition between these $J = 5/2$ and $J = 7/2$ manifolds. These manifolds split into a set of Kramers' doublets, according to the symmetry of the ligand field. We will discuss these considerations in more detail in Chapter 6.

A more complete analysis requires consideration of the $5d$ manifold. Since the $4f$ and $5d$ electrons have opposite parity ($\sim (-1)^l$), there is a directly allowed electric dipole transition between the $4f^1 \rightarrow 5d^1$ configurations. As this transition is very strongly allowed, it exhibits short optical lifetimes which has permitted the measurement of single Cerium ions in crystalline materials such as Yttrium Aluminum Garnet (YAG) [44] and Yttrium Orthosilicate (YSO) [77].

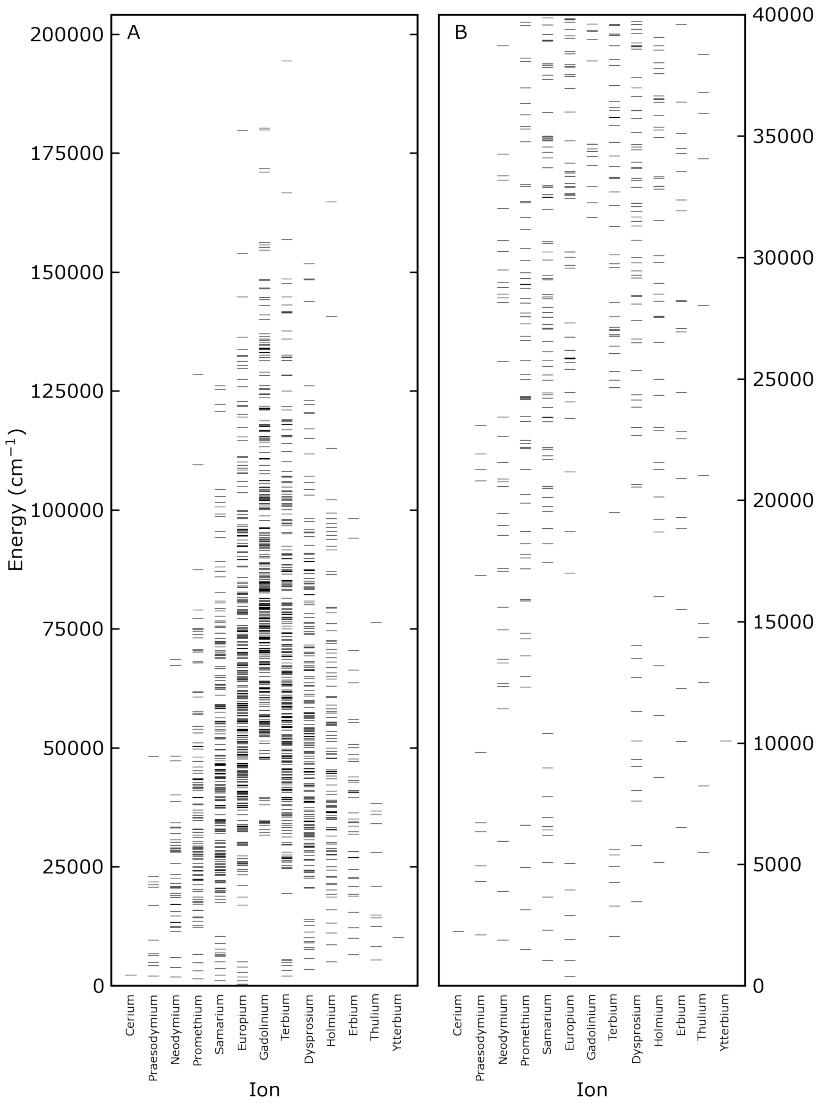

Figure 2.6. Dieke diagram of Lanthanide ions in solids. The full diagram (A) depicts the complete energy level structure for the n-electron ion, where Coulomb repulsion separates the different $|\nu SL\rangle$ multiplets. Spin-orbit coupling further splits these into $|\nu SLJ\rangle$ multiplets. The left half of the diagram (Cerium - Gadolinium) is a system of $4f^n$ electrons, while the right half (Terbium - Ytterbium) can be thought of as $4f^{14-n}$ holes (with the sign of the spin-orbit interaction reversed). The spin-orbit coupling strength increases across the series ($\sim Z^4$), resulting in a larger spacing between the J multiplets arising from each atomic term. The truncated diagram (B) is truncated to 40000cm^{-1}, as this is the range most readily accessible in most experiments.

CHAPTER 3

DEVELOPING SPIN-PHOTON INTERFACES FOR METAL ION COMPLEXES

Having outlined the electronic structure of transition metal and rare earth ion complexes, we discuss the photophysical constraints on implementation of a spin-photon interface. First, we discuss the time evolution of a spin in the presence of a microwave drive and spin-relaxation. Next, we discuss broadly molecular photophysics and the selection rules for various photophysical processes. Finally, we discuss possible spin-dependent photophysical processes and how these can lead to optical spin polarization and spin-dependent optical readout. We conclude by outlining approaches to model these processes using a set of coupled rate equations.

3.1 Spin Coherence and Electron Spin Resonance (ESR)

The development of a viable spin-photon interface relies on the ability to detect light with at least one property (intensity, polarization, etc.) correlated with the spin state of the metal center. However, this readout process competes with spin relaxation, whereby the interactions between the spin and its environment destroy coherence. This detection process constitutes a measurement and therefore serves to project the spin into an eigenstate. We begin with a brief discussion of spin-coherence and relaxation processes and construct a toy model for these processes.

Previously, we discussed the electronic energy level structure of metal-organic complexes of the first and second row transition metals and lanthanides. We outlined how the various atomic term spin multiplicities S (or total angular momentum J for the lanthanides) can be determined, and how consideration of the free ion levels (in tandem with the ligand field) allows easy determination of the expected ground state spin (or total angular momentum) multiplicity. As an example, we discussed the case of Cr^{4+}, where distortions from T_d symmetry, in tandem with spin-orbit coupling, introduces the zero-field splitting H_{ZFS} for the spin-triplet ground state. Furthermore, the interaction with a magnetic field introduces a Zeeman splitting of the spin sublevels given by

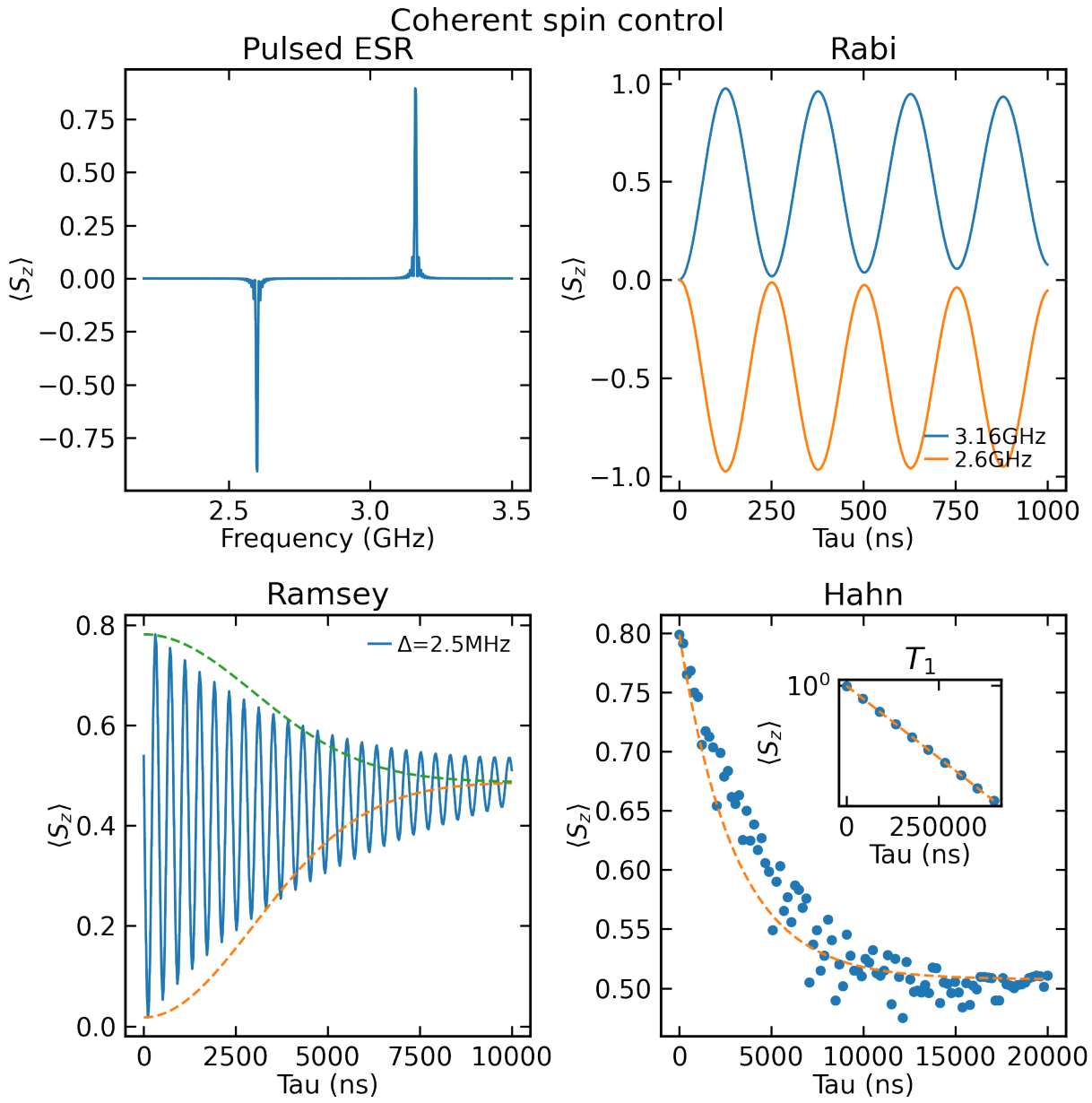

Figure 3.1. Simulations of electron spin resonance. Each plot depicts the expectation value of $\langle S_z \rangle$ under various drive conditions and $T_2 \sim 3\mu$s and $T_1 \sim 100\mu$s.

$H_{\text{Zeeman}} \sim g\mu_B \mathbf{B} \cdot \mathbf{S}$, where g is the electron g-factor, μ_B is the Bohr magneton, $\mathbf{B} = \{B_x, B_y, B_z\}$ is the magnetic field, and $\mathbf{S} = \{S_x, S_y, S_z\}$ are the spin operators.

Next, we introduce a time-dependent microwave drive field $H_{\text{drive}}(t)$ by applying a microwave tone of frequency f. Therefore the total time-independent spin Hamiltonian for the $S = 1$ ground state is given by:

$$H_{\text{spin}}(t) = H_0 + H_1(t) = (H_{\text{ZFS}} + H_{\text{Zeeman}}) + H_{\text{drive}}(t) \tag{3.1}$$

We can model our microwave drive as $H_{\text{drive}}(t) = \Omega_R \sqrt{S(S+1)} \hat{S}_x \sin(\omega t)$, where Ω_R is the Rabi frequency, $\omega = 2\pi \times f$ is the microwave frequency and $\hat{S}_x$ is the spin operator. In the typical ESR experiment, we can measure the expectation value of the spin state along the molecular quantization axis by taking the expectation value $\langle S_z \rangle$.

The standard presentation of quantum mechanics focuses on the evolution of a state ket under the Schrödinger equation, but here we use the density matrix formulation to permit treatment of non-pure states, as well as environmental dephasing and relaxation. The diagonal elements of a density matrix ρ are populations of the states (summing to 1), with the off-diagonal elements representing the coherences between different states. The time-evolution of the system is given by the Lindblad master equation:

$$\dot{\rho} = \underbrace{\frac{-i}{\hbar}\left[H_{\text{spin}}(t), \rho\right]}_{\text{coherent evolution}} + \underbrace{\frac{1}{2}\sum_n \left[C_n \rho(t) C_n^\dagger - \rho(t) C_n^\dagger C_n - C_n^\dagger C_n \rho(t)\right]}_{\text{dephasing and relaxation}} \tag{3.2}$$

where the left half of the equation describes coherent evolution (this is known as the von-Neumann equation) and the right half includes dephasing and relaxation. The $C_n = \sqrt{\gamma_n} A_n$ are known as "collapse operators" and can be determined phenomenologically, but must be traceless in order to conserve populations (i.e. $\text{Tr}(\rho(t)) = 1$).

Having set up these equations, we can now perform some basic simulations of both conventional electron spin resonance (ESR) in Figure 3.1 and optically detected magnetic resonance

(ODMR) in Figure 3.5. The simulations in this chapter were performed using the Quantum Toolbox in Python (QuTiP) [78,79]. For simplicity, these models assume the initial condition $\rho(t=0) = |0\rangle\langle 0|$, and that the collapse operator for spin-lattice relaxation drives $|\pm 1\rangle \rightarrow |0\rangle$ (i.e. the $T = 0$ limit, where all population ultimately relaxes to the ground state). Conventional ESR typically probes the subpopulation of spins which are thermally polarized, which limits sensitivity.

3.1.1 Spin-lattice relaxation

Spin-lattice relaxation drives the population of the different spin sublevels to thermal equilibrium (i.e. Boltzmann polarization). For the transition metal compounds considered in this thesis, this process is driven primarily by molecular vibrations in conjunction with spin-orbit coupling, which maps fluctuations acting on the orbital angular momentum to the spin. There are several physical mechanisms that are responsible for this relaxation, such as the direct, Orbach, and Raman processes, which have their own characteristic dependence on temperature and magnetic field [80]. For the purposes of this discussion, we are less concerned with the distinct physical mechanisms of these processes, and merely interested in long-lived spins where the relaxation to the lattice is slow relative to the optical lifetime.

Although molecular systems are typically considered "floppy" relative to crystals, molecular design does offer several unique strategies that can help mitigate spin-lattice relaxation. For example, minimization of ground-state angular momentum [81], tailoring of lattice vibrational modes [82,83], and increasing covalency between the metal and ligand orbitals [84] have each been shown to increase the spin-lattice relaxation timescales for molecular spin systems. These strategies are generally not available to solid-state spin qubits, and thus represent interesting knobs that can potentially improve molecular spin properties.

The rate of spin-lattice relaxation can be determined experimentally in both conventional ESR and optically-detected magnetic resonance by preferentially populating some excited state sublevel, and then measuring the equilibration of the sublevel populations over time. The decay in

polarization proceeds exponentially, with a characteristic timescale T_1, known as the spin-lattice relaxation time.

3.1.2 Spin dephasing

Dephasing, by which superposition between states decays, presents an additional challenge for molecular spin qubits. Dephasing is manifested as a decay in the off-diagonal coherences in the density matrix over time. This process is typically driven by magnetic field noise, where the transition frequency of a spin qubit is broadened or modulated by interaction with a fluctuating magnetic field. For spin qubits, this dephasing is typically driven by homonuclear interactions between the pairs of the same nuclear spin species [85] of the atoms comprising the host lattice. These interactions are especially problematic for molecular systems, as many common molecular frameworks rely on hydrogen, which contributes a high density of nuclear spins in the form of ^1H protons. On the bright side, chemical synthesis provides several strategies to help mitigate this issue, such as deuteration of molecular systems [86], use of nuclear spin-free solvents [87,88], or the engineering of clock transitions in the spin Hamiltonian (whereby $\frac{df(B)}{dB} \rightarrow 0$) through chemical design [89]. In addition, techniques from solid state qubits, such as dynamical decoupling and operation at optimal working points [90], can be readily applied to mitigate dephasing errors.

We can characterize dephasing errors with several different experimental lifetimes: T_2^* (inhomogenous dephasing time), T_2/T_m (Hahn-echo coherence time), and T_{DD} (coherence time under dynamical decoupling). Typically $T_2^* \leq T_2/T_m \leq T_{DD}$.

3.1.3 Transition linewidths

Finally, it is important to discuss the radiation absorption linewidth for each of these transitions. In principle, the transition linewidth is lower-bounded by the inverse of the homogeneous dephasing time, whereby a longer dephasing time corresponds to a narrower absorption linewidth. Though an appropriate picture for a single spin, the experiments in this work (and most electron spin resonance experiments) are conducted on ensembles, where local variations in magnetic field or

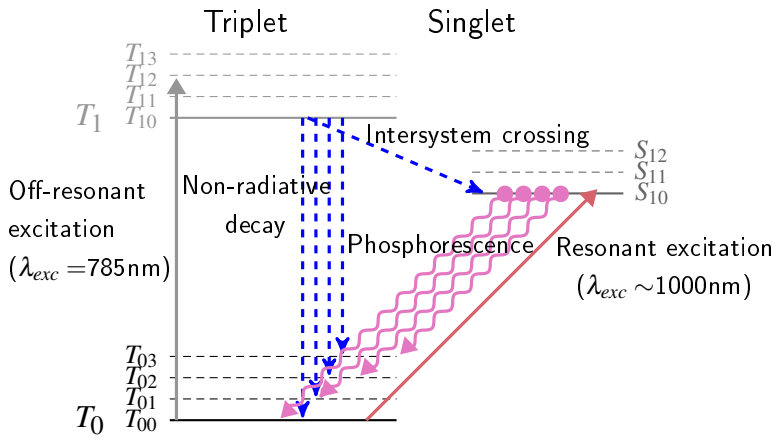

Figure 3.2. Overview of various photophysical processes in molecular systems. The emitter starts in one of the triplet spin sublevels denoted by T_{00}. The emitter can be excited off-resonantly (grey) through a spin-conserving transition to a vibrational triplet state (T_{1n}) or resonantly (peach) to the singlet excited state S_{10} via a spin-flip transition. From the triplet excited state, population rapidly relaxes to the lowest triplet vibrational level T_{10}, where it can undergo intersystem crossing into the singlet excited state or relax to the triplet ground state directly through internal conversion (blue).

strain broaden the transition linewidth. The experimental spin transition linewidth is then the convolution of the intrinsic, homogeneous linewidth and the distribution of transition frequencies across the ensemble. These local variations effectively "smear out" any optical or electron spin resonance contrast, reducing the overall peak intensity relative to a uniform ensemble. These broadening effects, though experimentally important, are not captured in the simple ESR toy model described above. As will be discussed in Section 3.2.3, similar considerations in the optical domain explain the different optical spectra under resonant and off-resonant optical excitation.

3.2 Molecular photophysics

We start with a brief overview of molecular photophysics to outline the landscape of photophysical processes in molecular systems. Using these ingredients, we then specialize to the discuss the photophysical processes occurring in Cr^{4+} and Ce^{3+} complexes.

As with any state transition, molecular photophysics is driven by the selection rules between the initial state $|i\rangle$ and final state $|f\rangle$. The transition rate for some interaction Hamiltonian H_{int} is given by Fermi's Golden rule as:

$$\Gamma_{|i\rangle\rightarrow|f\rangle} = \frac{2\pi}{\hbar}|\langle f|H_{\text{int}}|i\rangle|^2 g(\hbar\omega) \tag{3.3}$$

where $g(\hbar\omega)$ is the density of states at the energy $\hbar\omega$. In free space, we assume a continuum of electromagnetic modes, and thus $g(\hbar\omega)$ is just a constant. It is worth mentioning that this can density of states can be modified significantly by the presence of an electromagnetic cavity, which can strongly enhance or suppress the transition frequency at E_f through the Purcell factor $\sim \frac{Q}{V_{\text{mode}}}$ [91].

A full treatment of Equation 3.3 requires considering the full system wavefunction, taking into account orbital, spin, and vibrational degrees of freedom: $|\psi\rangle = |\psi_{\text{orb}}\rangle|\psi_{\text{spin}}\rangle|\psi_{\text{vib}}\rangle$.

3.2.1 - Electric dipole transitions - optical absorption and emission

Design of a viable spin-photon interface relies on the ability for a complex to efficiently absorb and emit light. One strategy to optimize this ability is to focus on complexes that have a strong electric dipole transition, as electric dipole transitions are typically stronger than magnetic dipole or electric quadrupolar transitions by several orders of magnitude. However, the selection rules for electric dipole transitions introduce an inherent challenge, as the selection rules for electric dipole transitions require a parity change. In particular, the electric dipole transition matrix element is given by $H_{\text{int}} = -e\mathbf{r}$:

$$\langle f|H_{\text{ed}}|i\rangle = -e\langle f|\mathbf{r}|i\rangle \tag{3.4}$$

and thus is vanishing between two states of the same parity.

For this thesis, we focus on two classes of complexes: tetrahedrally-coordinated Cr^{4+} complexes and Ce^{3+} complexes. These complexes are exemplary of two different strategies to in-

troduce a strong electric dipole transition. For the former, we rely on an admixture of $p-$type orbital character due to covalent interactions between the Cr^{4+} metal center and the tetrahedrally-coordinating ligands. For the latter, we use a direct $4f \rightarrow 5d$ transition which involves an explicit parity change. Thus, this transition exhibits strong optical absorption and relatively fast emission characterized by lifetimes in the 10s of nanoseconds in a variety of solid-state host matrices.

3.2.2 Tetrahedral coordination and electric dipole transitions

A central assumption of crystal field theory, in contrast to the ligand field theory, is that the metal ion does not interact directly with the ligands and only feels the effect of adjacent point charges. Though this picture was sufficient in the previous chapter to describe the electronic structures of a broad class of compounds, it fails to when predicting the optical properties of tetrahedral complexes, specifically their optical absorption. Crystal field theory predicts that compounds will have weak electric dipole absorption, which is correct for octahedral complexes. However, for tetrahedral complexes, electric dipole absorption is strong which is not explained by the crystal field theory. For tetrahedral complexes, there is significant overlap between the metal center d-orbitals and the coordinating ligands, allowing these orbitals to hybridize strongly. Ligand field theory then admits some degree of covalency between the metal ion and the coordinating ligands parameterized here by $0 \leq \alpha \leq \sqrt{\frac{1}{2}}$. This leads to the formation of modified bonding, non-bonding, and anti-bonding orbitals as listed in Table 3.1. [75]

These new, modified orbitals have both $s-$ and $p-$character which then permits the following electric dipole transitions between the non-bonding and anti-bonding orbitals as given in Table 3.2 [75].

ψ	Normalization	Orbitals	Characteristic
$\psi_b(t_2)$	N_b	$\sqrt{1-\alpha^2}(3d_{yz})+\alpha\frac{1}{2}(\sigma_1+\sigma_3-\sigma_2-\sigma_4)$	Bonding
		$\sqrt{1-\alpha^2}(3d_{xz})+\alpha\frac{1}{2}(\sigma_1+\sigma_2-\sigma_3-\sigma_4)$	
		$\sqrt{1-\alpha^2}(3d_{xy})+\alpha\frac{1}{2}(\sigma_1+\sigma_4-\sigma_2-\sigma_3)$	
$\psi(e)$	1	$3d_{x^2-y^2}$	Non-bonding
		$3d_{z^2}$	
$\psi_a(t_2^*)$	N_a	$\tilde{yz}=\alpha(3d_{yz})-\sqrt{1-\alpha^2}\frac{1}{2}(\sigma_1+\sigma_3-\sigma_2-\sigma_4)$	Anti-bonding
		$\tilde{xz}=\alpha(3d_{xz})-\sqrt{1-\alpha^2}\frac{1}{2}(\sigma_1+\sigma_2-\sigma_3-\sigma_4)$	
		$\tilde{xy}=\alpha(3d_{xy})-\sqrt{1-\alpha^2}\frac{1}{2}(\sigma_1+\sigma_4-\sigma_2-\sigma_3)$	
$\psi_c(a_1^*)$	1	$\alpha(4s)-\sqrt{1-\alpha^2}\frac{1}{2}(\sigma_1+\sigma_2+\sigma_3+\sigma_4)$	Antibonding

Table 3.1: Molecular orbitals for tetrahedral complexes.

H_{ed}	$\lvert 3d_{x^2-y^2}\rangle$	$\lvert 3d_{z^2}\rangle$
$\langle\tilde{xy}\rvert$	0	$-N\sqrt{1-\alpha^2}\frac{8}{3}A\mathbf{k}$
$\langle\tilde{yz}\rvert$	$-N\sqrt{1-\alpha^2}\frac{4}{\sqrt{3}}A\mathbf{i}$	$N\sqrt{1-\alpha^2}\frac{4}{3}A\mathbf{i}$
$\langle\tilde{xz}\rvert$	$-N\sqrt{1-\alpha^2}\frac{4}{\sqrt{3}}A\mathbf{j}$	$N\sqrt{1-\alpha^2}\frac{4}{3}A\mathbf{j}$

Table 3.2: Electric dipole selection rules in the Cartesian basis.

3.2.3 Homogeneous and inhomogeneous broadening

In practice, although the molecular systems we study are chemically identical, they are not truly indistinguishable in the sense that they see slightly different local environments. Thus, it's worthwhile to briefly describe two different types of broadening: homogeneous and inhomogeneous, as they are caused by different physical mechanisms and manifest differently experimentally. The former is the linewidth of the emitter in the single emitter limit, and is lower bounded by the radiative lifetime. In practice, near-lifetime limited emission has been demonstrated for single emitters for both molecular [59,92] and solid state [93–95] emitters, though there are often significant challenges such as spectral diffusion that prevent reaching this limit. The inhomogeneous linewidth is an ensemble effect, which is driven by variations between molecules or emitters. Although the molecular systems we study are chemically identical, they are not truly indistinguishable in the sense that they see slightly different local environments.

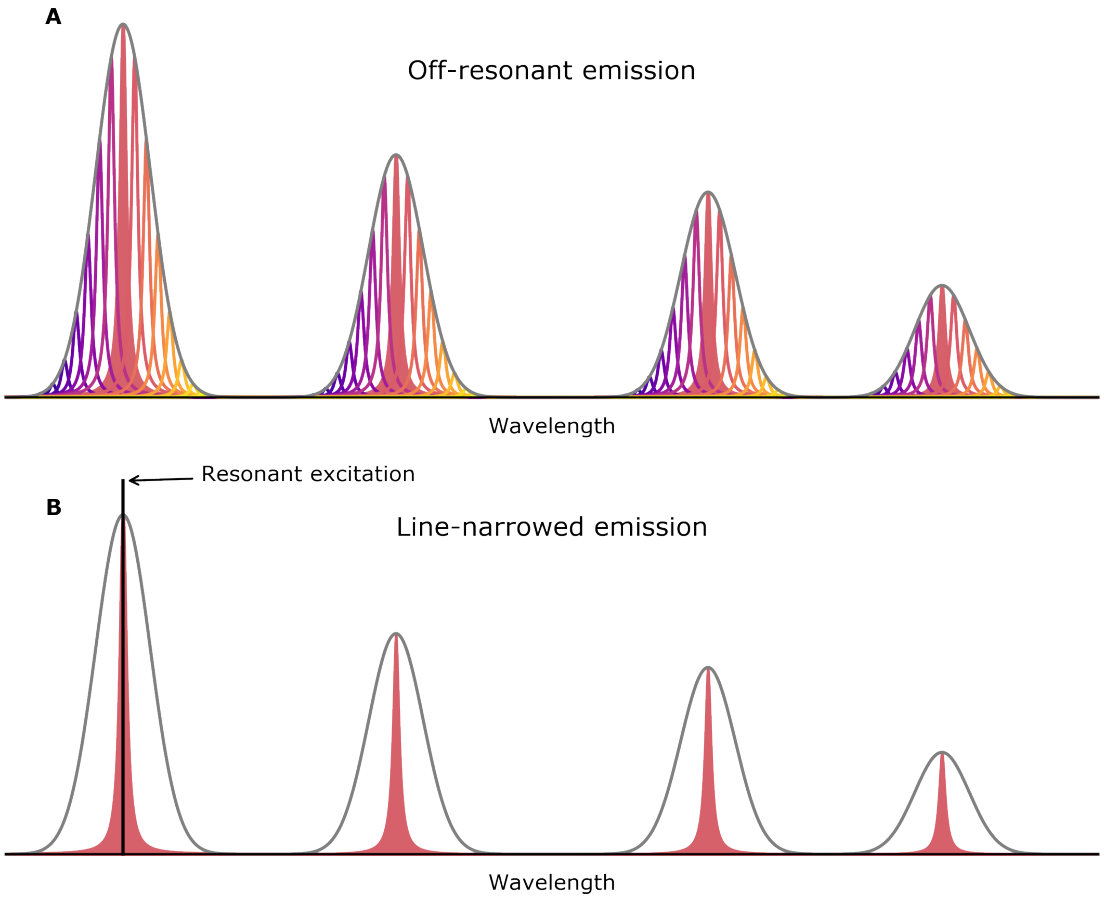

Figure 3.3. Optical emission spectra under off-resonant (top) and resonant (bottom) excitation. Off-resonant excitation yields a broadened emission spectra, as all molecules in the ensemble are excited to a vibrational excited state, which undergoes rapid relaxation to the vibrational ground state. In the resonant case, the laser selectively excites a subensemble of molecules with transitions resonant with the laser, producing a line-narrowed emission spectra.

3.2.4 Non-radiative processes

In addition to optically emissive transitions, molecular systems can undergo non-radiative transitions which may play an important role in their photophysical dynamics. These are typically classified according to their impact on the electronic spin multiplicity: vibrational relaxation (which occurs within a ladder of vibronic states), intersystem crossing (which changes the spin multiplicity) or internal conversion (which conserves the spin multiplicity).

Vibrational relaxation is responsible for driving transitions from vibrational excited states that mediate absorption to the vibrational ground state for a particular manifold. For our purposes, this process is so fast as to be considered instantaneous. However, this does have an important consequence - Kasha's rule, which states that luminescence occurs primarily from the lowest energy level of a particular multiplicity [96].

Intersystem crossing (ISC) is a non-radiative process responsible for transitions between states of different spin multiplicities S. This change in spin multiplicity must be mediated through the spin-orbit coupling, with the rate of ISC will be proportional to the matrix element of the spin-orbit coupling between the initial state $|i\rangle$ and final state $|f\rangle$. By Fermi's golden rule, this transition rate will scale according to:

$$k_{\mathrm{ISC}} \sim |\langle f|H_{\mathrm{SO}}|i\rangle|^2 = \sum_i \tfrac{1}{2}\lambda_{\perp}(\hat{l_{+,i}}\hat{s_{-,i}} + \hat{l_{-,i}}\hat{s_{+,i}}) + \lambda_z \hat{l_{z,i}}\hat{s_{z,i}} \tag{3.5}$$

where $\lambda_{\perp(\|)}$ are the transverse and longitudinal spin orbit coupling constants, and $\hat{l}_i$s and $\hat{s}_i$s are the single electron operators for orbital and spin angular momentum respectively. One important consideration from molecular photophysics is the El-Sayed rule, which stipulates that the spin-orbit interaction (and therefore intersystem crossing rate) is strong between states with a single change in orbital type [97].

In contrast to intersystem crossing, internal conversion drives relaxation between states of the same spin multiplicity. As this process is spin-conserving, it can occur directly due to the interaction between orbitals and vibrational modes of the molecule or the host matrix. The effect of this

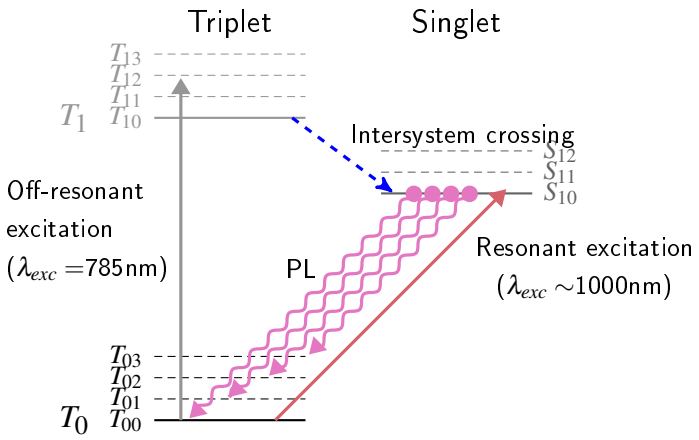

Figure 3.4. Schematic of photophysics of tetrahedral Cr^{4+}. Off-resonant excitation drives an electric dipole transition from the ground state spin triplet into the vibrational ladder of the first spin-triplet excited state. Following relaxation into the vibronic ground state of this excited triplet state, rapid intersystem crossing into the intermediate spin-singlet excited state occurs. The singlet state relaxes back to the vibrational ladder of ground state through phosphorescence. Alternatively, the singlet state can be excited resonantly through an optically narrow, spin-flip transition.

relaxation is to decrease the radiative efficiency out of an excited state, with the excited state decay rate then determined by the sum of internal conversion and optical emission rates.

3.2.5 Photophysics of tetrahedral Cr^{4+}

Now we specialize to discuss the physics of the tetrahedral Cr^{4+} complexes studied in this thesis in Chapters 4 and 5. As discussed in Section 2.3.2, tetrahedral Cr^{4+} has a triplet ground state. The first two excited states are singlet and triplet, with the singlet state lying intermediate between the two triplet states. We can excite two types of electric dipole transitions: a spin-conserving triplet-triplet transition (gray in Figure 3.4), and a spin non-conserving triplet-singlet excitation (peach in Figure 3.4).

The spin conserving transition can excite the molecule into any of the vibrational modes in the excited state.

3.2.6 *Photophysics of Ce^{3+}*

For Ce^{3+}, since the ground state is a $4f^1$ configuration, the first excited state is a $5d^1$ configuration and thus electric dipole transitions are allowed to first order, even with vanishing ligand hybridization. As a result, many trivalent cerium ions exhibit strong optical absorption and emission, with characteristic excited state lifetimes of approximately 10-100ns. In addition, the strong spin-orbit coupling of the lanthanide series permits highly spin-selective pumping under circularly polarized excitation. Provided that these compounds are photostable and the optical cycle is primarily metal-centered, optical detection and spin readout of single cerium ions can be demonstrated [44,77]. Remarkably, provided the lowest $5d^1$ doublet is sufficiently well isolated from the other $5d^1$ doublets, the excited state spin can be read out optically at room temperature. We will discuss the photophysics of these in more detail in Chapter 6.

3.3 Spin-photon interface

Finally, we combine photophysical and spin relaxation considerations together to construct a basic framework to understand the constraints on a viable spin-photon interface. Using a set of coupled rate equations allows us to evaluate the parameters that yield a viable spin-photon interface. We then specialize to discuss the case of Cr^{4+} and Ce^{3+} in more detail.

3.3.1 *Desiderata for a spin-photon interface*

From our discussion so far, we need to have several key criteria to have optically addressable spins:

1. Long T_1 to slow thermalization of spin sublevel populations.

2. Long spin coherence T_2^* and T_2 to enable coherent spin manipulation.

3. Reasonably high radiative efficiency to yield measurable luminescence signal.

4. $T_{\text{opt}} << T_1$, so spin polarization can be built up over multiple cycles.

5. Sufficiently strong spin-dependence to optical cycle to produce optical contrast.

Our previous discussion has already outlined the importance of the first three points. The fourth point highlights the fact that a larger number of optical cycles before relaxation of the spin yields a higher degree of spin polarization. The final piece mentions that the optical cycle must be spin-dependent, but does not provide a specific approach to implement this experimentally. Fortunately, there are several ways that we to accomplish this, namely strongly spin-dependent intersystem crossing rates, optical selection rules, and frequency selective optical pumping. Though the former is responsible for the spin-polarization mechanism of the NV-center in diamond [98], we will focus on the latter two mechanisms in this work. For the transition metal systems studied in this work, the spin-orbit coupling is sufficiently strong that the intersystem crossing rates are effectively instantaneous relative to the rest of the system dynamics [99].

3.3.2 Optically detected magnetic resonance

Finally, for systems with a high contrast spin-photon interface, we can perform optically detected magnetic resonance (ODMR) measurements. In these experiments, the detected optical signal is spin-dependent and correlates with the spin state in some way. As an example, for Cr^{4+} compounds, we have $S = 1$ and want to read out population differences between $|0\rangle$ and $|\pm 1\rangle$. Instead of measuring S_z as we did in conventional electron spin resonance, one way to do this is just to take the expectation value of the zero-field splitting operator $H_{\mathrm{ZFS}} \sim S_z^2 - S(S+1)/3$. We performed numerical simulations to determine the time evolution of $\langle S_z^2 \rangle$ for an $S = 1$ spin in the presence of spin-lattice relaxation and dephasing, which is shown in Figure 3.5.

3.3.3 Coupled rate equation modeling

We can model this situation mathematically using a set of coupled rate equations. We can denote the population of the ground state spin sublevels as $n_{g,i}$ and the excited state sublevels as $n_{e,i}$, and the rate of change of these populations as $\dot{n_{g,i}}$ and $\dot{n_{e,i}}$ respectively. These can be grouped into

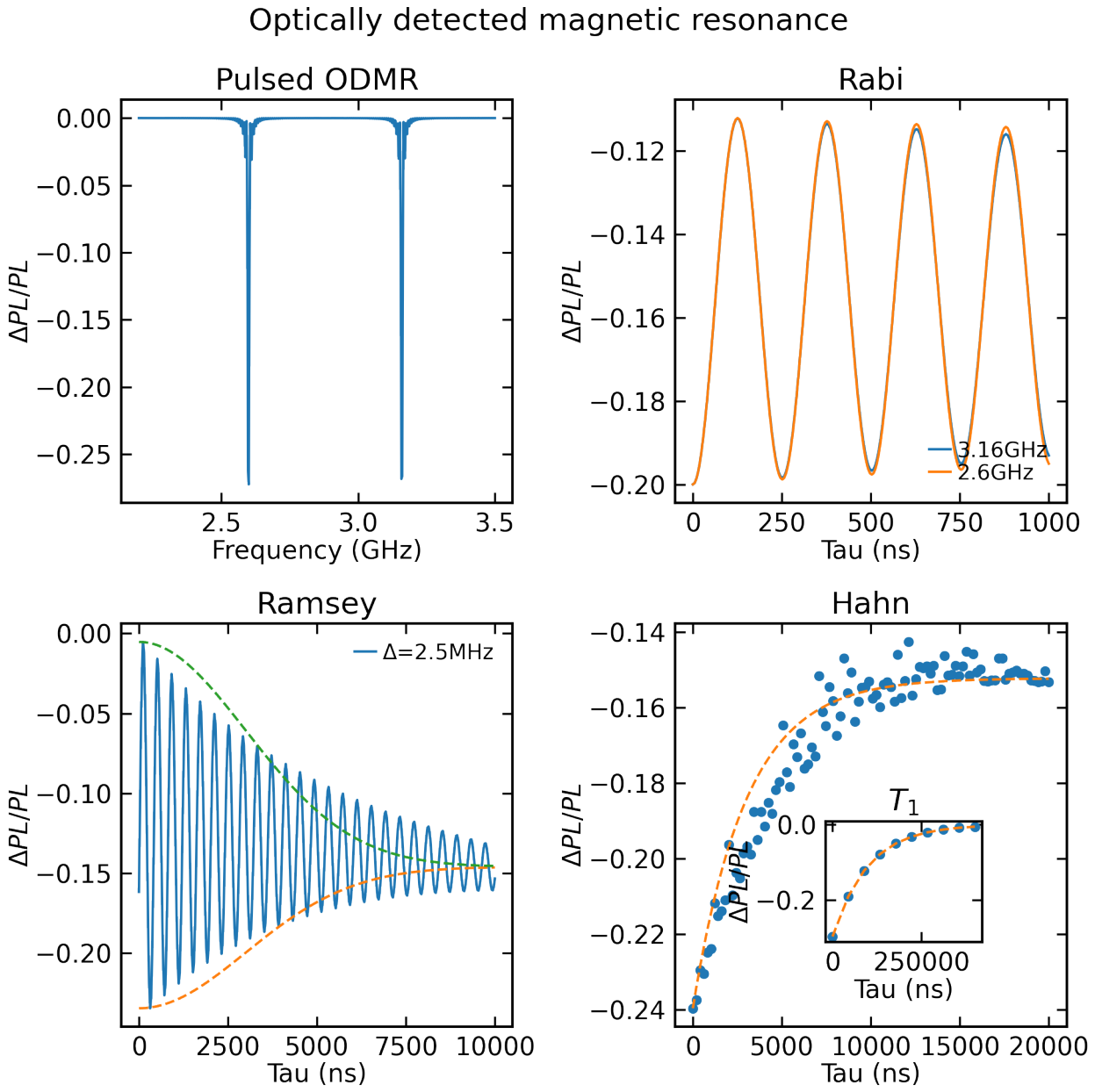

Figure 3.5. Simulations of optically-detected magnetic resonance. Each plot depicts the expectation value of $\langle S_z^2 \rangle$, which corresponds to the population difference between $|0\rangle$ and $|\pm 1\rangle$. In comparison with the Rabi measurement of $\langle S_z \rangle$, the change in luminescence is similar for both $|0\rangle \leftrightarrow |+1\rangle$ and $|0\rangle \leftrightarrow |-1\rangle$. Simulations were performed under and $T_2 \sim 30\mu$s and $T_1 \sim 200\mu$s.

Process	Notation	Comment
Spin-lattice relaxation	γ_{T_1}	Equilibriates spin sublevel populations
Intersystem crossing	γ_{ISC}	Connects multiplets with different S
Optical lifetime	$\gamma_{\text{opt}} = \gamma_{\text{rad}} + \gamma_{\text{non-rad}}$	Includes luminescence and internal conversion
		$\text{PL}(t) \sim \gamma_{\text{rad}} n_e(t)$
Optical Pumping	g_{i}	Drive optical transitions
Microwave drive	g_{MW}	Drive spin transitions

Table 3.3: Transition rates for coupled rate equation modeling.

a single vector $\mathbf{n}$ describing all the level populations n_i. Neglecting the coherences allows us to set up a simplified classical rate equation model to determine the specific conditions under which optical spin contrast is achievable. One important constraint is that all interactions must be linear in the populations, which allows recasting these coupled rate equations into a convenient matrix form $\dot{\mathbf{n}} = \kappa\mathbf{n}$ for some interaction matrix κ. The interaction matrix must therefore conserve population:

$$\sum_i \dot{n_i} = 0 = \sum_j \kappa_{ij} n_j \Rightarrow \kappa_{ij} = -\kappa_{ji} \tag{3.6}$$

.

We can list the various ingredients for our coupled rate equation models in Table 3.3:

These coupled rate equations are linear, first-order, constant-coefficient differential equations and can usually be solved directly given some initial condition $\mathbf{n}(t=0)$ by finding the eigenvalues and eigenvectors for the rate constant matrix κ. However, in many cases, it is sufficient to just solve for the steady state solution by finding the conditions for $\dot{n_i} = 0$ for all states i. By solving for the steady-state solution of these equations subject to the normalization condition $\sum_i n_i = 1$, we can determine the specific conditions under which we get spin-dependent optical contrast.

CHAPTER 4

OPTICAL INITIALIZATION AND READOUT OF MOLECULAR CR^{4+} COMPLEXES

This chapter and figures were adapted from the publication [100].

4.1 Introduction

In this work, we demonstrate the first optical initialization and readout of a molecular spin complex, Cr^{4+}(o-tolyl)$_4$. We use a narrow-line laser to pump population out of spin sublevels whose triplet-singlet transition frequency lies on resonance with the laser frequency, which then relax into the ground state. If the spin relaxes into the initial spin sublevel, it is then repumped, though this does not happen in the case that decay is into a different sublevel, with a different transition frequency. The net result of this is that the sublevels lying off-resonance with the pump laser are preferentially populated.

4.1.1 Experimental schematic

Here, we focus on a set of tetrahedral Cr^{4+} complexes **1**-**3**, which are produced through direct chemical synthesis. These tetrahedral Cr^{4+} complexes have $n = 2$ electrons, yielding a $S = 1$ ground state by Hund's rule. Thus, our ground-state spin Hamiltonian is given by the sum of the zero-field splitting and the Zeeman energy as:

$$H = H_{\mathrm{ZFS}} + H_{Zeeman} = \underbrace{hD\left(S_z^2 - \frac{1}{3}S(S+1)\right) + hE(S_x^2 - S_y^2)}_{\text{zero-field splitting}} + \underbrace{g\mu_B \mathbf{B}\cdot\mathbf{S}}_{\text{Zeeman splitting}} , \qquad (4.1)$$

where h is the Planck constant, D and E are the zero-field splitting parameters, g is the electron g-factor ~ 2 (and assumed isotropic), μ_B is the Bohr magneton, $\mathbf{B}$ is the magnetic field vector, and $\mathbf{S}$ are the spin operators $\{S_x, S_y, S_z\}$. In addition, these complexes have two excited state manifolds

which are experimentally accessible: a higher energy triplet excited state, which can be accessed through spin-conserving, off-resonant excitation, and an intermediate spin singlet state, which is accessed through a spectrally narrow, resonant spin flip transition. These photophysical processes, and the ground and excited state energy levels are depicted schematically in Figure 4.2A.

Figure 4.2B depicts the molecular structure of **1**-**3**, which are homoleptic coordination complexes comprised of a central chromium coordinated with aryl ligands. Each of these compounds can be synthetically produced through choice of the appropriate aryl ligand, i.e. **2** and **3** differ from **1** through the addition of an extra methyl group to the aryl ring. The homoleptic nature of these compounds provides a high degree of symmetry, and the tetrahedral geometry permits strong electric dipole transitions.

An illustration of our experimental setup is shown in Figure 4.2C. Samples were placed on a coplanar waveguide which allowed application of a time varying microwave drive field B_1, and a static magnetic field B_0 can be applied using a permanent magnet. Both resonant and off-resonant lasers were used for photoexcitation (purple beam), and the resulting optical emission (red) was collected and measured. A more detailed diagram and explanation of the experimental setup is shown in Figure 4.1A.

With the exception of the optical Zeeman data shown in Figure 4.2E, all experiments were performed using a home-built confocal microscopy system using a closed cycle cryostat. For the optical Zeeman experiments, excitation and collection were performed through a a fiber optic cable butt coupled to the sample as shown in Figure 4.1B. The experimental apparatus was placed in a closed cycle cryostat housing a superconducting electromagnet, which could provide magnetic fields up to 9T.

4.1.2 Characterization of 1-3

We start by characterizing the optical and spin properties of our tetravalent chromium complexes **1**-**3**. As depicted in the inset of Figure 4.2C, each compound is diluted in a host crystal of their

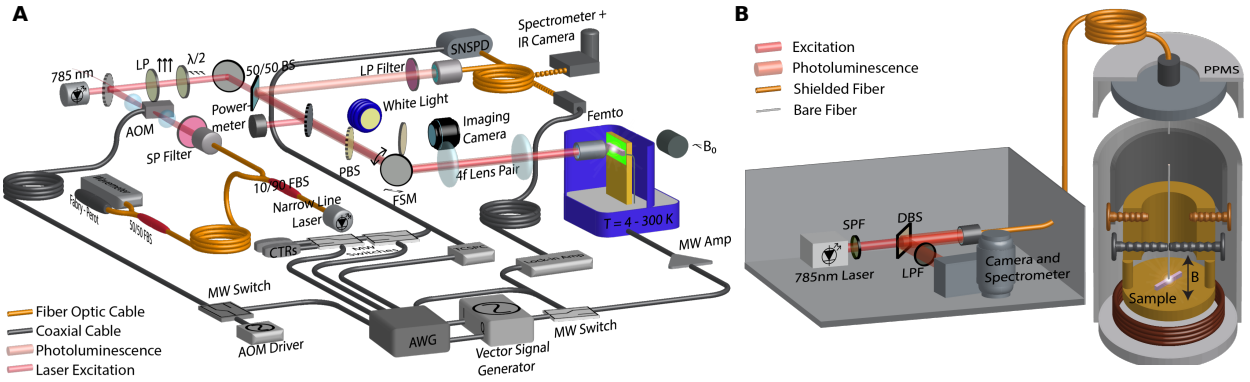

Figure 4.1. Experimental setup used in optical **(A)** and high magnetic field measurements **(B)**. For optical experiments, the sample is placed in a closed cycle cryostat offering temperature control from room temperature down to 4 Kelvin. A variable magnetic field is provided by a magnet mounted on a motorized stage (B_0). Continuous-wave, off-resonant excitation is provided by a 785nm diode laser, which is spectrally-filtered using a short-pass filter. Narrow-line resonant excitation is provided by a diode laser using a motorized Littman-Metcalf cavity geometry. The resonant laser is filtered by a short-pass filter (SP) and passes through an acousto-optic modulator (AOM) to provide timed control of the optical pulses. The modulated laser is coupled into single-mode fiber to provide a high extinction ratio and to yield a high-quality spatial profile. Both lasers pass through a linear polarizer (LP) and half-waveplate ($\lambda/2$) to enable polarization control at the sample. Both beams pass through a 50:50 beamsplitter (BS) and pass through imaging optics (FSM and $4f$) and a high numerical aperture objective to excite the sample. The objective collects optical emission from the sample, which passes through the imaging optics and is reflected by the beamsplitter. A long-pass (LP) spectrally filters the emission (to reject any excitation light), which is then coupled into a fiber for measurement on a suite of detectors. The filtered emission can be measured on a superconducting nanowire single photon detector (SNSPD), femtowatt photoreceiver, or Czerny-Turner spectrometer / camera system to provide single photon detection, low-noise, lock-in detection of intensity, or spectral information respectively. An arbitary waveform generator (AWG) is used to control the timing and modulation of all optical and microwave pulses used in the experiment. Microwave excitation is provided by a vector signal generator (VSG), which outputs a variable frequency and power microwave tone. The VSG also offers internal IQ modulation, and an external microwave switch improves the extinction ratio. The microwave pulses are amplified by an external amplifier (MW amp) to provide sufficient microwave power to drive the spin.

For high field measurements, the sample was placed in a closed-cycle cryostat (Quantum Design PPMS) containing a superconducting magnet providing fields up to 9 Tesla. Light from a 785nm diode laser is spectrally filtered (SPF) and passes through a dichroic beam splitter (DBS) and coupled into a large 400μm core, high numerical aperture fiber. This fiber is then integrated into a home-built feedthrough to both excite and collect optical emission from the sample. Following transit through the fiber, emission is reflected by the DBS, spectrally filtered by a long-pass filter (LPF), and measured spectroscopically by a Czerny-Turner spectrometer / camera system.

isostructural tin analogs. The data in this section provide support for an $S = 1$ ground state, a singlet first excited state, and a higher energy triplet excited state.

4.1.2.1 PL spectra

We present photoluminescence (PL) spectra of **1**-**3** under off-resonant excitation (λ=785nm) in Figure 4.2D. As discussed in Chapter 3, the tetrahedral geometry of these complexes mediates efficient, electric dipole-allowed transitions, and the broadened absorption spectrum is mediated through phonons. Experimental absorption data ([100], Supplementary Materials) show strong absorption indicative of a spin-conserving electric dipole transition. However, the data in Figure 4.2D show spectrally narrow emission, indicative of a spin-flip transition (i.e phosphorescence from an intermediate singlet state).

4.1.2.2 Magneto PL

Magneto-photoluminescence measurements provide additional evidence for the intermediate singlet excited state and triplet ground state electronic structure. Using a superconducting magnetic with a maximum field of 9T, we acquired optical emission spectra as a function of magnetic field. Here, in Figure 4.2E.we focus on the differential spectra taken in the high field and low field limits. Full measurement data is shown in Reference [100], Supplementary Materials. While the spin singlet excited state has $S = 0$ and has no Zeeman term in the Hamiltonian, the spin sublevels of the spin triplet ground state are shifted in energy by the Zeeman splitting.

For high fields where $H_{\text{Zeeman}} >> H_{\text{ZFS}}$, the magnetic field separates the system into the $M_S = \pm 1$ and $M_S = 0$ eigenstates, resulting in a broadening of the optical emission as the various spin sublevels are energetically separated. This process is depicted schematically in the inset of Figure 4.2E. We calculate the differential spectrum (i.e. PL($B = 9$T) - PL($B = 0$T) and observe a central dip corresponding to a decrease in intensity at the ZPL energy as emission for $M_S = \pm 1$ is pushed to lower and higher energies. In these measurements, the ZPL is sufficiently broad that we

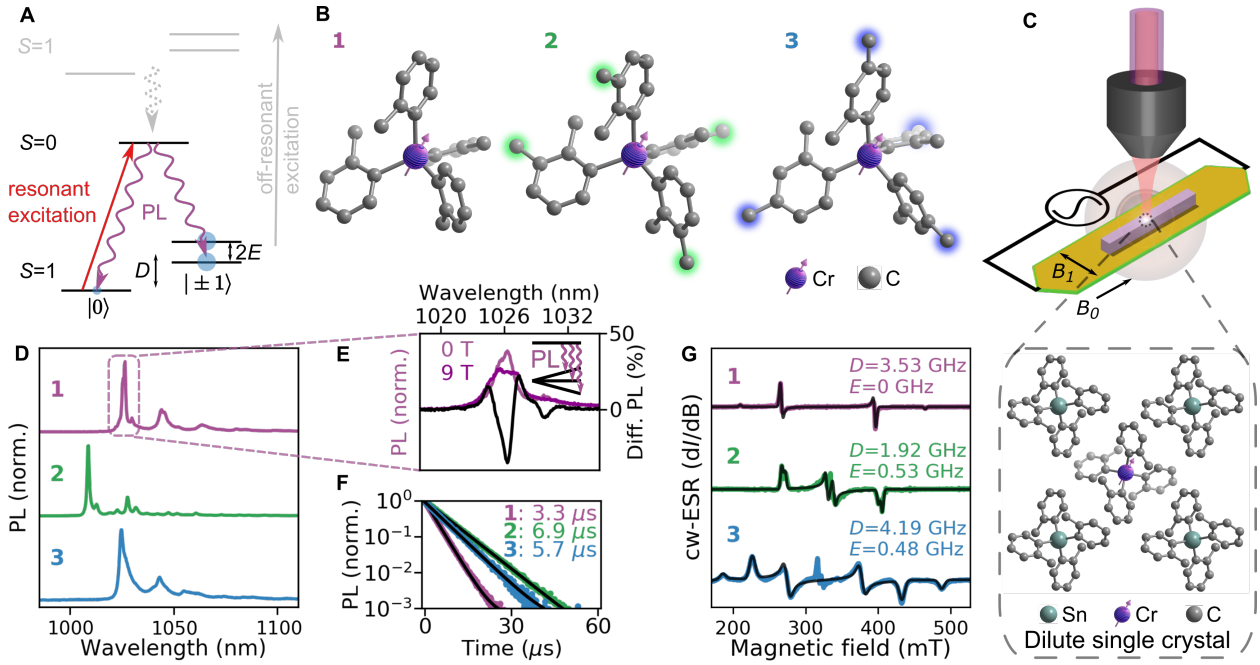

Figure 4.2. Experimental setup and sample characterization. **(A)** Tetrahedral Cr^{4+}(o-tolyl)$_4$ complexes exhibit a triplet ground state, with the spin sublevels separated by the zero-field splitting parameters D and E. Resonant excitation can pump the triplet ground state into the singlet excited state, from which it decays phosphorescently. Furthermore, off-resonant excitation can drive a spin-conserving transition into a triplet excited state, which rapidly decays into the singlet state via intersystem crossing. **(B)** Chemical structure of **1**-**3**, where small chemical changes in the coordinating ligands allow for the generation of a broader class of complexes. Hydrogens are omitted for simplicity. **(C)** Experimental schematic. The sample (purple needle-like crystal) is placed on a coplanar waveguide structure which provides a AC magnetic field B_1, while a permanent magnet can be used to apply a static field B_0. The sample can be excited with either resonant or off-resonant lasers (purple). Sample luminescence (red) is collected by a microscope objective and measured using a detector (not shown). **(D)** 785nm excitation spin-flip phosphorescence spectrum of **1**-**3**, following 785nm excitation. All samples emit spectrally narrow luminescence with a sharp zero-phonon line. **(F)** The long optical lifetimes of **1-3** indicate long-lived phosphorescence with characteristic lifetimes of 3.3-6.9μs. **(G)** Continuous wave electron spin resonance experiments allow determination of the zero-field splitting parameters for **1**-**3**.

cannot fully resolve the various spin sublevels optically, but this can be demonstrated in analogous systems with spectrally narrower emission [99].

4.1.2.3 Optical lifetimes

Next, we characterized the photophysical properties of **1**-**3** using time-domain measurements as shown in in Figure 4.2F under off-resonant excitation with λ =785nm. We observe long, monoexponential optical lifetimes of 3.3 - 6.9μs, which are consistent with the spin-flip phosphorescence process proposed in Section 4.1.2.1. We can explain this result with a simple model of (1) vibrationally-allowed triplet-triplet absorption followed by (2) rapid intersystem crossing into an intermediate singlet state and then (3) long-lived phosphorescence. For (2), El-Sayed's rule predicts that the intersystem crossing should proceed rapidly due to the single change in orbital configuration and the relatively large spin orbit coupling.

4.1.2.4 ESR data

We characterize the ground state spin of **1**-**3** using X-band continuous-wave electron spin resonance in in Figure 4.2G. As these measurements were taken in the absence of optical excitation, the data indicate a $S = 1$ ground state for **1**-**3** with a non-zero zero-field splitting. As discussed in Section 2.3.4, this zero field splitting arises from the combination of both spin-orbit coupling and small distortions away from tetrahedral symmetry. Crucially, due to the reasonably strong spin-orbit coupling of transition metals, these deviations from ideal symmetry must be fairly small to allow them to be addressed with conventional X-band spectroscopy ($f \sim$ 9GHz) and commonly available microwave electronics used in our experiments (0.1 - 6 GHz). Notably, compound **1** is the highest symmetry (approximately D_{2d}) and has $E \approx 0$ to within our experimental resolution. In contrast, both **2** and **3** have $E \neq 0$, resulting from a rhombic distortion that lowers the symmetry.

4.2 Spin-state initialization of 1

In this section, we demonstrate optical spin initialization of **1** through frequency-selective resonant pumping. We begin with a brief discussion of molecular photophysics under resonant excitation, depicted schematically in Figure 4.3A. For **1,** the triplet ground state spin sublevels $|0\rangle$ and $|\pm 1\rangle$ are energetically separated by the zero-field splitting $|D|$. This zero-field splitting introduces a small anisotropy in the transition frequency between the $|0\rangle$ and $|\pm 1\rangle$ sublevels and the singlet excited state. In addition, the transition frequencies between the triplet states and the singlet state for the ensemble are inhomogeneously broadened due to strain. In contrast to the off-resonant case, resonant absorption is not mediated by phonons, and therefore is highly frequency selective, pumping only a subensemble that lies on resonance with the probe laser tone.

4.2.1 PLE

However, the picture outlined in Figure 4.3A is a bit simplistic, as our sample is comprised of an ensemble of molecules in a host matrix. Each molecule in the ensemble experiences a distinct local environment, which can shift its optical transition frequencies slightly. Though an individual molecule may be only broadened homogeneously, these shifted transition frequencies produce inhomogeneous broadening for the ensemble. This process is schematically depicted in the inset of Figure 4.3C, whereby the zero-phonon line is comprised of a sum of many homogeneously broadened lines with small frequency shifts. We characterize this inhomogeneous broadening for **1** by measuring the ensemble absorption spectrum in Figure 4.3B. While sweeping the frequency of a narrow-line laser, we measure the amount of phonon side band emission in order to measure the inhomogeneous linewidth (~150GHz) of the sample. These data indicate that different spins in the ensemble experience a range of local environments, which slightly shifts the optical transition energies of different spins within the ensemble.

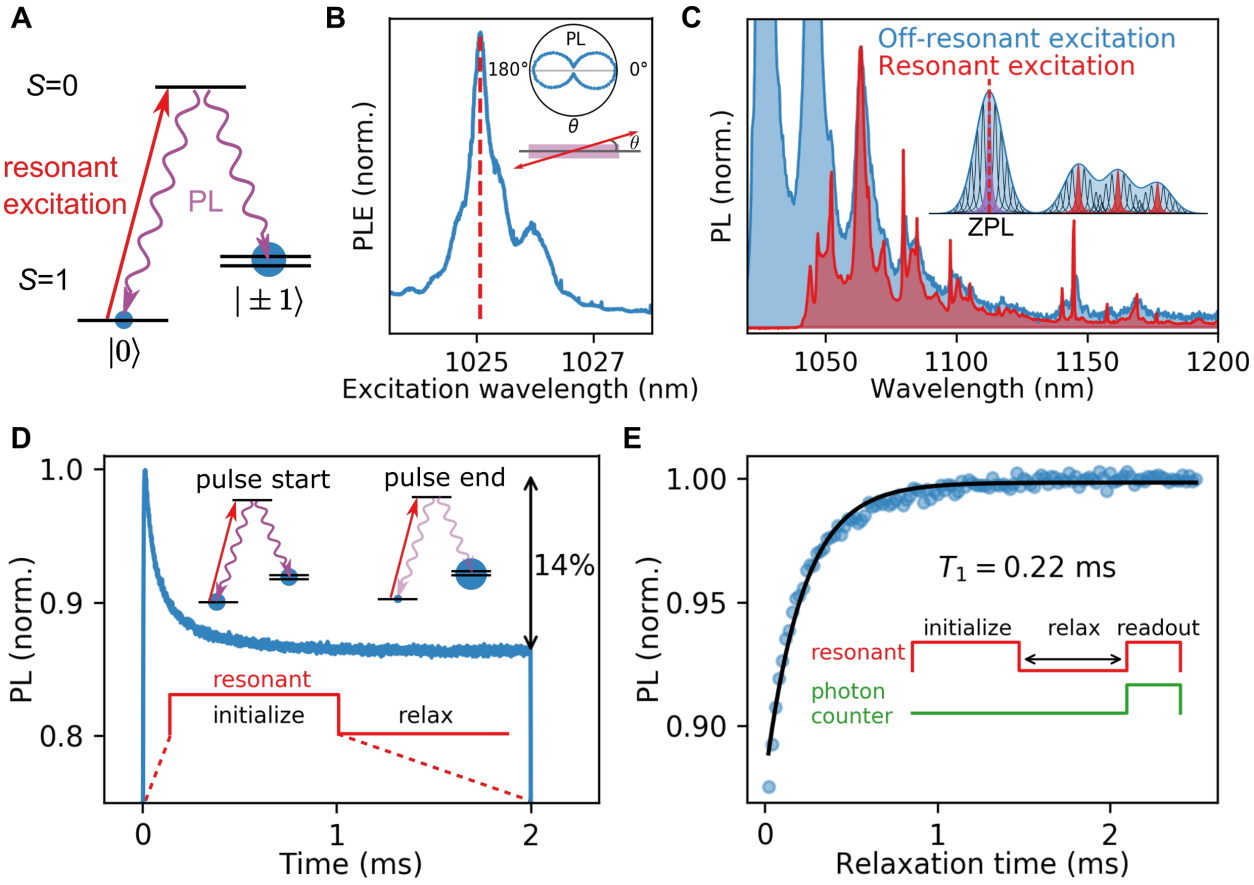

Figure 4.3. Optical initialization of **1** using resonant excitation. **(A)** Schematic of resonant excitation. The resonant laser pumps population from a probed sublevel (e.g.$|0\rangle$) into the singlet excited state. The population then decays into the unprobed sublevels ($|\pm 1\rangle$) through phosphorescence, resulting in preferential population of spin sublevels. **(B)** Photoluminescence excitation (PLE) sweep and polarization dependence (inset). **(C)** Optical emission spectra under off-resonant (blue) and resonant (red) excitation. The observed emission line narrowing indicates that the resonant laser only probes spins with transitions on resonance with the laser frequency, rather than the inhomogenously broadened ensemble. **(D)** Resonant hole burning of **1**. The resonant laser pulse pumps population out of the probed sublevel(s) into the unprobed sublevel(s), resulting in non-equilibrium spin polarization. **(E)** Spin-lattice relaxation of **1**. By varying the time between initialization and readout pulses (inset) and measuring the resulting decay to equilibrium, we obtain a spin-lattice relaxation timescale $T_1 = 0.22$ms.

4.2.2 Emission line narrowing

Though it would seem that the large inhomogeneous linewidths presented in Figure 4.3B ($>> D$) would preclude spin-selective readout, here we show that resonant excitation pumps a narrower subensemble of spins, which permits spin-selective readout. To show that resonant excitation only pumps a subensemble of spins, we measure the luminescence spectrum of **1** under off-resonant and resonant excitation in Figure 4.3C. As previously mentioned, off-resonant excitation drives a spin-conserving triplet-triplet transition, where absorption is mediated through emission of host lattice phonons or molecular vibrational modes. Off-resonant excitation therefore excites the whole molecular ensemble, yielding the inhomogeneously broadened spectrum (blue) in Figure 4.3C. In contrast, resonant excitation yields the line-narrowed emission spectrum (red) in Figure 4.3C, where only the subensemble lying on resonance with the laser is pumped. The narrow vibrational peaks (spectrometer-limited) are indicative of a much narrower central absorption feature decorated by sharply-defined vibrational modes. Though we do not characterize the linewidth of these peaks directly, these indicate that a narrower subensemble, is being probed as the linewidth is bounded by the convolution of the absorption linewidth and vibrational mode (Figure 4.3C inset).

4.2.3 Hole burning

Returning briefly to Figure 4.3A, our goal is to optically initialize the spin by preferentially populating a spin sublevel. We demonstrate this experimentally using a transient hole burning measurement. The measurement is shown schematically in Figure 4.3D. A long initialization laser pulse pumps the subensemble of spins that lie on resonance with the laser tone. At the start of the resonant laser pulse, the populations of the spin sublevels are in thermal equilibrium and the spin unpolarized. Applying the narrow-line laser pumps the resonant subensemble into the singlet state, from which it is free to decay (non-preferentially) into any of the triplet spin sublevels. In the case that the spin returns to the spin sublevel lying on resonance, it is repumped again into the excited state. However, if the spin returns to a different, unprobed spin sublevel (lying off resonance), it cannot be repumped and does not return to the singlet excited state. As this process repeats multi-

ple times, a net spin polarization builds up in the unprobed sublevels which lie off resonance with the laser.

4.2.4 All-optical T_1

Finally, we can characterize the spin-lattice relaxation time T_1 using an all-optical measurement sequence. We use a long initialization pulse to polarize the molecular spin subensemble, wait a variable time τ, and then measure the optical emission after a final readout pulse. Two limiting cases are informative for interpreting the experimental data. In the $\tau = 0$ limit, the optical emission is identical to that at the end of the hole burning pulse (where the spin is polarized). In the long τ limit, the spin ensemble has relaxed to thermal equilibrium, and the optical emission reverts back to the emission at the beginning of the hole burning pulse. Thus, measuring the optical emission as a function of the delay time τ provides both a measure of the spin relaxation time T_1 and the spin polarization P. An all-optical measurement of the spin-lattice relaxation time is shown in Figure 4.3D, indicating $T_1 \sim 220\mu$s.

4.2.5 Rate equation model

Finally, we can construct a simple rate equation model to estimate the steady-state spin polarization and contrast. We ignore coherences between levels, and consider three processes: spin-dependent optical pumping, excited-state decay, and spin-lattice relaxation. Denoting the populations of the triplet levels as n_0, n_{+1}, and n_{-1}, and the population of the singlet excited state as n_e, we can model our system with the following coupled rate equations:

$$\dot{n}_0 = -g_0 n_0 + \frac{\gamma_{\text{opt}}}{3} n_e + \frac{\gamma_{T_1}}{2} \left[(n_{+1} - n_0) + (n_{-1} - n_0) \right] \tag{4.2}$$

$$\dot{n}_{+1} = -g_1 n_1 + \frac{\gamma_{\text{opt}}}{3} n_e - \frac{\gamma_{T_1}}{2} (n_{+1} - n_0) \tag{4.3}$$

$$\dot{n}_{-1} = -g_{-1} n_{-1} + \frac{\gamma_{\text{opt}}}{3} n_e - \frac{\gamma_{T_1}}{2} (n_{-1} - n_0) \tag{4.4}$$

$$\dot{n}_e = g_0 n_0 + g_1 n_1 + g_{-1} n_{-1} - \gamma_{\text{opt}} n_e \tag{4.5}$$

where $\{g_i\}$ are the spin-dependent pumping rates for the triplet levels $i = 0, -1, +1$, $\gamma_{\text{opt}} = T_{\text{opt}}^{-1}$ is the optical decay rate, and $\gamma_{T_1} = T_1^{-1}$ is the spin-lattice relaxation rate. (We assume equal decay rates from the singlet state to the three spin sublevels.) In the following discussion, we take pumping from the $|\pm 1\rangle$ levels to be equal i.e. $g_{-1} = g_{+1} \to g_{\pm 1}$.

Solving this equation in the steady state (i.e. $\dot{n}_i \to 0$) yields a relatively straightforward expression for the steady-state spin polarization:

$$P = \frac{n_{\pm 1} - n_0}{n_{\pm 1} + n_0} = \frac{(g_0 - g_{\pm 1})}{(g_0 + g_1 + 3\gamma_{T_1})} \tag{4.6}$$

In addition, we can extract the optical contrast from the difference between the polarized and maximally mixed ($\gamma_{T_1} \to \infty$) limits:

$$C = \frac{2 (g_0 - g_{\pm 1})^2 \gamma_{\text{opt}}}{3 \left(3\gamma_{\text{opt}} + g_0 + 2g_{\pm 1}\right) \left(g_{\pm 1}\gamma_{T_1} + g_0 \left(g_{\pm 1} + \frac{1}{2}\gamma_{T_1}\right)\right)} \tag{4.7}$$

Thus, the optical contrast depends quadratically on the optical pump anisotropy (i.e. $\sim (g_0 - g_1)^2$), while the polarization exhibits only a linear dependence.

Substituting in our estimated values for $g_0, g_{\pm 1}$, γ_{opt}, and γ_{T_1} yields a estimates of $P = 28\%$ and $C = 19\%$, where the latter is in reasonable agreement with Figure 4.3D.

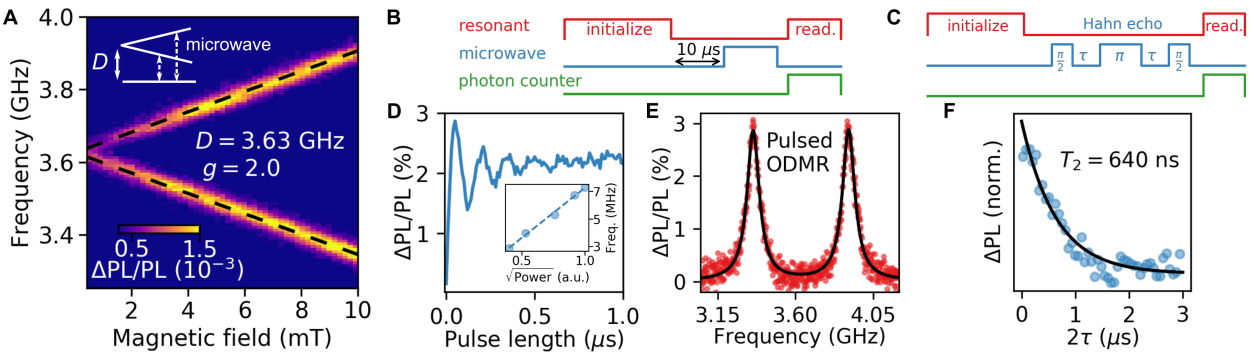

Figure 4.4. Optically addressing the spin state of **1**. **(A)** ODMR field and frequency dependence for **1**, indicating a ZFS of 3.63GHz and g ~ 2. **(B)** Pulse sequence used for Rabi and pulsed ODMR measurements. **(C)** Pulse sequence used for Hahn echo measurements. The final $\pi/2$ pulse rotates the coherences into population for optical readout. **(D)** Coherent control of **1**, showing the expected oscillations as the pulse length is increased. The linear dependence of the Rabi frequency shows the expected $\sqrt{\text{Power}}$ dependence **(D** inset). **(E)** Pulsed ODMR measurements with a 10μs delay time indicate that we coherently manipulate the ground state spin. **(F)** Hahn echo indicates a pin coherence time of T_2 =640ns.

4.3 Coherent control of 1

In this section, we demonstrate coherent control of **1** in Figure 4.4, thereby establishing it as an optically addressable $S = 1$ molecular spin qubit. We start with field and frequency-dependent optically-detected magnetic resonance (ODMR) measurements to characterize the ground state spin. Next, we use pulsed excitation and microwave control to manipulate the spin and measure its coherence properties. We demonstrate coherent control of the spin by measuring Rabi oscillations, and use a spin echo measurement to characterize the spin lifetime.

4.3.1 ODMR

In Figure 4.4 we measure continuous-wave optically detected resonance of **1**. A resonant laser drive pumps a subensemble of spins into the optically dark state in the presence of a continuous microwave drive. When the microwave drive tone is resonant with the spin transition frequency, population is coherently driven back into the probed sublevel, resulting in an increase in optical emission. Therefore, our optically detected magnetic resonance signal is unambiguously positive.

In addition, though the spin is polarized in the sense that the sublevels are no longer thermally populated, this mechanism does not necessarily preferentially populate a specific spin state, so all possible spin transitions ($|0\rangle \leftrightarrow |\pm 1\rangle$ and $|0\rangle \leftrightarrow |\pm\rangle$ in the $E \neq 0$ case) can be observed providing the microwave drive is sufficiently strong and well-aligned to the spin magnetic dipole moment.

We use a permanent magnet on a motorized stage to provide a variable static magnetic field. Changing the magnetic field changes the Zeeman term in the spin Hamiltonian, thereby changing the resonant microwave transition frequencies. We use a slow, square-wave modulation of the microwaves to permit lock-in detection. In Figure 4.4A, we show the change in optical emission as a function of applied magnetic field and microwave drive frequency. The zero-field splitting and observation of Zeeman splitting as a function of magnetic field provide evidence for the expected $S = 1$ ground state. In addition, these data show a zero-field splitting of ~ 3.63GHz and an electron g-factor g~2, in good agreement with our results from conventional electron spin resonance.

4.3.2 Rabi driving

Next, we demonstrate coherent control of **1** through Rabi oscillation measurements. As depicted in Figure 4.4B, a long resonant laser initialization pulse optically polarizes the spin subensemble, followed by a wait of 10μs (to ensure decay from the singlet into the ground state). Following the wait, a resonant microwave pulse of variable duration τ drives transitions from the probed sublevel into the unprobed sublevel. The change in optical emission as a function of pulse width τ is presented in Figure 4.4D. These data show Rabi oscillations consistent with coherent driving of the spin state, where the emission increases as the spin is driven from the unprobed sublevel back into the probed sublevel, and decreases again as the microwave drive continues to drive the spin back into the probed sublevel. In addition, we extract the Rabi frequency Ω_R as a function of the microwave drive power and obtain the expected $\sqrt{\text{Power}}$ dependence (Figure 4.4D inset).

4.3.3 Pulse ODMR

Next, using the pulse sequence depicted in Figure 4.4B and choosing the pulse width τ that maximizes the PL contrast, we can sweep the microwave drive frequency to measure pulsed ODMR of the ground state spin. Notably, the delay time of $10\mu s >> T_{opt} = 3.3\mu s$ indicates that we drive the ground state spin, as population has decayed into the ground state following the delay. In addition, this measurement allows us to estimate the spin transition linewidth ($\Delta f \sim$42MHz) which implies a T_2^* of approximately 8ns.

4.3.4 T_2

Finally, we can measure the spin coherence time T_2 by initializing the spin into a superposition state and measuring the time it takes the superposition to decay. For solid-state spins, a dominant source of dephasing is magnetic field noise resulting from random fluctuations of nearby spins. When fluctuations are sufficiently slow, this dephasing can be canceled out by driving a π-pulse. We implement this experimentally using the pulse sequence depicted in Figure 4.4C, which is a modified Hahn echo sequence with an additional $\pi/2$ pulse that projects the coherences back into populations, which can be read out optically. The optical emission as a function of function of delay τ is shown in Figure 4.4F, showing a spin coherence time T_2 of 640ns. Though not impressive compared to other spin qubits, longer coherence times have been demonstrated in other molecular spin systems probed through conventional electron spin resonance, and molecular design offers a straightforward pathway to improve this figure in future work.

4.4 Optically detected magnetic resonance of $1-3$

Finally, we demonstrate that our optical initialization and readout method applies to a general class of Cr^{4+} complexes. Synthetic chemistry allows chemical substitution of one of the hydrogens on the coordinating ligands with a methyl group, which lowers the molecular symmetry. We show experimentally that these chemical substitutions introduce changes in the zero-field splittings,

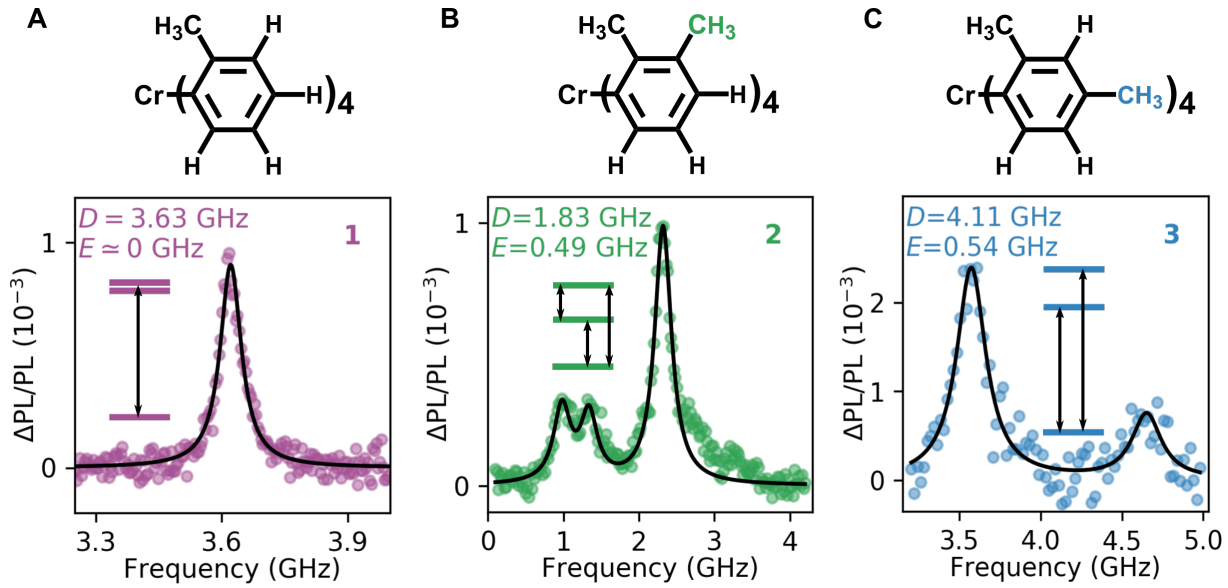

Figure 4.5. Optically detected magnetic resonance of **1-3**. **(A)** ODMR of **1** (highest symmetry) shows $E \approx 0$ and degeneracy between $|\pm 1\rangle$. In **(B)** and **(C)**, chemical substitution of a methyl group for one of the ligand hydrogens lowers the local symmetry to rhombic, yielding $E \neq 0$. This yields three distinct spin transition frequencies: $D \pm E$ and $2E$. **(B)** ODMR of 2 shows $|D| \sim 1.83$GHz and $E \sim 0.49$GHz. **(C)** For **3**, the methyl group position is changed relative to **2**, resulting in different zero-field splitting parameters $D \sim 4.11$GHz and $E \sim 0.54$GHz.

changing D and introducing $E \neq 0$ due to the rhombic distortion. By applying our measurement procedure from Section 4.3, we can can demonstrate optically-detected magnetic resonance of this broader class of compounds **1-3**, as shown in Figures 4.5B and 4.5C.

Importantly, we see reasonable agreement between zero-field splitting parameters measured by both optically detected magnetic resonance and conventional electron spin resonance in Table 4.1.

	D (GHz)		E (GHz)	
	ESR	ODMR	ESR	ODMR
1	3.53	3.63	–	–
2	1.92	1.83	0.53	0.49
3	4.19	4.11	0.48	0.54

Table 4.1: Comparison of zero-field splitting parameters D and E obtained via optically detected magnetic resonance (ODMR) and electron spin resonance (ESR).

4.5 Conclusions

To our knowledge, this work represents the first optical readout of a ground state spin, thereby extending optical spin and initialization methods from the solid-state to the field of molecular spins. In addition, we show that this method is not exclusive to just a single Cr^{4+} complex, showing that a broader class of molecular spin systems can be initialized and read out. We show that changing the coordinating ligands provides a means to adjust the zero-field splitting and optical emission energies. Though this chapter focuses just on Cr^{4+} compounds, this resonant readout approach should be generalizable to a variety of metal-organic complexes (both transition metal and rare-earth ions), provided the ground state has a sufficiently long spin lifetime T_1 and the homogeneous linewidth is smaller than the energetic splitting between spin sublevels.

CHAPTER 5

OFF-RESONANT INITIALIZATION AND READOUT OF CR^{4+} MOLECULAR SPINS

Abstract Molecular spin qubits are an emerging platform for quantum information processing and sensing. For many solid-state spins, such as the negatively-charged NV center in diamond and the neutral divacancy in silicon carbide, an off-resonant optical interface to initialize and read-out the spin is often advantageous. However, optically-addressable molecular spins currently rely on frequency-selective excitation of spectrally narrow transitions [100]. In this work, we demonstrate off-resonant optical initialization of the ground state spin of the pseudo-tetrahedral complex Cr^{4+}(2,3-dimethyphenyl)$_4$ via spin-dependent pumping and compare to the resonant interface case. We propose a theoretical model to explain how this spin-dependent pumping can arise from the combination of spin-orbit coupling and polarization selection rules for tetrahedral organometallic complexes. Finally, we conclude by discussing molecular design strategies that may improve the performance of the spin-selectivity of optical interface demonstrated here.

5.1 Introduction

Molecular spin qubits are an emerging platform for quantum information processing and sensing. Recently, optical interfaces for molecular spins have been demonstrated [100,101] but these rely on frequency-selective excitation to selectively pump specific spin states. These interfaces provide a high contrast optical readout mechanism for ground state spins, but the need for narrow optical linewidths introduces the requirement for cryogenic temperatures and spectrally narrow laser sources. In contrast, many solid-state defect spins offer a robust off-resonant optical interface, which allows for room-temperature operation and the ability to use commonly-available laser sources. In this work, we develop an off-resonant initialization and readout scheme for the molecular spin Cr^{4+}(2,3-dimethyphenyl)$_4$ using polarization selection rules. We demonstrate the ability to initialize and read-out the spin off-resonantly, comparing to the resonant case. We propose a

simple model that explains our experimental results and suggest several methods to improve the quality of the spin-photon interface.

Metal-organic complexes of transition metal ions can be described using ligand field theory, whereby the energy levels of the bare metallic ion are perturbed through coordination to the surrounding ligands. In this work, we have focused on a homoleptic, pseudo-tetrahedral complex Cr^{4+}(2,3-dimethyphenyl), whose structure as determined by X-ray diffraction measurements is shown in Figure 5.1B.

A molecular orbital diagram of the complex is shown in Figure 5.1C. Under complexation, the metal t_2 orbitals hybridize with the ligand σ orbitals, resulting in t_2 bonding and t_2^* antibonding orbitals. The two d-electrons then nominally occupy the e non-bonding orbitals ($d_{x^2-y^2}$ and d_{z^2}) for both the ground state triplet and singlet excited state. Due to its spin-flip nature, the transition from the ground state into the singlet excited state is spectrally narrow and directly accessible using a narrow line laser. The first (second) triplet excited state is roughly comprised of promotion of one (both) electron into the t_2^* antibonding orbitals. Since this transition is spin-conserving, population can be pumped into these triplet states using broad vibrationally-mediated absorption.

Cr^{4+}(2,3-dimethyphenyl)$_4$ and Sn(2,3-dimethyphenyl)$_4$ compounds were synthesized and co-crystallized following the procedure in [100]. This process provides a low-disorder host, permitting spectrally narrow optical transitions into the singlet state at low temperatures.

Off-resonant 785nm laser excitation pumps population into the first triplet excited state. Due to the single orbital configuration change, El-Sayed's rule predicts rapid intersystem crossing (ISC) into the singlet excited state, similar to the photophysics observed in isoelectronic vanadium complexes [99]. As the singlet excited state and ground state occupy the same orbital configuration, ISC proceeds slowly out of the singlet, and the decay is predominantly via phosphorescence. The phosphorescence spectrum in Figure 5.1D shows a well-resolved zero-phonon line (ZPL) with several sharp phonon side band features corresponding to vibrational modes of the complex and the host matrix. We characterized the optical emission lifetime and spectrum of the compound. A

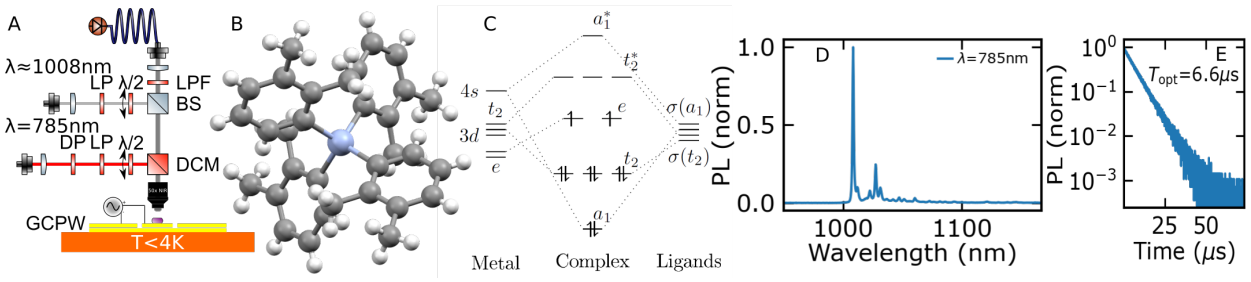

Figure 5.1. Experimental setup and characterization of Cr^{4+}(2,3-dimethylphenyl)$_4$. (A) Schematic of confocal microscope used for experiments. (B) Structure of Cr^{4+}(2,3-dimethylphenyl)$_4$ determined by x-ray diffraction measurements. (C) Molecular orbital diagram for pseudo-tetrahedral Cr^{4+} complexes. (D) Optical emission spectrum of Cr^{4+}(2,3-dimethylphenyl)$_4$ under off-resonant excitation, showing ZPL at ~ 1008nm. (E) Optical lifetime of Cr^{4+}(2,3-dimethylphenyl)$_4$ under off-resonant excitation, showing an optical lifetime of 6.6μs.

simplified schematic of the experimental setup is shown in Figure 5.1A and a more detailed description of the experimental apparatus can be found in Appendix B. Figure 5.1E shows the sample optical lifetime, indicative of a phosphorescence lifetime of 6.6μs.

5.2 Spin initialization and readout

Having outlined the basic photophysical considerations and experimental setup, we demonstrate two separate schemes to perform optical spin initialization using spin-dependent pumping. We show how spin state-dependent pumping can be accomplished using frequency-selective resonant excitation, or through polarization-selective off-resonant excitation. Importantly, this work represents the first demonstration of off-resonant optical spin initialization of a molecular spin qubit.

We depict the spin-dependent photophysical schemes used in this work in Figure 5.2A and Figure 5.2B. In Figure 5.2A, a narrow-line laser (linewidth $<<$ $|D|$) drives the triplet to singlet transition for the subensemble of spins on resonance with the laser frequency. As mentioned previously, decay from the singlet excited state into the ground state is mediated via phosphorescence, and nominally populates all spin sublevels at an equal rate. However, as the spin sublevel energies are separated by the zero-field splitting energy $|D|$ and E, this introduces a detuning away from resonance and therefore anisotropic pump rates. Therefore, the effect of a long pulse with

the narrow-line laser is to burn a hole, as population is pumped out of the spin sublevel with the highest pump rate into the dark sublevels with lower pump rates.

Our off-resonant initialization and readout scheme is similarly depicted in Figure 5.2B. In this case, off-resonant excitation pumps the spin-conserving triplet-triplet transition, with a broad absorption spectrum resulting from the vibronic modes of the molecule and lattice phonons of the host matrix. In the orbital occupancy picture, the triplet excited state consists of electrons populating one of the t_2^* anti-bonding orbitals and one of the e non-bonding orbitals. The specific orbitals that are occupied following absorption depend on the polarization of the incident light. Due to the single orbital configuration change, we expect rapid intersystem crossing and therefore spin-dependent ISC would not induce off-resonant spin polarization (in contrast to solid-state systems such as NV^- and VV^0 where spin-dependent ISC is competitive with fluorescence). Instead of spin-dependent ISC, spin-initialization must therefore rely again on spin-dependent pump rates, which result from polarization selection rules in this case. A more detailed theoretical model to explain these spin-dependent pump rates is given in Section 5.4.2.

First, we demonstrate spin-state initialization by monitoring the time evolution of phosphorescence under the hole-burning pulse shown in Figure 5.2. At the beginning of the pulse, the spin ensemble is unpolarized and therefore a certain amount of phosphorescence is emitted. As population is pumped out of the brighter spin-state (spin polarization), the total phosphorescence decreases as less population is pumped into the singlet excited state. The results for resonant and off-resonant excitation are depicted in Figure5.2D and Figure 5.2E respectively. Notably, under orthogonal polarization, no hole burning was observed for off-resonant excitation, indicating that spin initialization and readout are mediated by polarization selection rules in the off-resonant case.

5.3 Optically detected magnetic resonance

Finally, we demonstrate optical spin polarization and microwave manipulation using optically detected magnetic resonance (ODMR) measurements. We present the ODMR spectrum under resonant and off-resonant excitation in Figures 5.3A and 5.3C respectively. We monitor the opti-

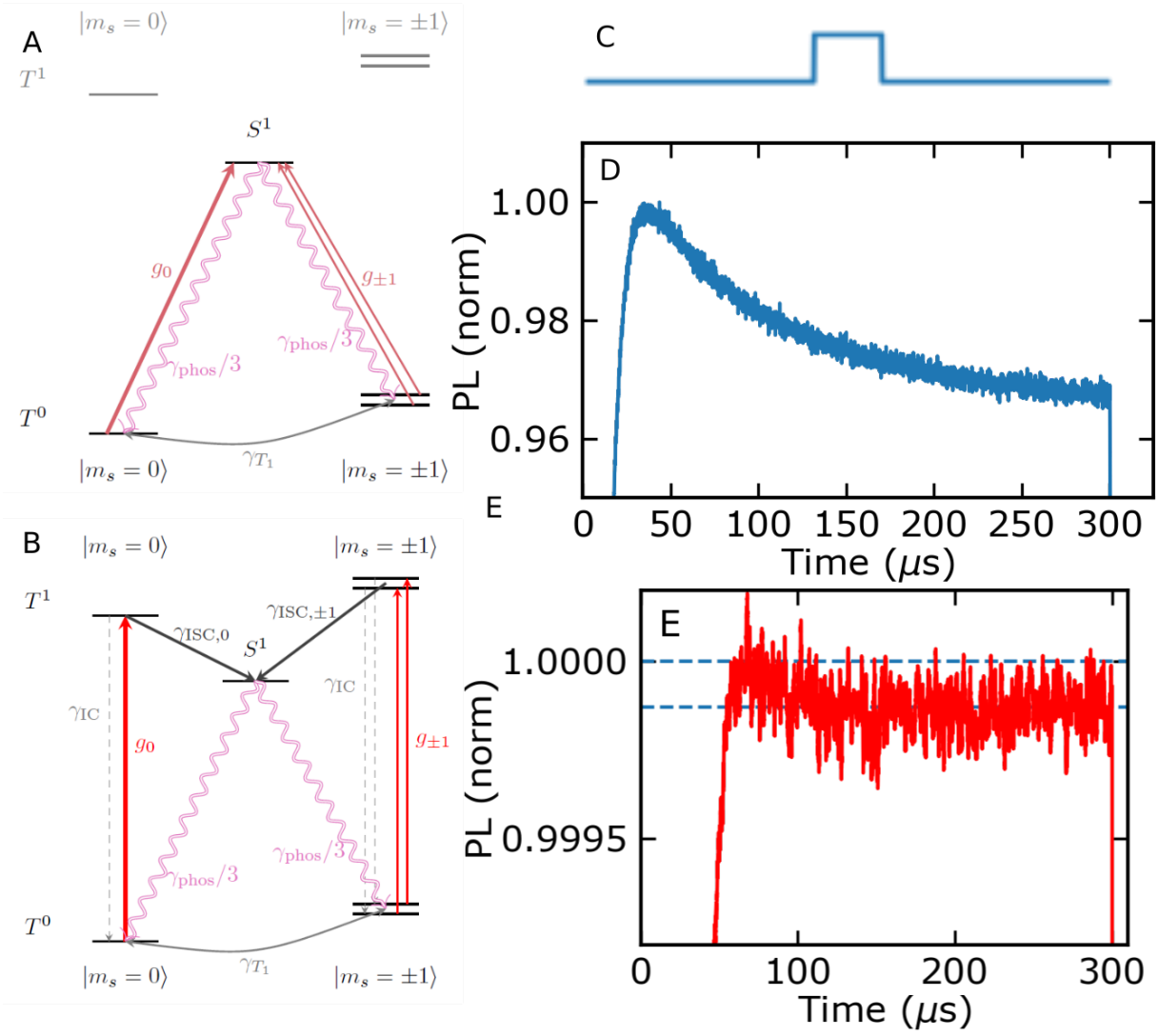

Figure 5.2. Optical initialization and readout of Cr^{4+}(2,3-dimethylphenyl)$_4$. (A) Spin-dependent photophysical schematic under resonant excitation. A narrow-line laser pumps the subensemble of spins on resonance with the laser tone, pumping them into the dark, unprobed spin sublevel. (B) Spin-dependent photophysical schematic under off-resonant excitation. Off-resonant excitation introduces a spin-dependent pump strength using polarization selection rules. (C) Pulse sequence used for both resonant and off-resonant hole burning experiments. The time evolution of emission is monitored using time-correlated single photon counting. (D) Resonant hole burning of Cr^{4+}(2,3-dimethylphenyl)$_4$. (E) Off-resonant hole burning of Cr^{4+}(2,3-dimethylphenyl)$_4$.

cal emission under continuous-wave optical excitation and a variable frequency microwave field, which drives spin transitions. We used a lock-in sequence on the microwave drive in order to make all measurements differential. For the off-resonant case (to avoid heating artifacts), lock-in measurements were taken at the probe microwave frequency and a baseline frequency, then subtracted. Importantly, our theoretical model accounts for the observed microwave transitions and the optical polarization dependence of ODMR signal in both cases.

For the resonant case, hole burning polarizes the subensemble of spins whose optical transition frequencies are on resonance with the laser, regardless of the specific spin multiplicity. The microwave drive then pumps population back into the bright, probed sublevel, so in principle all spin transitions can be observed. In contrast, the mechanism we propose to explain the off-resonant spin-dependent contrast pumps population into $|\pm\rangle$. The readout mechanism then amounts to measuring the population difference between $|\pm\rangle$ and $|0\rangle$, so the $2E$ transition cannot be observed.

5.4 Theoretical model

In this section, we propose a theoretical model based on ligand field theory to explain the observed spin-dependent contrast under $\hat{z}$-polarized excitation. By considering an admixture of the first excited state introduced by spin-orbit coupling, our model provides a mechanism for spin-dependent pumping under off-resonant excitation. In addition, using perturbation theory, we determine the lowest-order terms to account from the zero-field splitting, which results from a combination of spin-orbit coupling and symmetry lowering from T_d symmetry.

We start by applying a tetrahedral ligand field of form:

$$\begin{aligned}\langle L, M_L|H_{\mathrm{LF}}|L'M'_L\rangle = \quad & (-1)^l\sqrt{(2l+1)(2l+1)}\langle L|\mathbf{U}^{(k)}|L'\rangle \\ & \sum_{k,q}(-1)^{L-M_L}\begin{pmatrix} L & k & L' \\ -M_L & q & M'_L\end{pmatrix}B_q^{(k)}\end{aligned} \tag{5.1}$$

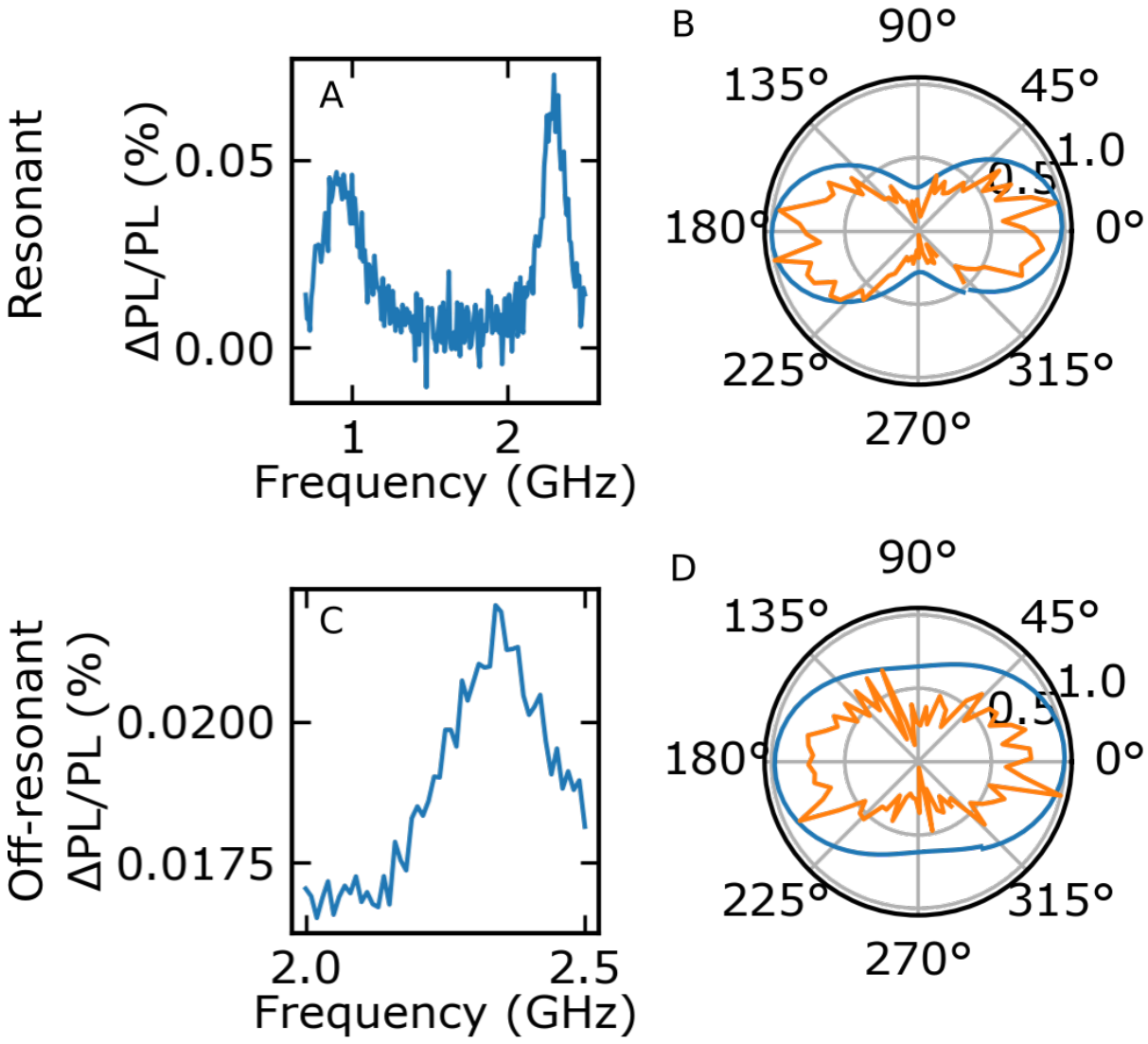

Figure 5.3. Optically-detected magnetic resonance of Cr^{4+}(2,3-dimethylphenyl)$_4$. (A) Resonant optically-detected magnetic resonance of Cr^{4+}(2,3-dimethylphenyl)$_4$. In principle, all three microwave transitions can be observed ($D \pm E$ and $2E$) but the microwave drive geometry only permits observation of the $D+E$ and $2E$ transitions. (B) Polarization dependence of off-resonant optically-detected magnetic resonance for Cr^{4+}(2,3-dimethylphenyl)$_4$. The optical emission and ODMR signals have an identical polarization dependence. (C) Off-resonant optically-detected magnetic resonance of Cr^{4+}(2,3-dimethylphenyl)$_4$. We only observe the $D+E$ transition, which we attribute to the fact that our off-resonant polarization mechanism gives the same optical emission for $|+\rangle$ and $|-\rangle$. (D) Polarization dependence of off-resonant optically-detected magnetic resonance for Cr^{4+}(2,3-dimethylphenyl)$_4$. The ODMR signal has a strong polarization dependence, indicating that polarization selection rules are important for the spin-dependent optical contrast.

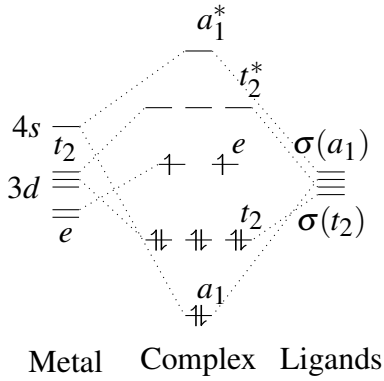

Figure 5.4. Molecular orbital diagram for tetrahedral Cr^{4+}. The spin triplet ground state consists of occupation of two lowest energy orbitals ($d_{x^2-y^2}$ and d_{z^2}). These orbitals are non-bonding e orbitals and thus do not significantly hybridize with the ligands. The t_2^* ligands hybridize with the ligands, which introduces a small amount of p-character, increasing the strength of electric dipole transitions to the first triplet excited state, where one of the electrons is promoted to the t_2^* orbitals.

where the crystal field parameters $B_q^{(k)}$s follow strict tetrahedral symmetry (i.e. $B_0^{(4)} = -21|Dq|$ and $B_{\pm 4}^{(4)} = \sqrt{\frac{5}{14}} B_0^{(4)}$)

Denoting our eigenstates in the $|L, M_L\rangle$ basis, we obtain the canonical d^2 spin-triplet states:

$$|g\rangle = \frac{1}{\sqrt{2}}\left(|3,-2\rangle - |3,+2\rangle\right) = |(d_{z^2})(d_{x^2-y^2})|$$

$$|k_{T_2}^{(0)}\rangle = \begin{cases} \psi_{T_2,a} &= \frac{1}{4}\left(\sqrt{10}|3,-1\rangle - \sqrt{6}|3,+3\rangle\right) \\ \psi_{T_2,b} &= \frac{1}{\sqrt{2}}\left(|3,-2\rangle + |3,+2\rangle\right) \\ \psi_{T_2,c} &= \frac{1}{4}\left(-\sqrt{10}|3,+1\rangle + \sqrt{6}|3,-3\rangle\right) \end{cases} \tag{5.2}$$

$$|k_{T_1}^{(0)}\rangle = \begin{cases} \psi_{T_1,a} &= |3,0\rangle \\ \psi_{T_1,b} &= \frac{1}{4}\left(\sqrt{6}|3,-1\rangle + \sqrt{10}|3,+3\rangle\right) \\ \psi_{T_1,c} &= \frac{1}{4}\left(\sqrt{10}|3,-3\rangle + \sqrt{6}|3,+1\rangle\right) \end{cases}$$

where the first two excited states each have a threefold orbital degeneracy.

Next, we consider symmetry lowering from T_d, which breaks the degeneracy of these orbital excited states. We can consider their behavior under an additional set of crystal field parameters

corresponding to the low-symmetry perturbation denoted $\tilde{B_q^{(k)}}$:

$$\begin{aligned}\langle L, M_L|H_{\text{dist}}|L'M'_L\rangle = \quad & (-1)^l\sqrt{(2l+1)(2l+1)}\langle L|\mathbf{U}^{(k)}|L'\rangle \\ & \Sigma_{k,q}(-1)^{L-M_L}\begin{pmatrix} L & k & L' \\ -M_L & q & M'_L\end{pmatrix}\tilde{B}_q^{(k)}\end{aligned} \tag{5.3}$$

where we admit all possible $\tilde{B}_q^{(k)}$s (assuming non-triclinic / monoclinic / trigonal symmetries): $\tilde{B}_0^{(2)}, \tilde{B}_{\pm 2}^{(2)}, \tilde{B}_0^{(4)}, \tilde{B}_{\pm 2}^{(4)}, \tilde{B}_{\pm 4}^{(4)}$

Following the rule of degenerate perturbation theory, we construct the matrix $\langle k^{(0)}|V_{\text{dist}}|l^{(0)}\rangle$ in both cases by running over the ${}^3T_2$ and ${}^3T_1$ subspaces respectively.

$$\langle k_{T_2}^{(0)}|V_{\text{dist}}|l_{T_2}^{(0)}\rangle = \begin{bmatrix} -\frac{\tilde{B}_0^{(4)}}{12}+\frac{\sqrt{70}\tilde{B}_4^{(4)}}{28} & 0 & -\frac{\sqrt{10}}{6}\tilde{B}_2^{(4)} \\ 0 & \frac{\tilde{B}_0^{(4)}}{3}-\frac{\sqrt{70}\tilde{B}_4^{(4)}}{21} & 0 \\ -\frac{\sqrt{10}}{6}\tilde{B}_2^{(4)} & 0 & -\frac{\tilde{B}_0^{(4)}}{12}+\frac{\sqrt{70}\tilde{B}_4^{(4)}}{28} \end{bmatrix} \tag{5.4}$$

and

$$\langle k_{T_2}^{(0)}|V_{\text{dist}}|l_{T_2}^{(0)}\rangle = \begin{bmatrix} \frac{4}{35}\tilde{B}_0^{(2)}-\frac{2\tilde{B}_0^4}{7} & 0 & 0 \\ 0 & \frac{-2}{35}\tilde{B}_0^{(2)}-\frac{3}{28}\tilde{B}_0^{(4)}-\frac{\sqrt{70}}{28}\tilde{B}_4^{(4)} & \frac{-2\sqrt{6}}{35}\tilde{B}_2^{(2)}-\frac{\sqrt{10}}{14}\tilde{B}_2^{(4)} \\ 0 & \frac{-2\sqrt{6}}{35}\tilde{B}_2^{(2)}-\frac{\sqrt{10}}{14}\tilde{B}_2^{(4)} & \frac{-2}{35}\tilde{B}_0^{(2)}-\frac{3}{28}\tilde{B}_0^{(4)}-\frac{\sqrt{70}}{28}\tilde{B}_4^{(4)} \end{bmatrix} \tag{5.5}$$

We can calculate the energy splittings of the ${}^3T_2$ first excited state under this symmetry-lowering operation to first order as:

$$\begin{aligned} E_+ =& \frac{-1}{12}\tilde{B}_0^{(4)}-\frac{\sqrt{10}}{6}\tilde{B}_2^{(4)}+\frac{\sqrt{70}}{28}\tilde{B}_4^{(4)} \\ E_0 =& \frac{1}{3}\tilde{B}_0^{(4)}-\frac{\sqrt{70}}{21}\tilde{B}_4^{(4)} \\ E_- =& \frac{-1}{12}\tilde{B}_0^{(4)}+\frac{\sqrt{10}}{6}\tilde{B}_2^{(4)}+\frac{\sqrt{70}}{28}\tilde{B}_4^{(4)} \end{aligned} \tag{5.6}$$

as well as the eigenstates in the $|L,M_L\rangle$ basis:

$$
\begin{aligned}
{}^3T_2^+ &= \frac{1}{\sqrt{2}}\left(\psi_{T_2,a}+\psi_{T_2,b}\right) = \frac{1}{4}\left(\sqrt{3}|3,-3\rangle+\sqrt{5}|3,-1\rangle-\sqrt{5}|3,+1\rangle-\sqrt{3}|3,+3\rangle\right)\\
{}^3T_2^0 &= \frac{1}{\sqrt{2}}\left(|3,-2\rangle+|3,+2\rangle\right)\\
{}^3T_2^- &= \frac{1}{\sqrt{2}}\left(-\psi_{T_2,a}+\psi_{T_2,b}\right) = \frac{1}{4}\left(\sqrt{3}|3,-3\rangle-\sqrt{5}|3,-1\rangle-\sqrt{5}|3,+1\rangle+\sqrt{3}|3,+3\rangle\right)
\end{aligned}
\tag{5.7}
$$

For the second ${}^3T_1$ excited state, the eigenvalues of the matrix of $\langle k_{T_2}^{(0)}|V_{\text{dist}}|l_{T_2}^{(0)}\rangle$ depends on the specific parameter values. Therefore the ${}^3T_1^{\pm}$ state composition depends a bit more specifically on the parameters of the splitting, but could be constructed as a linear combination following:

$$
\begin{aligned}
|{}^3T_1^0\rangle &= |3,0\rangle\\
|{}^3T_1^+\rangle &= c_b^+|\psi_{T_{1,b}}\rangle + c_c^+|\psi_{T_{1,,c}}\rangle\\
|{}^3T_1^-\rangle &= c_b^-|\psi_{T_{1,,b}}\rangle + c_c^-|\psi_{T_{1,,c}}\rangle
\end{aligned}
\tag{5.8}
$$

where $c_b^{\pm}$ and $c_c^{\pm}$ are coefficients satisfying $|c_b^{+(-)}|^2+|c_c^{+(-)}|^2=1$.

5.4.1 Perturbation theory - zero field splitting and wavefunctions

For the ground state spin, we aim to calculate the zero-field splitting parameters D and E that emerge from a combination of symmetry-lowering and spin-orbit coupling to break the degeneracy of the spin-sublevels. In addition, using perturbation theory, we can compute the first-order correction to the wavefunction. Our objective is to compute the zero field splitting in terms of the spin-orbit coupling and a general symmetry-lowering distortion $V = H_{\text{SO}} + H_{\text{dist}}$. For a perturbation V on some unperturbed eigenstate $|n^{(0)}\rangle$, we can expand the energy corrections up to third order with the series:

$$
E_n(\lambda) = E_n^{(0)} + \lambda E_n^{(1)} + \lambda^2 E_n^{(2)} + \lambda^3 E_n^{(3)} + \mathscr{O}(\lambda^4) \tag{5.9}
$$

Our first order correction term is just the expectation value of the perturbation on the original eigenstates. The higher order correction terms are given by a sums over the other eigenstates $|k^{(0)}\rangle, |m^{(0)}\rangle, |n^{(0)}\rangle$, divided by the applicable splittings $E_n^{(0)} - E_k^{(0)}$:

$$\begin{aligned}
E_n^{(0)} &= E_n^{(0)} \\
E_n^{(1)} &= \langle n^{(0)}|V|n^{(0)}\rangle \\
E_n^{(2)} &= \sum_{k\neq n} \frac{|\langle k^{(0)}|V|n^{(0)}\rangle|^2}{E_n^{(0)} - E_k^{(0)}} \\
E_n^{(3)} &= \sum_{k\neq n}\sum_{m\neq n} \frac{|\langle n^{(0)}|V|m^{(0)}\rangle\langle m^{(0)}|V|k^{(0)}\rangle\langle k^{(0)}|V|n^{(0)}\rangle}{(E_n^{(0)} - E_m^{(0)})(E_n^{(0)} - E_k^{(0)})} \\
&\quad - \langle n^{(0)}|V|n^{(0)}\rangle \sum_{m\neq n} \frac{|\langle n^{(0)}|V|m^{(0)}\rangle|^2}{(E_n^{(0)} - E_m^{(0)})^2}
\end{aligned} \tag{5.10}$$

The wavefunctions can be similarly expanded as a series according to:

$$|n(\lambda)\rangle = |n^{(0)}\rangle + \lambda \sum_{k\neq n} |k^{(0)}\rangle \frac{\langle k^{(0)}|V|n^0\rangle}{E_n^{(0)} - E_k^{(0)}} + \mathscr{O}(\lambda^2) \tag{5.11}$$

To avoid the need to perform a multivariate expansion, we consider a general perturbation that includes both the spin-orbit interaction and a symmetry-lowered ligand field: $V = H_{\text{SO}} + H_{\text{dist}}$ where

$$H_{\text{SO}} = \tfrac{1}{2}\lambda_{xy}(L_+S_- + L_-S_+) + \lambda_z L_z S_z \tag{5.12}$$

and H_{dist} is the Hamiltonian for a generic symmetry-lowered distortion, previously given in Equation 5.3.

First order energy splitting For the ground state, $|n^{(0)}\rangle = |g\rangle \otimes |\chi_i\rangle$, where the $|\chi_i\rangle$s are the different spin eigenstates. We can separate the perturbation into the distortion and spin-orbit com-

ponents:

$$\langle n^{(0)}|V|n^0\rangle = \langle n^{(0)}|H_{\text{dist}}|n^{(0)}\rangle + \underbrace{\cancel{\langle n^{(0)}|H_{\text{SO}}|n^0\rangle}}_{\langle g|L_z|g\rangle=\langle g|L_\pm|g\rangle=0} \tag{5.13}$$

The symmetry-lowering term yields the matrix element gives:

$$E_n^{(1)} = \frac{1}{3}B_0^{(4)} + \frac{\sqrt{70}}{21}B_4^4 \to \frac{1}{3}\left(B_0^{(4)} + 2\sqrt{\frac{5}{14}}B_4^4\right), \tag{5.14}$$

which is the same for each of the spin sublevels, as H_{dist} acts only on the orbital degree of freedom.

First order wavefunction The first order wavefunctions under the perturbation can be expanded into the sum:

$$|n(\lambda)\rangle = |n^{(0)}\rangle + \lambda \sum_{k\neq n} |k^{(0)}\rangle \frac{\langle k^{(0)}|V|n^0\rangle}{E_n^{(0)} - E_k^{(0)}} + \mathscr{O}(\lambda^2) \tag{5.15}$$

We start by trying to find all non-zero values of $\langle k^{(0)}|V|n^{(0)}\rangle$. In general, the symmetry-lowering distortion does not mix the ground state with any of the excited states: $\langle k^{(0)}|H_{\text{dist}}|n^{(0)}\rangle = 0$, so we don't need to consider those terms here. (Note that this is independent of our basis choice, and holds for an arbitrary linear combination of the degenerate basis functions $\sum_i c_i|\psi_i\rangle$.) In contrast to the symmetry lowering distortion, the spin-orbit interaction can mix the ground and ${}^3T_2$ first excited state. There is no mixing with the second ${}^3T_1$ excited state, however. We can calculate the non-zero matrix elements $\langle k^{(0)}|V|n^{(0)}\rangle$ (working in the $|0\rangle, |\pm\rangle$ basis, which reduces the number of non-zero terms) as:

$$\begin{aligned}
\langle k^{(0)}|H_{\text{SO}}|g,+\rangle &: \langle k^{(0)}|\{2|\psi_0\rangle|-\rangle, 2|\psi_+\rangle|0\rangle\} \\
\langle k^{(0)}|H_{\text{SO}}|g,0\rangle &: \langle k^{(0)}|\{2|\psi_+\rangle|+\rangle, -2|\psi_-\rangle|-\rangle\} \\
\langle k^{(0)}|H_{\text{SO}}|g,-\rangle &: \langle k^{(0)}|\{2|\psi_0\rangle|+\rangle, 2|\psi_-\rangle|0\rangle\}
\end{aligned} \tag{5.16}$$

Therefore, our wavefunctions are given (up to normalization) by:

$$
\begin{aligned}
&|g,+\rangle + \frac{2\zeta}{10|Dq|}\left(|\psi_0\rangle|-\rangle + |\psi_+\rangle|0\rangle\right) \\
&|g,0\rangle + \frac{2\zeta}{10|Dq|}\left(|\psi_+\rangle|+\rangle - |\psi_-\rangle|-\rangle\right) \\
&|g,-\rangle + \frac{2\zeta}{10|Dq|}\left(|\psi_0\rangle|+\rangle + |\psi_-\rangle|0\rangle\right)
\end{aligned}
\tag{5.17}
$$

We can lower bound the amount of mixing for Cr^{4+}(2,3-dimethylphenyl)$_4$ according to $\frac{2\zeta}{10|Dq|} \sim \frac{2(325-335\text{cm}^{-1})}{(12700\text{cm}^{-1})} \sim 5\%$, where $12700\text{cm}^{-1} \approx 785\text{nm}$, which is squarely in the absorption band (and therefore $10|Dq|$ is in fact smaller).

Second order energy splitting Now we aim to compute the second-order energy splitting, given by:

$$
E_n^{(2)} = \sum_{k \neq n} \frac{|\langle k^{(0)}|V|n^{(0)}\rangle|^2}{E_n^{(0)} - E_k^{(0)}} \tag{5.18}
$$

where the sum runs over the excited states $|k^{(0)}\rangle$. We previously calculated the matrix elements non-zero matrix elements $\langle k^{(0)}|V|n^{(0)}\rangle$, which emerge only due to the spin-orbit mixing between the ground and first excited states. However, to get the change in energy for each of the spin sublevels, we sum over the square of these matrix elements and obtain the result that our perturbation shifts all spin sublevels equally up to second order:

$$
\begin{aligned}
E_{g,+}^{(2)} &= \frac{8\zeta^2}{10|Dq|} \\
E_{g,0}^{(2)} &= \frac{8\zeta^2}{10|Dq|} \\
E_{g,-}^{(2)} &= \frac{8\zeta^2}{10|Dq|}
\end{aligned}
\tag{5.19}
$$

Third order energy splitting Since the first and second order terms did not account for the ZFS, we now consider the third-order term:

$$E_n^{(3)} = \sum_{k\neq n}\sum_{m\neq n} \frac{\frac{|\langle n^{(0)}|V|m^{(0)}\rangle\langle m^{(0)}|V|k^{(0)}\rangle\langle k^{(0)}|V|n^{(0)}\rangle}{(E_n^{(0)}-E_m^{(0)})(E_n^{(0)}-E_k^{(0)})} - \underbrace{\langle n^{(0)}|V|n^{(0)}\rangle \sum_{m\neq n} \frac{|\langle n^{(0)}|V|m^{(0)}\rangle|^2}{(E_n^{(0)}-E_m^{(0)})^2}}_{\text{spin-independent}}} \tag{5.20}$$

We know that we only have $\langle k^{(0)}|V|n^{(0)}\rangle \neq 0$ for the spin-orbit interaction with the T_2 states. Therefore we only need to consider the spin-orbit interaction with the first excited state for the $\langle k^{(0)}|V|n^{(0)}\rangle$ and $\langle n^{(0)}|V|m^{(0)}\rangle$ portions of this expression. The second half of this expression is proportional to $E^{(2)}$ and therefore doesn't have any-spin dependence. Thus we can ignore it in our calculation of the ZFS. The middle term $\langle m^{(0)}|V|k^{(0)}\rangle$ in principle could include both the spin-orbit interaction between the ${}^3T_2$ states, and the symmetry-lowering H_{dist}. However, we know that spin-coupling by itself is insufficient to explain ZFS, so we don't compute this term explicitly here, as it only can contribute to higher order. In handling the degeneracy of the ${}^3T_2$ state, we already calculated the energies $\{E_+ =, E_0, E_-\}$ and respective eigenvectors $\{|\psi_+\rangle, |\psi_0\rangle, |\psi_-\rangle\}$, which gives a diagonal form for $\langle m^{(0)}|H_{\text{dist}}|k^{(0)}\rangle$. This reduces us to calculating the sum over:

$$\sum_{k\neq n}\sum_{m\neq n} \frac{\langle n^{(0)}|H_{\text{SO}}|\overbrace{m^{(0)}\rangle\langle m^{(0)}}^{{}^3T_2}|H_{\text{dist}}|\overbrace{k^{(0)}\rangle\langle k^{(0)}}^{{}^3T_2}|H_{\text{SO}}|n^{(0)}\rangle}{10|Dq|^2} \tag{5.21}$$

For each of the spin sublevels, we can expand this out:

$$
\begin{aligned}
E_{g,+}^{(3)} &= \sum_{k\in{}^3T_2}\sum_{m\in{}^3T_2}\frac{4\zeta^2}{(E_m^{(0)}-E_n^{(0)})(E_k^{(0)}-E_n^{(0)})}\left[\{\langle\psi_0|\langle -|,\langle\psi_+|\langle 0|\}\,|H_{\text{dist}}\{|\psi_0\rangle|-\rangle,|\psi_+\rangle|0\rangle\}\right] \\
&= \frac{4\zeta^2(E_0+E_+)}{(10|Dq|)^2} \\
E_{g,0}^{(3)} &= \sum_{k\in{}^3T_2}\sum_{mk\in{}^3T_2}\frac{4\zeta^2}{(E_m^{(0)}-E_n^{(0)})(E_k^{(0)}-E_n^{(0)})}\left[\{\langle\psi_+|\langle +|,-\langle\psi_-|\langle -|\}\,|H_{\text{dist}}\{|\psi_+\rangle|+\rangle,-|\psi_-\rangle|-\rangle\}\right] \\
&= \frac{4\zeta^2(E_++E_-)}{(10|Dq|)^2} \\
E_{g,-}^{(3)} &= \sum_{k\in{}^3T_2}\sum_{mk\in{}^3T_2}\frac{4\zeta^2}{(E_m^{(0)}-E_n^{(0)})(E_k^{(0)}-E_n^{(0)})}\left[\{\langle\psi_0|\langle +|,\langle\psi_-|\langle 0|\}\,|H_{\text{dist}}\{|\psi_0\rangle|+\rangle,|\psi_-\rangle|0\rangle\}\right] \\
&= \frac{4\zeta^2(E_0+E_-)}{(10|Dq|)^2}
\end{aligned}
\tag{5.22}
$$

This allows us to compute the zero field splitting (up to third order) as:

$$
\begin{aligned}
D &= \frac{1}{2}\left(E_{g,+}^{(3)}+E_{g,+}^{(3)}\right)-E_{g,0}^{(3)} = \frac{4\zeta^2}{(10|Dq|)^2}\left(\frac{1}{4}B_0^{(4)}+\frac{\sqrt{70}}{84}B_4^{(4)}\right) \\
E &= E_{g,+}^{(3)}-E_{g,-}^{(3)} = \frac{4\zeta^2}{(10|Dq|)^2}\left(\frac{\sqrt{10}}{3}B_2^{(4)}\right)
\end{aligned}
\tag{5.23}
$$

A more detailed calculation up to fourth order using the perturbation loop method [102] is presented in [103] introduces additional higher-order corrections that can contribute additional terms to the zero field splitting. However, the third order calculation presented here is sufficient to explain the origins of the ZFS.

5.4.2 Spin-dependent pumping

Finally, we aim to combine our knowledge of the perturbed ground states with electric dipole selection rules to understand the polarization-dependence of our spin-dependent contrast. Denoting the Slater determinant of two orbitals ϕ_a and ϕ_b as $|(\phi_a)(\phi_b)|$, our triplet ground state in the $|L,M_L\rangle$

basis is given by:

$$|(d_{z^2})(d_{x^2-y^2})| = \frac{1}{\sqrt{2}}(|3,-2\rangle - |3,+2\rangle) \tag{5.24}$$

These two orbitals are non-bonding, and therefore do not hybridize appreciably with the ligands. However, our t_2^* orbitals, which are involved in the excited states, are free to hybridize with the ligands. This hybridization introduces some $s-$ and $p-$character to these orbitals. The latter character is responsible for allowing the electric dipole transition, as it allows the parity change. We know that the electric dipole operator only acts on the orbital degree of freedom. Therefore any spin-dependent pumping must be mediated by spin-orbit coupling. To understand the impact of the spin-orbit coupling on our electric dipole transition strengths, we substitute in our wavefunctions, correct to first-order:

$$\begin{aligned} &|g,+\rangle + \frac{2\zeta}{10|Dq|}(|\psi_0\rangle|-\rangle + |\psi_+\rangle|0\rangle) \\ &|g,0\rangle + \frac{2\zeta}{10|Dq|}(|\psi_+\rangle|+\rangle - |\psi_-\rangle|-\rangle) \\ &|g,-\rangle + \frac{2\zeta}{10|Dq|}(|\psi_0\rangle|+\rangle + |\psi_-\rangle|0\rangle) \end{aligned} \tag{5.25}$$

If instead, we were in the $|0\rangle, |\pm 1\rangle$ basis:

$$\begin{aligned} |g,0\rangle &\qquad |g,0\rangle + \frac{2}{10|Dq|}\left(|\psi_+\rangle\frac{1}{\sqrt{2}}(|+1\rangle + |-1\rangle) - |\psi_-\rangle\frac{1}{\sqrt{2}}(|+1\rangle - |-1\rangle)\right) \\ |g,+1\rangle = \frac{1}{\sqrt{2}}(|+\rangle + |-\rangle) &\qquad = |g,+1\rangle + \frac{2}{10|Dq|}\left(|\psi_0\rangle|+1\rangle + \frac{1}{\sqrt{2}}(|\psi_+\rangle + |\psi_-\rangle)|0\rangle\right) \\ |g,-1\rangle = \frac{1}{\sqrt{2}}(|+\rangle - |-\rangle) &\qquad = |g,-1\rangle + \frac{2}{10|Dq|}\left(-|\psi_0\rangle|-1\rangle + \frac{1}{\sqrt{2}}(|\psi_+\rangle - |\psi_-\rangle)|0\rangle\right) \end{aligned} \tag{5.26}$$

H_{ed}	$\lvert\psi_+\rangle$	$\lvert\psi_0\rangle$	$\lvert\psi_-\rangle$	$T_1^0 = \lvert(d_{xz})(d_{yz})\rvert$	$T_1^a = \lvert(d_{xy})(d_{yz})\rvert$	$T_1^b = \lvert(d_{xy})(d_{xz})\rvert$
$\lvert g^{(0)}\rangle = \lvert(d_{x^2-y^2})(d_{z^2})\rvert$	$\hat{x}$	$\hat{z}$	$\hat{y}$	–	–	–
$\lvert\psi_+\rangle = \frac{\sqrt{3}}{2}\lvert(d_{x^2-y^2})(d_{yz})\rvert - \frac{1}{2}\lvert(d_{z^2})(d_{yz})\rvert$	–	–	–	$\hat{y}$	$\hat{z}$	–
$\lvert\psi_0\rangle = \lvert(d_{z^2})(d_{xy})\rvert$	–	–	–	–	$\hat{x}$	$\hat{y}$
$\lvert\psi_-\rangle = \frac{\sqrt{3}}{2}\lvert(d_{x^2-y^2})(d_{xz})\rvert + \frac{1}{2}\lvert(d_{z^2})(d_{xz})\rvert$	–	–	–	$\hat{x}$	–	$\hat{z}$

Table 5.1: Tabulated Electric dipole selection rules for tetrahedral d^2 complex. Transitions from the unperturbed ground state $|g^{(0)}\rangle \rightarrow^3 T_1$ require configuration change for both electrons and are forbidden to first order. Electric dipole transitions cannot occur between orbitals of $^3T_2$, but we are free to have $^3T_2 \rightarrow^3 T_1$ transitions.

We can decompose our ground and first excited state into the orbital functions (see Equations 6-31 and 6-33 of [75]):

$$
\begin{aligned}
|g\rangle &= \frac{1}{\sqrt{2}}\left(|3,-2\rangle - |3,+2\rangle\right) = |(d_{z^2})(d_{x^2-y^2})| \\
|\psi_+\rangle &= \frac{1}{4}\left(\sqrt{3}|3,-3\rangle + \sqrt{5}|3,-1\rangle - \sqrt{5}|3,c+1\rangle - \sqrt{3}|3,+3\rangle\right) = \frac{\sqrt{3}}{2}|(d_{x^2-y^2})(\tilde{d_{yz}})| - \frac{1}{2}|(d_{z^2})(\tilde{d_{yz}})| \\
|\psi_0\rangle &= \frac{1}{\sqrt{2}}\left(|3,-2\rangle + |3,+2\rangle\right) = |(d_{z^2})(\tilde{d_{xy}})| \\
|\psi_-\rangle &= \frac{1}{4}\left(\sqrt{3}|3,-3\rangle - \sqrt{5}|3,-1\rangle - \sqrt{5}|3,+1\rangle + \sqrt{3}|3,+3\rangle\right) = \frac{\sqrt{3}}{2}|(d_{x^2-y^2})(\tilde{d_{xz}})| + \frac{1}{2}|(d_{z^2})(\tilde{d_{xz}})|
\end{aligned}
\tag{5.27}
$$

We can then tabulate the allowed transitions in Table 5.1, noting that allowed transitions have a single change in orbital configuration and are equal in strength:

5.4.2.1 Polarization dependence

Finally, we explicitly compute the polarization-dependent pump strength for each of the spin sublevels.

$E \neq 0$ case: When the polarization is along $\hat{z}$:

$$
\begin{aligned}
|g,+\rangle =&|(d_{z^2})(d_{x^2-y^2})||+\rangle \quad &+\frac{2}{10|Dq|}\left(\cancel{|\psi_0\rangle|-\rangle}+|\psi_+\rangle|0\rangle\right)\\
|g,0\rangle =&|(d_{z^2})(d_{x^2-y^2})||0\rangle \quad &+\frac{2}{10|Dq|}\left(|\psi_+\rangle|+\rangle-|\psi_-\rangle|-\rangle\right)\\
|g,-\rangle =&|(d_{z^2})(d_{x^2-y^2})||-\rangle \quad &+\frac{2}{10|Dq|}\left(\cancel{|\psi_0\rangle|+\rangle}+|\psi_-\rangle|0\rangle\right)
\end{aligned}
\tag{5.28}
$$

In this case, the pump strength is strongest for $|0\rangle \rightarrow g_0 > g_\pm$, so pumping leads to a net polarization into $|\pm\rangle$.

For polarization along $\hat{x}$:

$$
\begin{aligned}
|g,+\rangle =&|(d_{z^2})(d_{x^2-y^2})||+\rangle \quad &+\frac{2}{10|Dq|}\left(|\psi_0\rangle|-\rangle+\cancel{|\psi_+\rangle|0\rangle}\right)\\
|g,0\rangle =&|(d_{z^2})(d_{x^2-y^2})||0\rangle \quad &+\frac{2}{10|Dq|}\left(\cancel{|\psi_+\rangle|+\rangle}-|\psi_-\rangle|-\rangle\right)\\
|g,-\rangle =&|(d_{z^2})(d_{x^2-y^2})||-\rangle \quad &+\frac{2}{10|Dq|}\left(|\psi_0\rangle|+\rangle+|\psi_-\rangle|0\rangle\right)
\end{aligned}
\tag{5.29}
$$

For polarization along $\hat{y}$:

$$
\begin{aligned}
|g,+\rangle =&|(d_{z^2})(d_{x^2-y^2})||+\rangle \quad &+\frac{2}{10|Dq|}\left(|\psi_0\rangle|-\rangle+|\psi_+\rangle|0\rangle\right)\\
|g,0\rangle =&|(d_{z^2})(d_{x^2-y^2})||0\rangle \quad &+\frac{2}{10|Dq|}\left(|\psi_+\rangle|+\rangle-\cancel{|\psi_-\rangle|-\rangle}\right)\\
|g,-\rangle =&|(d_{z^2})(d_{x^2-y^2})||-\rangle \quad &+\frac{2}{10|Dq|}\left(|\psi_0\rangle|+\rangle+\cancel{|\psi_-\rangle|0\rangle}\right)
\end{aligned}
\tag{5.30}
$$

$E = 0$ *case:* When the polarization is along $\hat{z}$:

. First, we determine the composition of the ${}^3T_1$ and ${}^3T_2$ states

$$
\begin{aligned}
&= |g,+1\rangle + \frac{2}{10|Dq|}\left(\cancel{|\psi_0\rangle|+1\rangle}+\frac{1}{\sqrt{2}}\left(|\psi_+\rangle+|\psi_-\rangle\right)|0\rangle\right)\\
|g,0\rangle + \frac{2}{10|Dq|}&\left(|\psi_+\rangle\frac{1}{\sqrt{2}}\left(|+1\rangle+|-1\rangle\right)-|\psi_-\rangle\frac{1}{\sqrt{2}}\left(|+1\rangle-|-1\rangle\right)\right)\\
&= |g,-1\rangle + \frac{2}{10|Dq|}\left(\cancel{-|\psi_0\rangle|-1\rangle}+\frac{1}{\sqrt{2}}\left(|\psi_+\rangle-|\psi_-\rangle\right)|0\rangle\right)
\end{aligned}
\tag{5.31}
$$

When the polarization is along $\hat{x}$:

$$
\begin{aligned}
&= |g,+1\rangle + \frac{2}{10|Dq|}\left(|\psi_0\rangle|+1\rangle + \frac{1}{\sqrt{2}}(\cancel{|\psi_+\rangle} + |\psi_-\rangle)|0\rangle\right) \\
|g,0\rangle + \frac{2}{10|Dq|}&\left(\cancel{|\psi_+\rangle\frac{1}{\sqrt{2}}(|+1\rangle + |-1\rangle)} - |\psi_-\rangle\frac{1}{\sqrt{2}}(|+1\rangle - |-1\rangle)\right) \\
&= |g,-1\rangle + \frac{2}{10|Dq|}\left(-|\psi_0\rangle|-1\rangle + \frac{1}{\sqrt{2}}(\cancel{|\psi_+\rangle} - |\psi_-\rangle)|0\rangle\right)
\end{aligned}
\tag{5.32}
$$

When the polarization is along $\hat{y}$:

$$
\begin{aligned}
&= |g,+1\rangle + \frac{2}{10|Dq|}\left(|\psi_0\rangle|+1\rangle + \frac{1}{\sqrt{2}}(|\psi_+\rangle + \cancel{|\psi_-\rangle})|0\rangle\right) \\
|g,0\rangle + \frac{2}{10|Dq|}&\left(|\psi_+\rangle\frac{1}{\sqrt{2}}(|+1\rangle + |-1\rangle) - |\psi_-\rangle\cancel{\frac{1}{\sqrt{2}}(|+1\rangle - |-1\rangle)}\right) \\
&= |g,-1\rangle + \frac{2}{10|Dq|}\left(-|\psi_0\rangle|-1\rangle + \frac{1}{\sqrt{2}}(|\psi_+\rangle - \cancel{|\psi_-\rangle})|0\rangle\right)
\end{aligned}
\tag{5.33}
$$

So we end up with a similar spin-dependent pumping for $\hat{z}$-polarization, even in the $|E| = 0$ case.

5.4.3 Rate equation model

Considering the spin sublevels $|0\rangle$ and $|\pm 1\rangle$ (as a single level), and denoting the laser pump rate as g_i, the intersystem crossing rates as $\gamma_{\mathrm{ISC,i}}$, the phosphorescence rate as γ_{phos}, the rate of internal conversion as γ_{IC}, and the rate of spin-lattice relaxation as $\gamma_{\mathrm{S\text{-}L}}$, we can then write down the coupled rate equations:

$$
\begin{aligned}
\dot{n_{g,0}} &= -g_0 n_{g,0} + \frac{\gamma_{\mathrm{phos}}}{3} n_s + \gamma_{\mathrm{IC}} n_{e,0} + \gamma_{\mathrm{SL}}(n_{g,\pm 1} - n_{g,0}) \\
\dot{n_{g,\pm 1}} &= -g_{\pm 1} n_{g,\pm 1} + \frac{\gamma_{\mathrm{phos}}}{3} n_s + \gamma_{\mathrm{IC}} n_{e,\pm 1} - \gamma_{\mathrm{SL}}(n_{g,\pm 1} - n_{g,0}) \\
\dot{n}_{e,0} &= g_0 n_{g,0} - \gamma_{\mathrm{ISC},0} n_{e,0} - \gamma_{\mathrm{IC}} n_{e,0} \\
\dot{n_{e,\pm 1}} &= g_{\pm 1} n_{g,\pm 1} - \gamma_{\mathrm{ISC},\pm 1} n_{e,\pm 1} - \gamma_{\mathrm{IC}} n_{e,\pm 1} \\
\dot{n}_{\mathrm{s}} &= -\gamma_{\mathrm{phos}} n_s + \gamma_{\mathrm{ISC},0} n_{e,0} + \gamma_{\mathrm{ISC},\pm 1} n_{e,\pm 1}
\end{aligned}
\tag{5.34}
$$

subject to the normalization condition $n_{g,0} + n_{g,\pm 1} + n_{e,0} + n_{e,\pm 1} + n_{\mathrm{s}} = 1$. These equations are depicted schematically in Figure 5.5.

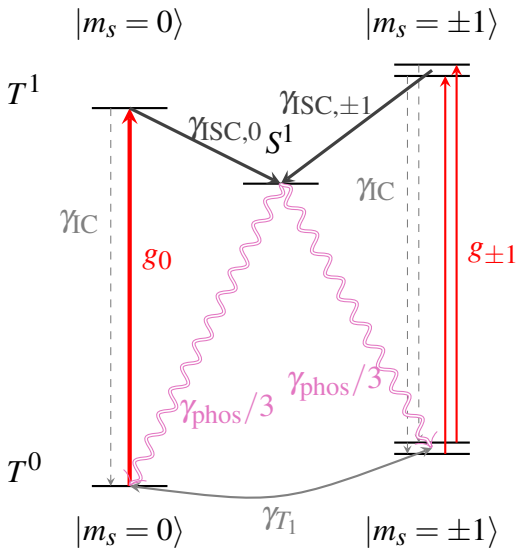

Figure 5.5. Kinetic model for tetrahedral Cr^{4+} under off-resonant excitation. Our model predicts that $g_0 > g_{\pm 1}$ under $\hat{z}$-polarized excitation, which is sufficient for optical initialization and readout, even in the absence of other spin-dependent photophysical processes.

We define the polarization as:

$$P(n_{g,0}, n_{g,\pm 1}) = \frac{n_{g,0} - n_{g,\pm 1}}{n_{g,0} + n_{g,\pm 1}} \tag{5.35}$$

The total emission is given by:

$$\mathrm{PL}(n_s) = \gamma_{\mathrm{phos}} n_{\mathrm{s}} \tag{5.36}$$

Due to the large spin-orbit coupling of transition metals, and the change in orbital type (El-Sayed's rule), we expect the intersystem crossing rate to be extremely fast in agreement with similar d^2 complexes [99]. Therefore we neglect any spin-dependence of the intersystem crossing rate. Under the condition $\gamma_{\mathrm{ISC},0} = \gamma_{\mathrm{ISC},\pm 1}$ and neglecting internal conversion ($\gamma_{\mathrm{IC}} \to 0$), we can find the steady state spin polarization as:

$$\bar{P} = \frac{g_0 - g_1}{g_0 + g_1 + 4\gamma_{\mathrm{SL}}} \tag{5.37}$$

The maximal optical contrast is given by the difference between the $\gamma_{SL} \to 0$ (no spin-lattice relaxation, full polarization) and $\gamma_{SL} \to \infty$ limits (instantaneous spin relaxation and no spin polarization). Assuming that $\gamma_{ISC} >> \gamma_{phos}$ and $g_0, g_1 << \gamma_{phos}$, we can simplify our expression for the contrast as:

$$C = \frac{(g_0 - g_{\pm 1})^2}{g_0^2 + 6 g_0 g_{\pm 1} + g_{\pm 1}^2} \tag{5.38}$$

Denoting $g_0 = g_1 g_r$, we can express this as:

$$C(g_r) = \frac{(g_r - 1)^2}{1 + g_r(6 + g_r)} \tag{5.39}$$

for $g_r \geq 1$. This has an approximately $(g_r - 1)^2$ functional dependence near $g_r \to 1$, so the contrast is quadratically sensitive to the relative pumping strength. Given the quadratic scaling, we expect approximately $\frac{C_{res}}{C_{offres}} \approx \frac{2\%}{0.05\%} \to g_{r,\text{res}} \sim 6 g_{r,\text{off-res}}$.

5.5 Conclusions and outlook

The biggest limitation of the off-resonant initialization scheme presented here is the poor degree of spin polarization and optical contrast, which are both limited by the limited spin-dependent pumping anisotropy $g_0/g_1 \sim 1$. Several experimental improvements, such as improving the sample crystallinity (so all molecules have identical orientations), and improving the alignment between the molecular dipole axis and lab frame electric field (ensuring fully $\hat{z}$-polarized light), will improve the spin-dependent pumping strength. These off-resonant experiments will also benefit from improvements in sample preparation and processing techniques for molecular spin crystals.

Next, I present a few molecular design strategies that may improve the quality of the spin-photon interface for future work. First, we can improve the optical interface by improving the spin figures of merit. From our expression for the spin polarization, increasing the spin-lattice relaxation time T_1 can improve the optically-induced spin polarization. Furthermore, increasing T_2^* (or increasing the Rabi frequency) will increase the fraction of the spin ensemble driven by the

microwave pulse, increasing the observed spin contrast. Secondly, the spin-dependent pumping mechanism presented here uses the spin-orbit interaction to produce a spin-dependent admixture of the first excited state with the ground state. Therefore, increasing the amount of admixture should increase the spin-dependence of the optical pumping strength. This admixture could be increased by enhancing the spin-orbit coupling strength by using a heavier, isoelectronic ion. Alternatively, a weaker ligand field can increase the admixture by reducing the energy splitting between the ground state and first triplet excited state, provided that the singlet state still remains intermediate in energy.

Finally, the application of polarization selection rules to spin-selective optical readout of transition metal ions remains underexplored. Though the electric dipole operator is nominally spin-conserving (acting directly on the orbital degree of freedom), the non-negligible spin-orbit coupling in transition metal ions can introduce a non-negligible spin dependence as presented. Future work may explore application of this strategy to read out molecular transition metal ions spins with $S \neq 1$.

5.6 Appendix

Here, we tabulate some results that are used as ingredients in the theoretical model section.

5.6.1 Orbital states

In Equation 5.2, we determined the composition of the triplet ground and excited states under a tetrahedral ligand field. As our electric dipole transition strengths relate to the electron occupation of different orbitals, we calculate the states corresponding to each electron configuration in the $|L, M_L\rangle$ basis here.

5.6.1.1 Triplet states

Denoting the Slater determinant of two orbitals ϕ_a and ϕ_b as $|(\phi_a)(\phi_b)|$, our triplet ground state in the $|L,M_L\rangle$ basis is given by occupation of both e orbitals as:

$$|(d_{z^2})(d_{x^2-y^2})| = \frac{1}{\sqrt{2}}\left(|3,-2\rangle - |3,+2\rangle\right) \tag{5.40}$$

We can also calculate the states corresponding to other electron orbital configurations. Note that the first triplet state is predominantly (though not entirely) one electron in an $e$orbital, with one promoted to the t_2^* orbitals:

$$\begin{aligned}
|(d_{z^2})(d_{xy})| &= \frac{-1}{\sqrt{2}}\left(|3,-2\rangle + |3,+2\rangle\right) \\
|(d_{z^2})(d_{xz})| &= \frac{1}{\sqrt{5}}\left(|3,-1\rangle + |3,+1\rangle\right) \\
|(d_{z^2})(d_{yz})| &= \frac{i}{\sqrt{5}}\left(|3,-1\rangle - |3,+1\rangle\right) \\
|(d_{x^2-y^2})(d_{xy})| &= \frac{-1}{\sqrt{5}}|3,0\rangle \\
|(d_{x^2-y^2})(d_{xz})| &= \frac{1}{2}\left(|3,-3\rangle + |3,+3\rangle\right) - \frac{\sqrt{15}}{10}\left(|3,-1\rangle + |3,+1\rangle\right) \\
|(d_{x^2-y^2})(d_{yz})| &= -i\left[\frac{1}{2}\left(|3,-3\rangle - |3,+3\rangle\right) + \frac{\sqrt{15}}{10}\left(|3,-1\rangle - |3,+1\rangle\right)\right]
\end{aligned} \tag{5.41}$$

Finally, the second triplet excited state ($^3T_1$) introduces terms resulting from both electrons occupying t_2^* orbitals:

$$\begin{aligned}
|(\tilde{d_{xy}})(\tilde{d_{xz}})| &= i\left[\frac{1}{2}\left(|3,-3\rangle - |3,+3\rangle\right) - \frac{\sqrt{15}}{10}\left(|3,-1\rangle - |3,+1\rangle\right)\right] \\
|(\tilde{d_{xy}})(\tilde{d_{yz}})| &= \frac{1}{2}\left(|3,-3\rangle + |3,+3\rangle\right) + \frac{\sqrt{15}}{10}\left(|3,-1\rangle + |3,+1\rangle\right) \\
|(\tilde{d_{xz}})(\tilde{d_{yz}})| &= \frac{2i}{\sqrt{5}}|3,0\rangle
\end{aligned} \tag{5.42}$$

In principle, this ${}^3T_1$ state has some degree of mixing with the ${}^3T_1$ state of $3P$ parentage ($3P \rightarrow T_2$) due to the ligand field, though we neglect this in our analysis here.

5.6.1.2 Metal-ligand covalency

The modified antibonding t_2 orbitals are then of form:

$$t_2^* = N \begin{cases} |\tilde{d_{xy}}\rangle & = \alpha|3d_{xy}\rangle - \sqrt{1-\alpha^2}\frac{1}{2}(\sigma_1 + \sigma_4 - \sigma_2 - \sigma_3) \\ |\tilde{d_{xz}}\rangle & = \alpha|3d_{xz}\rangle - \sqrt{1-\alpha^2}\frac{1}{2}(\sigma_1 + \sigma_2 - \sigma_3 - \sigma_4) \\ |\tilde{d_{yz}}\rangle & = \alpha|3d_{yz}\rangle - \sqrt{1-\alpha^2}\frac{1}{2}(\sigma_1 + \sigma_3 - \sigma_2 - \sigma_4) \end{cases} \tag{5.43}$$

where α is a measure of the covalency between the metal center and the ligand, the σ_is are ligand orbitals with $s-$ and $p-$ character, and N is a normalization factor.

5.6.1.3 Singlet state

The singlet state is a bit more subtle as its composition changes between the weak and strong field cases. We have the following singlet atomic terms which split under the ligand field according to:

$$\begin{aligned} {}^1S &\rightarrow A_1 \\ {}^1D &\rightarrow E, T_2 \\ \underbrace{{}^1G}_{\text{weak field}} &\rightarrow \underbrace{A_1 \oplus E \oplus T_1 \oplus T_2}_{\text{strong field}} \end{aligned} \tag{5.44}$$

The ligand field is only able to mix states of the same symmetry, so the only allowed mixings are:

$$\begin{aligned} A_1 &: {}^1S \leftrightarrow {}^1G \\ E &: {}^1D \leftrightarrow {}^1G \\ T_2 &: {}^1D \leftrightarrow {}^1G \end{aligned} \tag{5.45}$$

Strong field limit The $d_{x^2-y^2}$ and d_{z^2} orbitals are lowest in energy, so the eigenstates in the strong field limit are given by orbitally symmetric combinations of these orbitals:

$$\begin{aligned}
|d_{z^2}\rangle|d_{z^2}\rangle =& \sqrt{\frac{18}{35}}|4,0\rangle - \sqrt{\frac{2}{7}}|2,0\rangle + \frac{1}{\sqrt{5}}|0,0\rangle \\
|d_{x^2-y^2}\rangle|d_{x^2-y^2}\rangle =& \frac{1}{\sqrt{70}}|4,0\rangle + \frac{1}{2}\left(|4,-4\rangle + |4,+4\rangle\right) + \sqrt{\frac{2}{7}}|2,0\rangle + \frac{1}{\sqrt{5}}|0,0\rangle \\
\frac{1}{\sqrt{2}}\left(|d_{z^2}\rangle|d_{x^2-y^2}\rangle + |d_{x^2-y^2}\rangle|d_{z^2}\rangle\right) =& \sqrt{\frac{3}{14}}\left(|4,-2\rangle + |4,+2\rangle\right) + \sqrt{\frac{2}{7}}\left(|2,-2\rangle + |2,+2\rangle\right)
\end{aligned} \tag{5.46}$$

The third state has the required mixing between the ${}^1D \leftrightarrow {}^1G$ states, so we identify it as one of the ${}^1E$ states. We can construct the other ${}^1E$ state according to:where N is a normalization factor, A is an overlap integral common to all transitions, and α is the covalency.

$$\frac{1}{\sqrt{2}}\left(|d_{z^2}\rangle|d_{z^2}\rangle - |d_{x^2-y^2}\rangle|d_{x^2-y^2}\rangle\right) = \sqrt{\frac{5}{14}}|4,0\rangle - \frac{1}{2}\left(|4,-4\rangle + |4,+4\rangle\right) - 2\sqrt{\frac{2}{7}}|2,0\rangle \tag{5.47}$$

and the ${}^1A$ state as:

$$\frac{1}{\sqrt{2}}\left(|d_{z^2}\rangle|d_{z^2}\rangle + |d_{x^2-y^2}\rangle|d_{x^2-y^2}\rangle\right) = \sqrt{\frac{7}{10}}|4,0\rangle + \frac{1}{2}\left(|4,-4\rangle + |4,+4\rangle\right) + \frac{2}{\sqrt{5}}|0,0\rangle \tag{5.48}$$

Intermediate field limit The intermediate field states are then constructed by having the mixing between states of different atomic parentage scale according to $\frac{10|Dq|}{\Delta E}$:

$$\begin{aligned}
{}^1E :& \sqrt{1-\alpha^2}\sqrt{\frac{2}{7}}\left(|2,-2\rangle + |2,+2\rangle\right) + \alpha\sqrt{\frac{3}{14}}\left(|4,-2\rangle + |4,+2\rangle\right) \\
{}^1E :& -2\sqrt{1-\alpha^2}\sqrt{\frac{2}{7}}|2,0\rangle + \alpha\left(\sqrt{\frac{5}{14}}|4,0\rangle - \frac{1}{2}\left(|4,-4\rangle + |4,+4\rangle\right)\right) \\
{}^1A_1 :& \sqrt{1-\beta^2}\left(\sqrt{\frac{7}{10}}|4,0\rangle + \frac{1}{2}\left(|4,-4\rangle + |4,+4\rangle\right)\right) + \beta\frac{2}{\sqrt{5}}|0,0\rangle
\end{aligned} \tag{5.49}$$

where $\alpha \sim \frac{10|Dq|}{B}$ and $\beta \sim \frac{10|Dq|}{10B+C}$, and B and C are the Racah parameters.

5.6.2 Spin states

Here, we list the spin states, which come into play for the computation of the zero-field splitting using perturbation theory and the spin-orbit interaction.

Triplet states Denoting $|\uparrow\rangle \rightarrow |\alpha\rangle$ and $|\downarrow\rangle \rightarrow |\beta\rangle$, the spin-triplet states are given by:

$$\begin{aligned} |m_s = +1\rangle &= |\alpha\alpha\rangle \\ |m_s = 0\rangle &= \frac{1}{\sqrt{2}}\left(|\alpha\beta\rangle + |\beta\alpha\rangle\right) \\ |m_s = -1\rangle &= |\beta\beta\rangle \end{aligned} \tag{5.50}$$

$$\begin{aligned} |+\rangle &= \frac{1}{\sqrt{2}}\left(|\alpha\alpha\rangle + |\beta\beta\rangle\right) \\ |-\rangle &= \frac{1}{\sqrt{2}}\left(|\alpha\alpha\rangle - |\beta\beta\rangle\right) \end{aligned} \tag{5.51}$$

We also note the transformation into the $|\pm\rangle$ basis:

$$\begin{aligned} \frac{1}{\sqrt{2}}\left(|+\rangle + |-\rangle\right) &= |+1\rangle \\ \frac{1}{\sqrt{2}}\left(|+\rangle - |-\rangle\right) &= |-1\rangle \end{aligned} \tag{5.52}$$

Singlet state The spin singlet state is given by:

$$|S = 0\rangle = \frac{1}{\sqrt{2}}\left(|\alpha\beta\rangle + |\beta\alpha\rangle\right) \tag{5.53}$$

5.6.3 Electric dipole selection rules

In Table 5.2, we present the electric dipole selection rules for a tetrahedral complex ([75]), in order to compute the transition strengths from the ground state into ${}^3T_2$ and ${}^3T_1$:

H_{ed}	$\lvert 3d_{x^2-y^2}\rangle$	$\lvert 3d_{z^2}\rangle$
$\langle \tilde{xy} \rvert$	0	$-N\sqrt{1-\alpha^2}\frac{8}{3}A\mathbf{k}$
$\langle \tilde{yz} \rvert$	$-N\sqrt{1-\alpha^2}\frac{4}{\sqrt{3}}A\mathbf{i}$	$N\sqrt{1-\alpha^2}\frac{4}{3}A\mathbf{i}$
$\langle \tilde{xz} \rvert$	$-N\sqrt{1-\alpha^2}\frac{4}{\sqrt{3}}A\mathbf{j}$	$N\sqrt{1-\alpha^2}\frac{4}{3}A\mathbf{j}$

Table 5.2: Orbital electric dipole selection rules for a tetrahedral complex $\langle \phi_f | H_{\text{ed}} | \phi_i \rangle$. Note that electric dipole transitions are only allowed between the non-bonding e ($|d_{x^2-y^2}\rangle, |d_{z^2}\rangle$) and t_2^* antibonding orbitals ($|\tilde{xy}\rangle, |\tilde{xz}\rangle, |\tilde{yz}\rangle$). For each of the tabulated values, $\{\mathbf{i},\mathbf{j},\mathbf{k}\}$ correspond to the Cartesian basis vectors in the molecular frame, N is a normalization factor, A is an overlap integral common to all transitions, and α is the covalency.

CHAPTER 6

CE^{3+} MOLECULAR SPINS

Abstract In this section, we discuss an approach to potentially reach the single spin limit by developing molecular spin complexes that emulate trivalent cerium in the solid state. The electric dipole allowed $4f^1 \rightarrow 5d^1$ transition of Ce^{3+} typically offers lifetimes on the order of tens of nanoseconds, which has permitted detection of single ions in the solid state in crystalline materials such as Yttrium Aluminum Garnet (YAG) [44] and Yttrium Orthosilicate (YSO) [77]. In addition, the crystal field surrounding the ions splits the ground and excited states in such a manner that circular polarization selection rules can spin-selectively pump population into one of the excited state spin sublevels. With sufficiently long-lived spin states, this spin-selective excitation can then be used to initialize and read out both the ground and excited state spins. Our goal in this chapter is to elucidate the constraints on the ground and excited state electronic structures in order to design functional molecular analogs of these crystalline systems. We also present time-resolved magneto-luminescence and excited state optically detected magnetic resonance results in ensembles of Ce:YAG as an example system to inform future molecular experiments. Our hope is that the fast electric dipole transition of Ce^{3+} will permit the development of optically bright complexes which can be detected down to the single molecule limit. In addition, the Ce:YAG excited state spin is optically addressable at room temperature, which may enable new applications of molecular spin systems under ambient conditions.

6.1 Electronic structure of trivalent cerium complexes

First, we describe the electronic structure of the Ce^{3+} ion in solids. Trivalent cerium in solids has a single $4f$ electron, so the total spin angular momentum $s = 1/2 \rightarrow S = 1/2$ and the total orbital angular momentum is $l = 3 \rightarrow L = 3$. Since cerium is part of the lanthanide series, this $|SL\rangle$ state splits into two J-manifolds under spin-orbit coupling: $J = 5/2$ and $J = 7/2$, with the $J = 5/2$ state lying lower in energy due to Hund's rule. The J multiplets then split into the crystal field states,

depending on the local symmetry and strength of the ligand field. However, as J is half-integral, the states remain Kramers' doublets and are therefore degenerate at $B = 0$. The $5d^1$ excited state has total spin angular momentum $s \rightarrow S = 1/2$ and total orbital angular momentum $l = 2 \rightarrow L = 2$. However, due to the $5d$ nature of this excited state, spin-orbit coupling in this excited state is weaker and the manifold's electronic structure is determined primarily by the ligand field [104].

Kramers' doublets All states will have half-integral J and therefore remain degenerate at zero field by Kramers' theorem. Given some state $|\psi\rangle$, we can find its doublet partner by applying the time-reversal operator $\hat{\Theta}$:

$$\hat{\Theta}|\psi\rangle = \exp i\pi S_y/\hbar|\psi^*\rangle \tag{6.1}$$

Ground state The ligand field splits our $J = 5/2$ multiplet into a set of Kramers' doublet eigenstates, with their compositions set by the symmetry and strength of the ligand field. An arbitrary state in this manifold $|\psi\rangle = \sum_{i=-5/2}^{+5/2} c_i|J = 5/2, M_J = i\rangle$ and its corresponding doublet partner are given by applying Equation 6.1:

$$\hat{\Theta}\begin{bmatrix} c_{5/2} \\ c_{3/2} \\ c_{1/2} \\ c_{-1/2} \\ c_{-3/2} \\ c_{-5/2} \end{bmatrix} \xrightarrow{\text{time reversal}} \begin{bmatrix} -c^*_{-5/2} \\ c^*_{-3/2} \\ -c^*_{-1/2} \\ c_{1/2} \\ -c^*_{3/2} \\ c^*_{5/2} \end{bmatrix} \tag{6.2}$$

Our main interest is the composition of the ground state doublet, as the population should relax quickly from the higher excited states (within both $J = 5/2$ and $J = 7/2$) into this pair. Ideally, to avoid thermal population of other sublevels of the $J = 5/2$ manifold, these two ground state levels will be also be energetically well-separated from the higher lying excited states. Borrowing from cerium in the solid state, we will show (via explicit computation) that a simple strategy that maximizes the spin-dependence of pumping under circularly polarized excitation is to stabi-

lize energetically isolated $M_J = \pm\frac{1}{2}$ ground and excited states, permitting σ_+ excitation to pump $|g, M_J = \frac{-1}{2}\rangle \rightarrow |e, M_J = \frac{+1}{2}\rangle$. In principle, other polarization cycles and design strategies may also be possible, but may be more challenging to realize in practice.

One chemical design strategy that can help to stabilize this ground state can be adapted from the design principles proposed by Rinehart in Reference [105] for lanthanide single molecule magnets (SMMs). Single molecule magnets aim to produce a doubly-degenerate ground state (here, guaranteed by the half-integral J) with the largest $|M_J|$ (magnetic anisotropy) possible. In addition, this ground state doublet should be energetically well-separated from any higher lying excited states to avoid thermal excitation. The key insight outlined in [105] is that the different $|\pm M_J\rangle$ states have different electron density functions. Increasing overlap between the ligands and the electron density of a particular M_J state increases the energy for that state, and reducing this overlap decreases the energy.

In our case, we aim to stabilize the smallest $|M_J|$, but are equally interested in large energetic separations. Ce^{3+} has a largely oblate electron density, so Rinehart proposed that an ideal single molecule magnet would have ligands lying primarily along the molecular quantization axis (axial "sandwich" crystal field). Therefore our prescription is opposite of that proposed by Reference [105] for single molecule magnets: designing complexes with ligands that largely lie in the xy-plane lowers the energy of $M_J = \pm\frac{1}{2}$, while increasing the energy of $M_J = \pm\frac{3}{2}$ and $\pm\frac{5}{2}$.

In addition, this design serves a second purpose: to energetically separate the $5d_{z^2}$ orbital, as it localizes the ligand electron density away from the axial d_{z^2} orbital. This energetic separation is important to minimize absorption into higher lying $5d$ excited states that is not guaranteed to be spin-selective.

Finally, careful choice of the lanthanide ion's local symmetry can be advantageous in our design. As the crystal field parameter $B_q^{(k)}$ mixes M_J states with $\Delta M_J = q$, we can eliminating mixing between certain states through careful choice of the local symmetry around the lanthanide ion. For example, avoiding trigonal $(C_3, S_6, D_3, C_{3v}, D_{3d})$ symmetries, which have $B_{\pm 3}^{(k)}$ terms, prevents mixing $\Delta M_J = \pm 3$ $(\pm 1/2 \leftrightarrow \mp 5/2, \mp 3/2 \leftrightarrow \pm 3/2)$. We also should avoid low symmetry com-

plexes (C_i,C_1), as these have $B^{(k)}_{\pm 1}$ crystal field terms can mix $\Delta M_J = \pm 1$ ($\pm 1/2 \leftrightarrow \pm 3/2$, etc.) respectively. Avoiding the trigonal or low-symmetry complexes, we can simplify our ground state Kramers' doublets according to the convention that $|g,\uparrow\rangle$ have $c_{1/2} \neq 0 \rightarrow c_{-1/2} = c_{3/2} = 0$. We can choose the phase of one of these coefficients arbitrarily, so we can assume that $c_{1/2}$ is real without loss of generality, giving the following states as our doublet:

$$|g,\uparrow\rangle = \begin{bmatrix} c_{5/2} \\ 0 \\ c_{1/2} \\ 0 \\ c_{-3/2} \\ 0 \end{bmatrix} \xrightarrow{\text{time reversal}} \begin{bmatrix} 0 \\ c^*_{-3/2} \\ 0 \\ c_{1/2} \\ 0 \\ c^*_{5/2} \end{bmatrix} = |g,\downarrow\rangle \tag{6.3}$$

Excited state Our strategy of pushing the ligands to lie primarily in the *xy* plane should push the $5d_{z^2}$ orbital to be our lowest lying $5d$ excited state. Assuming the $5d_{z^2}$ orbital is energetically well separated from the others by the ligand field, we can map this into the $|JM_J\rangle$ basis using the Clebsch-Gordan coefficients:

$$\begin{aligned} |5d_{z^2}\rangle \otimes |\uparrow\rangle &= -\sqrt{\frac{2}{5}}|J = \tfrac{3}{2}, \tfrac{1}{2}\rangle + \sqrt{\frac{3}{5}}|J = \tfrac{5}{2}, \tfrac{1}{2}\rangle = |e,\uparrow\rangle \\ |5d_{z^2}\rangle \otimes |\downarrow\rangle &= \sqrt{\frac{2}{5}}|J = \tfrac{3}{2}, \tfrac{-1}{2}\rangle + \sqrt{\frac{3}{5}}|J = \tfrac{5}{2}, \tfrac{-1}{2}\rangle = |e,\downarrow\rangle \end{aligned} \tag{6.4}$$

Ligand excited states Our final molecular design constraint is that the optical excitation should only excite into the metal center excited states, avoiding photoexcitation of the ligand. This is particularly important, as the excitation wavelength for these compounds are typically in the 350-500nm range, sufficiently high in energy to probe the excited states of many ligands. These excited states may contribute to metal centered emission, but the photoexcitation process would not have

the same circularly polarized selection rules and thus no optically-induced spin polarization will occur.

6.2 Photophysics of Ce:YAG

Optically detected magnetic resonance of Ce^{3+} in solids uses circularly polarized selection rules to achieve spin-selective pumping of the ground state. Thus, polarization in this system relies on $|\langle e,\uparrow|H_{\text{ed}}|g,\downarrow\rangle|^2 \neq |\langle e,\uparrow|H_{\text{ed}}|g,\uparrow\rangle|$ To better understand this dependence, and the requirements it imposes on the level structure for this system, we explicitly calculate the spin-dependent transition strengths here.

We start by separating the electric dipole operator into radial and angular components:

$$H_{\text{ed}} = -e\underbrace{r}_{\text{radial}}\underbrace{\mathbf{C}_q^{(1)}}_{\text{angular}} \tag{6.5}$$

The radial component is given by: $\langle 5d|r|4f\rangle$ depends on the radial charge distribution around the ion, but is the same for all transitions, and guaranteed to be non-zero due to the explicit parity change between $4f$ and $5d$ states. The angular dependence can be computed by splitting this into the $q, M_J, M_{J'}$-dependent terms and reduced matrix elements by the Wigner-Eckhart theorem:

$$\langle JM_J|\mathbf{C}_q^{(1)}|J'M_J'\rangle = (-1)^{J-M_J}\begin{pmatrix} J & 1 & J' \\ -M_J & q & M_J' \end{pmatrix}\underbrace{\langle J|\mathbf{C}^{(1)}|J'\rangle}_{\text{reduced matrix element}} \tag{6.6}$$

The reduced matrix elements $\langle J|\mathbf{C}^{(1)}|J'\rangle$ can be computed using:

$$\langle vSLJ|C^{(1)}|v'S'L'J'\rangle = \delta_{S,S'}\sqrt{(2J+1)(2J'+1)}\begin{Bmatrix} J & 1 & J' \\ L' & S & L \end{Bmatrix}\langle vL|\mathbf{C}^{(1)}|v'L'\rangle \tag{6.7}$$

where $\langle \nu L|\mathbf{C}^{(1)}|\nu' L'\rangle = \delta_{\nu,\nu'}(-1)^L\sqrt{(2L+1)(2L'+1)}\begin{pmatrix} L & 1 & L' \\ 0 & 0 & 0 \end{pmatrix}$ is the reduced matrix element for the spherical tensor operator $\mathbf{C}^{(1)}$, common to all transitions here. For this case, we have

$$\langle \nu L|\mathbf{C}^{(1`)}|\nu' L'\rangle \rightarrow \langle 5d|\mathbf{C}^{(1)}|4f\rangle = (-1)^2\sqrt{(2(2)+1)(2(3)+1)}\begin{pmatrix} 2 & 1 & 3 \\ 0 & 0 & 0 \end{pmatrix} = -\sqrt{3} \quad (6.8)$$

Since the reduced matrix element is just a constant, we see our electric dipole selection rules: $M_J + q \rightarrow M_J^{'}$ directly from the $3j$-symbol portion of Equation 6.6.

Electric dipole operator Now we just need to know what to substitute in for our electric dipole operator components $\mathbf{C}_q^{(1)}$. The electric dipole operator has some intrinsic quantization axis, which is defined by the excitation light's propagation direction $\hat{k}$, with the different components $C_q^{(1)}$ corresponding to different polarizations in this laboratory frame. However, the molecule has its own quantization axis, which is defined by the geometry of the coordinating ligands. To account for misalignment between the molecular and light quantization axes, we need to rotate our electric dipole operator into the molecular frame. This can be accomplished using an *active* rotation through three Euler angles Ω_R according to the process outlined in Reference [106]. First, we rotate the original coordinate frame around the initial z-axis by some angle α to map the original y-axis to some intermediate axis u. Next, we rotate about the intermediate axis by angle β in order to fix the new z-axis. Finally, we can rotate by third angle γ to define the rotated x- and y-axes in the rotated frame.

We can represent this rotation of a spherical tensor operator $\mathbf{A}^{(k)}$ Euler angles Ω_R mathematically using the Wigner $D-$matrices following the convention in [106]:

$$\mathbf{A}^{(k)} \overset{\text{rotation}}{\longrightarrow} \mathbf{A}_q^{(k)R} = \sum_{p=-k}^{+k} D_{p,q}^{(k)}(\Omega_R)A_p^{(k)} \quad (6.9)$$

where $D^{(k)}_{p,q}(\Omega_R)$ are the Wigner rotation matrix elements and $A^{(k)}_p$ are the components of the electric dipole operator in the original (lab) frame.

For an *active* rotation by the Euler angles $\Omega_R = \{\alpha, \beta, \gamma\}$, these are given by:

$$D^{(k)}_{pq}(\Omega_R) = \exp(-i\alpha p)\exp(-i\gamma q) d^{(k)}_{pq}(\beta) \tag{6.10}$$

where the relevant Wigner $d-$matrices are:

$$\begin{aligned} d^{(1)}_{\pm1,\pm1}(\beta) &= \cos^2\left(\frac{\beta}{2}\right) \\ d^{(1)}_{\pm1,\mp1}(\beta) &= \sin^2\left(\frac{\beta}{2}\right) \\ d^{(1)}_{0,\pm1}(\beta) &= d^{(1)}_{\mp1,0} = \frac{\pm1}{\sqrt{2}}\sin(\beta) \\ d^{(1)}_{0,0}(\beta) &= \cos(\beta) \end{aligned} \tag{6.11}$$

Therefore, for a given polarization in the lab frame, we have the electric dipole operator, rotated into in the molecular frame:

$$\begin{aligned} \sigma_{+,\text{lab}} &: \sin^2(\frac{\beta}{2})\exp(i(\alpha-\gamma))C^{(1)}_{-1} + \tfrac{1}{\sqrt{2}}\exp(-i\gamma)\sin(\beta)C^{(1)}_0 + \cos^2(\frac{\beta}{2})\exp(-i(\alpha+\gamma))C^{(1)}_{+1} \\ \pi_{\text{lab}} &: \frac{1}{\sqrt{2}}\sin(\beta)\exp(i\alpha)C^{(1)}_{-1} + \cos(\beta)C^{(1)}_0 - \tfrac{1}{\sqrt{2}}\sin(\beta)\exp(-i\alpha)C^{(1)}_{-1} \\ \sigma_{-,\text{lab}} &: \cos^2(\frac{\beta}{2})\exp(i(\alpha-\gamma))C^{(1)}_{-1} - \tfrac{1}{\sqrt{2}}\exp(i\gamma)\sin(\beta)C^{(1)}_0 + \sin^2(\frac{\beta}{2})\exp(-i(\alpha-\gamma))C^{(1)}_{+1} \end{aligned} \tag{6.12}$$

Importantly, since the initial rotation by α about the original z-axis does not change our polarization convention, and the z-axis is fixed following the rotation around the intermediate axis by β, our final expression should only incorporate β, but not α or γ. This falls out of the expression as we could arbitrarily choose $\alpha = 0$ (which would not altering our definition of circular polarization), causing an $\exp(-i\alpha)$ factor to become common to all terms.

Spin polarization of both the ground and excited states requires spin-selective pumping. Defining $g_+ = |\langle e,\uparrow |H_{\text{ed}}|g,\downarrow\rangle|$, $g_- = |\langle e,\downarrow |H_{\text{ed}}|g,\uparrow\rangle|$, and $g_0 = |\langle e,\uparrow(\downarrow)|H_{\text{ed}}|g,\uparrow(\downarrow)\rangle|$, we can characterize the spin-selectivity of the optical interface according to:

$$\begin{aligned}\eta \sim & \frac{\left(|\langle e,\uparrow |H_{\text{ed}}|g,\downarrow\rangle|^2 + |\langle e,\uparrow |H_{\text{ed}}|g,\uparrow\rangle|^2\right) - \left(|\langle e,\downarrow |H_{\text{ed}}|g,\downarrow\rangle|^2 + |\langle e,\downarrow |H_{\text{ed}}|g,\uparrow\rangle|^2\right)}{|\langle e,\uparrow |H_{\text{ed}}|g,\downarrow\rangle|^2 + |\langle e,\uparrow |H_{\text{ed}}|g,\uparrow\rangle|^2 + |\langle e,\downarrow |H_{\text{ed}}|g,\downarrow\rangle|^2 + |\langle e,\downarrow |H_{\text{ed}}|g,\uparrow\rangle|^2} \\ & \rightarrow \frac{g_+ - g_-}{g_+ + g_- + 2g_0}\end{aligned} \tag{6.13}$$

where the first two terms in the numerator account for pumping into $|e,\uparrow\rangle$, the second two terms account for pumping into $|e,\downarrow\rangle$ and the denominator normalizes by the total pump rate.

Assuming the excited state doublet is rigorously $|5d_{z^2},\uparrow(\downarrow)\rangle$, we can substitute in the electric dipole operator for $\sigma_{+,\text{lab}}$ and determine the spin-dependent pump strength in terms of the ground state composition. This is done using a computer algebra system (which I have shared at [107]) but the full expression is too complex to present here. Instead, we present two limiting cases that are instructive. In the case where the molecule and the lab frame are aligned, this reduces down to a straightforward expression which is determined by the ground state composition:

$$\eta(\beta \rightarrow 0) \sim \frac{128c_{1/2}^2 - 1296|c_{-3/2}|^2}{128c_{1/2}^2 + 1296|c_{-3/2}|^2} \tag{6.14}$$

The lack of inclusion of any $c_{5/2}$ terms matches with the selection rule on the electric dipole operator enforces that $|g,M_J\rangle \rightarrow |e,M_J+q\rangle$, as the excited state consists only of $|M_J = \pm\frac{1}{2}\rangle$. These terms will decrease the overall transition strength but not alter the spin-selectivity. Based on this form, our goal should be to stabilize $M_J = \pm\frac{1}{2}$ as our Kramers' doublet ground state, and avoid mixing in $M_J = \pm\frac{3}{2}$ (which decreases the selectivity) and $M_J = \pm\frac{5}{2}$ (which does not contribute to the transition strength).

In the case that the doublet has no $M_J = \pm 3/2$ composition, we can obtain a simple dependence on the spin-selectivity versus the angle between the molecular quantization axis and the lab frame:

$$\eta(c_{-3/2} \to 0) = \frac{-128\cos(\beta)}{306\cos(2\beta) - 434} \tag{6.15}$$

6.3 Optical spin polarization

Now that we have determined the dependence of the spin-dependent pump rates on the ground state composition and misalignment of the molecular and lab frames, we can develop a rate equation model of ground and excited state spin polarizations. Denoting $n_{g,\uparrow(\downarrow)}$ as the ground state population for $\uparrow$ ($\downarrow$) and $n_{e,\uparrow(\downarrow)}$ as the $5d$ excited state population for $\uparrow$ ($\downarrow$), we can model the system using the following set of coupled rate equations:

$$\begin{aligned}
\dot{n_{e,\uparrow}} &= g_+ n_{g,\downarrow} + g_0 n_{g,\uparrow} \quad - \left(\gamma_{\text{opt,SC}} + \gamma_{\text{opt,SF}}\right) n_{e,\uparrow} - \gamma_{T_1,e}\left(n_{e,\uparrow} - n_{e,\downarrow}\right) \\
\dot{n_{e,\downarrow}} &= g_- n_{g,\uparrow} + g_0 n_{g,\downarrow} \quad - \left(\gamma_{\text{opt,SC}} + \gamma_{\text{opt,SF}}\right) n_{e,\downarrow} - \gamma_{T_1,e}\left(n_{e,\downarrow} - n_{e,\uparrow}\right) \\
\dot{n_{g,\uparrow}} &= -\left(g_- + g_0\right) n_{g,\uparrow} \quad + \gamma_{\text{opt,SC}} n_{e,\uparrow} + \gamma_{\text{opt,SF}} n_{e,\downarrow} - \gamma_{T_1,g}\left(n_{g,\uparrow} - n_{g,\downarrow}\right) \\
\dot{n_{g,\downarrow}} &= \underbrace{-\left(g_+ + g_0\right) n_{g,\downarrow}}_{\text{pumping}} \quad \underbrace{+\gamma_{\text{opt,SC}} n_{e,\uparrow} + \gamma_{\text{opt,SF}} n_{e,\downarrow}}_{\text{PL / internal conversion}} \underbrace{- \gamma_{T_1,g}\left(n_{g,\downarrow} - n_{g,\uparrow}\right)}_{\text{spin-lattice relaxation}}
\end{aligned} \tag{6.16}$$

where $\gamma_{T_1,e(g)}$ is the excited (ground) state spin-lattice relaxation rate, $\gamma_{\text{opt,SF(SC)}}$ are the spin-conserving (spin-flip) optical decay rates, state population for $\uparrow$ ($\downarrow$), $g_\pm$ are the spin-flip pump rates, and g_0 is the spin-conserving pump rate. This process is depicted schematically in Figure 6.1.

We define the ground state spin polarization as:

$$P_g = \frac{n_{g,\uparrow} - n_{g,\downarrow}}{n_{g,\uparrow} + n_{g,\downarrow}} \tag{6.17}$$

and the excited state spin polarization as:

$$P_e = \frac{n_{e,\uparrow} - n_{e\downarrow}}{n_{e,\uparrow} + n_{e,\downarrow}} \tag{6.18}$$

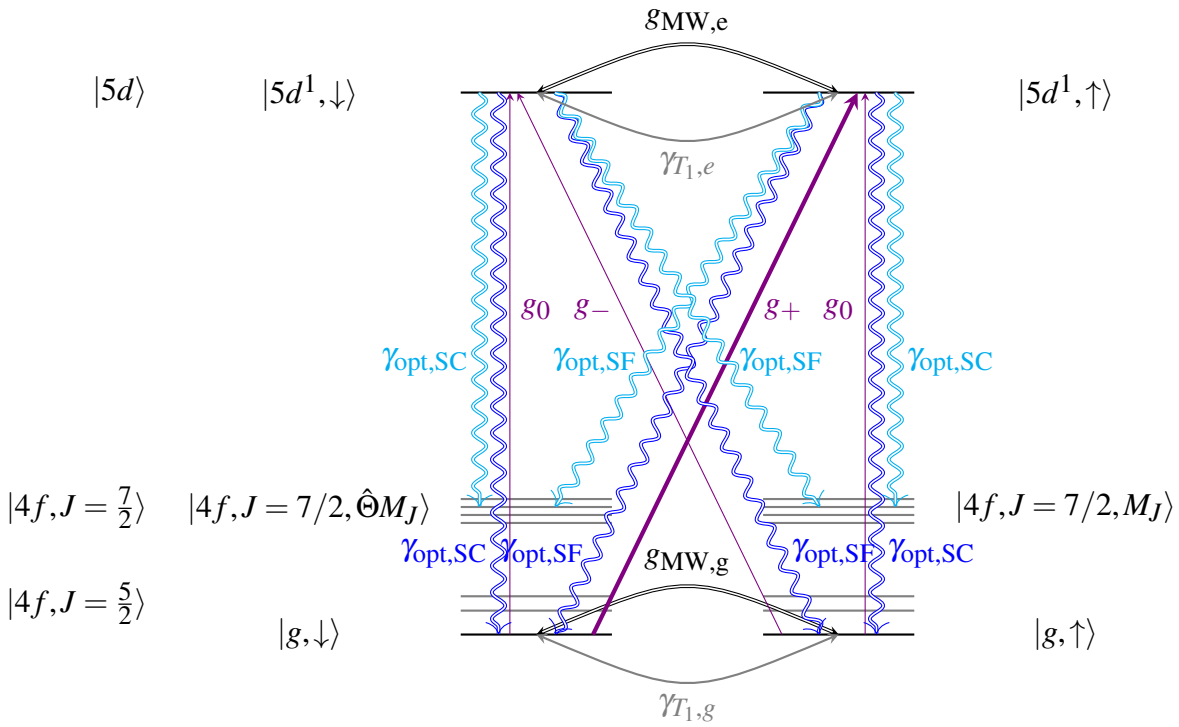

Figure 6.1. Photophysics of Ce^{3+}. Off-resonant excitation with circularly polarized light drives a spin-flip electric dipole transition at rate g_+. Imperfections in the polarization, or misalignment between the molecular and lab frame induces additional transitions at rate g_- and g_0. Population can decay out of the excited state radiatively through a spin flip process ($\gamma_{\mathrm{opt,SF}}$) or through a spin-conserving process ($\gamma_{\mathrm{opt,SC}}$, includes internal conversion). Spin-lattice relaxation mixes the populations of the spin sublevels in both the ground and excited states at respective rates $\gamma_{T_1,g}$ and $\gamma_{T_1,e}$ respectively. The relatively small spacing between the lowest two sublevels implies that $\gamma_{T_1,g}$ is fast, except for at low temperatures. Microwave transitions of both the ground and excited state can be driven coherently at $g_{\mathrm{MW,g}}$ and $g_{\mathrm{MW,e}}$ respectively.

Solving for the steady state solution by setting $\dot{n}_i = 0$ subject to the constraint $\sum_i n_i = 1$, and substituting in the $\bar{n}_i$, we can get the steady state spin-polarization:

$$\begin{aligned}
\overline{P_g} = & \frac{(g_+ - g_-)(\gamma_{\text{opt,SC}} + \gamma_{\text{SL,e}})}{(\gamma_{\text{opt,SC}} + \gamma_{\text{SL,e}})(g_+ + g_-) + 2g_0(\gamma_{\text{opt,SF}} + \gamma_{\text{SL,e}}) + 2(\gamma_{\text{opt}} + 2\gamma_{\text{SL,e}})\gamma_{\text{SL,g}}} \\
\overline{P_e} = & \frac{(g_+ - g_-)(g_0 + \gamma_{\text{SL,g}})(\gamma_{\text{opt,SC}} + \gamma_{\text{opt,SF}})}{2g_- g_+ (\gamma_{\text{opt,SC}} + \gamma_{\text{SL,e}}) + 2g_0^2(\gamma_{\text{opt,SF}} + \gamma_{\text{SL,e}}) + (g_+ + g_-)(\gamma_{\text{opt,SC}} + \gamma_{\text{opt,SF}} + 2\gamma_{\text{SL,e}})\gamma_{\text{SL,g}} + g_0(\gamma_{\text{opt,SC}} + \gamma_{\text{opt,SF}} + 2\gamma_{\text{SL,e}})(g_- + g_+ + 2\gamma_{\text{SL,g}})}
\end{aligned} \tag{6.19}$$

In the high temperature limit ($\gamma_{\text{SL,g}} \to \infty$), even though the ground state spin polarization $\overline{P_g} \to 0$, we can still achieve a steady-state excited state spin polarization, given by:

$$\overline{P_e} = \frac{g_+ - g_-}{g_+ + g_- + 2g_0}\left(\frac{\gamma_{\text{opt}}}{\gamma_{\text{opt}} + 2\gamma_{\text{SL,e}}}\right) = \eta\left(\frac{\gamma_{\text{opt}}}{\gamma_{\text{opt}} + 2\gamma_{\text{SL,e}}}\right) \tag{6.20}$$

6.3.1 Optical contrast

The total luminescence is given by the sum of the radiative decays out of the excited states, which can be distinguished by the polarization and the emission wavelength:

$$\begin{aligned}
\text{PL} = & n_{e,\downarrow}\left(\sum_i \left[|\langle 4f, J=7/2, i|\sigma_{+,\text{lab}}|e,\downarrow\rangle|^2 + |\langle 4f, J=7/2, i|\sigma_{-,\text{lab}}|e,\downarrow\rangle|^2\right]\right. \\
& \left. + \sum_j \left[|\langle 4f, J=5/2, j|\sigma_{+,\text{lab}}|e,\downarrow\rangle|^2 + |\langle 4f, J=5/2, j|\sigma_{-,\text{lab}}|e,\downarrow\rangle|^2\right]\right) \\
& + n_{e,\uparrow}\left(\sum_i \left[|\langle 4f, J=7/2, i|\sigma_{+,\text{lab}}|e,\uparrow\rangle|^2 + |\langle 4f, J=7/2, i|\sigma_{-,\text{lab}}|e,\uparrow\rangle|^2\right]\right. \\
& \left. \sum_j \left[|\langle 4f, J=5/2, j|\sigma_{+,\text{lab}}|e,\uparrow\rangle|^2 + |\langle 4f, J=5/2, j|\sigma_{-,\text{lab}}|e,\uparrow\rangle|^2\right]\right)
\end{aligned} \tag{6.21}$$

Each of these summations are just constants, which depend on the composition of the different ground state crystal field multiplets. In addition, they are related due to symmetry considerations:

- $\gamma_{\text{rad,SF,7/2}} = \sum_i |\langle 4f, J=7/2, i|\sigma_{\pm,\text{lab}}|e,\uparrow\rangle|^2 = \sum_i |\langle 4f, J=7/2, i|\sigma_{\mp,\text{lab}}|e,\downarrow\rangle|^2$ and $\gamma_{\text{rad,SC,7/2}} = \sum_i |\langle 4f, J=7/2, i|\sigma_{\mp,\text{lab}}|e,\uparrow\rangle|^2 = \sum_i |\langle 4f, J=7/2, i|\sigma_{\pm,\text{lab}}|e,\downarrow\rangle|^2$

- $\gamma_{\text{rad,SF,5/2}} = \sum_i |\langle 4f, J=5/2, i|\sigma_{\pm,\text{lab}}|e,\uparrow\rangle|^2 = \sum_i |\langle 4f, J=5/2, i|\sigma_{\mp,\text{lab}}|e,\downarrow\rangle|^2$ and $\gamma_{\text{rad,SC,5/2}} = \sum_i |\langle 4f, J=5/2, i|\sigma_{\mp,\text{lab}}|e,\uparrow\rangle|^2 = \sum_i |\langle 4f, J=5/2, i|\sigma_{\pm,\text{lab}}|e,\downarrow\rangle|^2$

For some configuration of the collection wavelength ($J = 5/2$ vs. $J = 7/2$, or both) or collected polarization ($\sigma_{\pm,\text{lab}}$ or both), we can calculate the luminescence from the excited state population and these constants.

For our experimental configuration, we separate $\sigma_{+,\text{lab}}$and $\sigma_{-,\text{lab}}$into two separate channels to yield:

$$\begin{aligned}
\text{PL}_+ &= n_{e,\downarrow} \sum_j |\langle 4f, J=5/2, j|\sigma_{+,\text{lab}}|e,\downarrow\rangle|^2 + n_{e,\uparrow} \sum_j |\langle 4f, J=5/2, j|\sigma_{+,\text{lab}}|e,\uparrow\rangle|^2 \\
&= n_{e,\downarrow}\gamma_{\text{rad,SC,5/2}} + n_{e,\uparrow}\gamma_{\text{rad,SF,5/2}} \\
\text{PL}_- &= n_{e,\downarrow} \sum_j |\langle 4f, J=5/2, j|\sigma_{-,\text{lab}}|e,\downarrow\rangle|^2 + n_{e,\uparrow} \sum_j |\langle 4f, J=5/2, j|\sigma_{-,\text{lab}}|e,\uparrow\rangle|^2 \\
&= n_{e,\downarrow}\gamma_{\text{rad,SF,5/2}} + n_{e,\uparrow}\gamma_{\text{rad,SC,5/2}}
\end{aligned} \tag{6.22}$$

Therefore the spin-dependent contrast is given by:

$$\begin{aligned}
C &\sim \frac{\text{PL}(n_{e,\uparrow}) - \text{PL}(n_{e,\downarrow})}{\text{PL}(n_{e,\uparrow}) + \text{PL}(n_{e,\downarrow})} \\
C_+ &= \frac{n_{e,\uparrow}\gamma_{\text{rad,SF,5/2}} - n_{e,\downarrow}\gamma_{\text{rad,SC,5/2}}}{n_{e,\downarrow}\gamma_{\text{rad,SC,5/2}} + n_{e,\uparrow}\gamma_{\text{rad,SF,5/2}}} \\
C_- &= \frac{n_{e,\uparrow}\gamma_{\text{rad,SC,5/2}} - n_{e,\downarrow}\gamma_{\text{rad,SF,5/2}}}{n_{e,\downarrow}\gamma_{\text{rad,SF,5/2}} + n_{e,\uparrow}\gamma_{\text{rad,SC,5/2}}}
\end{aligned} \tag{6.23}$$

6.3.2 Magnetic field dependence

By Kramers' theorem, both the ground and excited state doublets are degenerate under zero magnetic field. Applying a magnetic field breaks the degeneracy due to the Zeeman effect, and we apply degenerate perturbation theory to understand the impact on the ground and excited states here. This amounts to constructing and finding the eigenvalues of the matrix:

$$\langle k^{(0)}|V_{\text{Zeeman}}|k^{(0)}\rangle \tag{6.24}$$

where $|k^{(0)}\rangle$ are the Kramers' doublet states. The eigenvalues give the Zeeman splitting, and the eigenvectors yield the coefficients of the original doublet basis vectors $|\uparrow\rangle$ and $|\downarrow\rangle$.

Ground state The Zeeman interaction is given in the spherical basis as:

$$\begin{aligned}\langle vSLJM_J|H_{\text{Zeeman}}|v'S'L'J'M'_J\rangle =& \langle vSLJ|L+g_eS|v'S'L'J'\rangle \\ & \sum_{q=-1}^{+1}(-1)^q B_q^1 \begin{pmatrix} J & 1 & J' \\ -M_J & -q & M'_J \end{pmatrix}\end{aligned} \tag{6.25}$$

where g_J is the Lande g-factor and $B_{+1}^{(1)} = -\frac{1}{\sqrt{2}}\left(B_x + iB_y\right)$, $B_{-1}^{(1)} = \frac{1}{\sqrt{2}}\left(B_x - iB_y\right)$ and $B_0^{(1)} = B_z$ relate the Cartesian and spherical bases. The reduced matrix element $\langle vSLJ|L+gS|v'S'L'J'\rangle$ is given by Equation 2.22:

$$\begin{aligned}\langle vSLJ|L+gS|v'S'L'J\rangle &= \delta_{v,v'}\delta_{L,L'}\delta_{S,S'}g\sqrt{J(J+1)(2J+1)} && (J=J') \\ \langle vSLJ|L+gS|v'S'L'(J-1)\rangle &= \delta_{v,v'}\delta_{L,L'}\delta_{S,S'}(g-1)\sqrt{\tfrac{(S+L+J+1)(J+L-S)(J+S-L)(S+L-J+1)}{4J}} && (J'=J-1)\end{aligned} \tag{6.26}$$

where the $J=J'$ case accounts for the interaction between states belonging to the same J-multiplet and the $J'=J-1$ case accounts for the interaction between J-multiplets subject to magnetic dipole selection rules (which mixes the states).

The ground state g-factors depend on the composition of the lowest Kramers' doublets in terms of the $|J,M_J\rangle$ states. We plot the computed $g-$factors as a function of the ground state composition in Figure 6.2. The g_{zz} component is directly aligned to the molecular frame and can be measured directly through ODMR, as it does not induce mixing between the Kramers' doublet states. As applying an off-axis field mixes the Kramers' doublet states (and eliminates any spin-dependent pumping), the transverse g-factors may be more challenging to measure directly through ODMR (requiring a larger, axial field, with a small off-axis field).

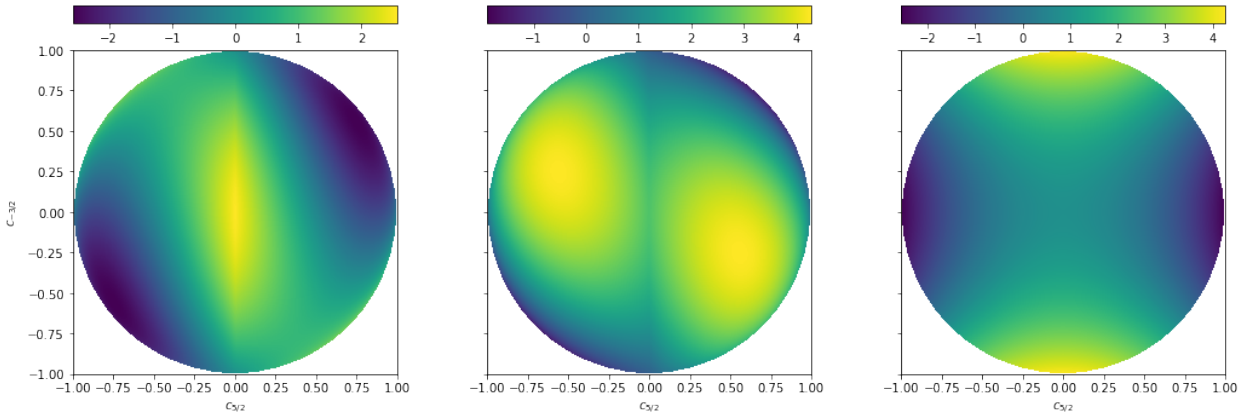

Figure 6.2. Computed ground state g-factors for Ce^{3+} compounds. Comparison of experimental and computed values allows some determination of the composition of the ground state doublet. Calculations do not account for any mixing with the $J = 7/2$ manifold, which likely is admixed with the ground state to ~ 0.1 [108]

Excited state For the $5d$ excited state, we work in the $|LS\rangle$-basis, where the Zeeman interaction separates into orbital and spin terms and is given by Equation 2.19 and Equation 2.20 respectively.

$$\begin{aligned}\langle \nu SLM_S M_L|H_{\text{Zeeman}}|\nu' S' L' M_S' M_L'\rangle &= \langle \nu SLM_S M_L|L + g_e S|\nu' S' L' M_S M_L\rangle \\ &= \delta_{S,S'}\delta_{M_S,M_S'}\langle \nu SLM_L|L|\nu' L' M_L\rangle \\ &+ g_e \delta_{L,L'}\delta_{M_L,M_L'}\langle \nu SM_S|S|\nu' SM_S\rangle\end{aligned} \tag{6.27}$$

For the orbital part, $|d_{z^2}\rangle \leftrightarrow M_L = 0$ and the three-J symbol in the Hamiltonian is zero for all values of q. Therefore the orbital part does not contribute to the Zeeman interaction. The second part is equivalent to the Hamiltonian for a free electron. Therefore the excited state g-factor is approximately isotropic and equal to the electron g-factor $g_e \approx 2.0023$. Deviations from this value, and any observed anisotropy result from mixing with other orbitals with $M_L \neq 0$.

6.3.3 Excited state optically-detected magnetic resonance

For experimental purposes, we consider two limiting cases are useful for our analysis: the case of aligned ($\mathbf{B} \parallel \hat{z}$) and the perpendicular cases ($\mathbf{B} \perp \hat{z}$) where $\hat{z}$ denotes the molecular quantization axis. In the aligned case, our eigenbasis remains the same, with no mixing between the nominal

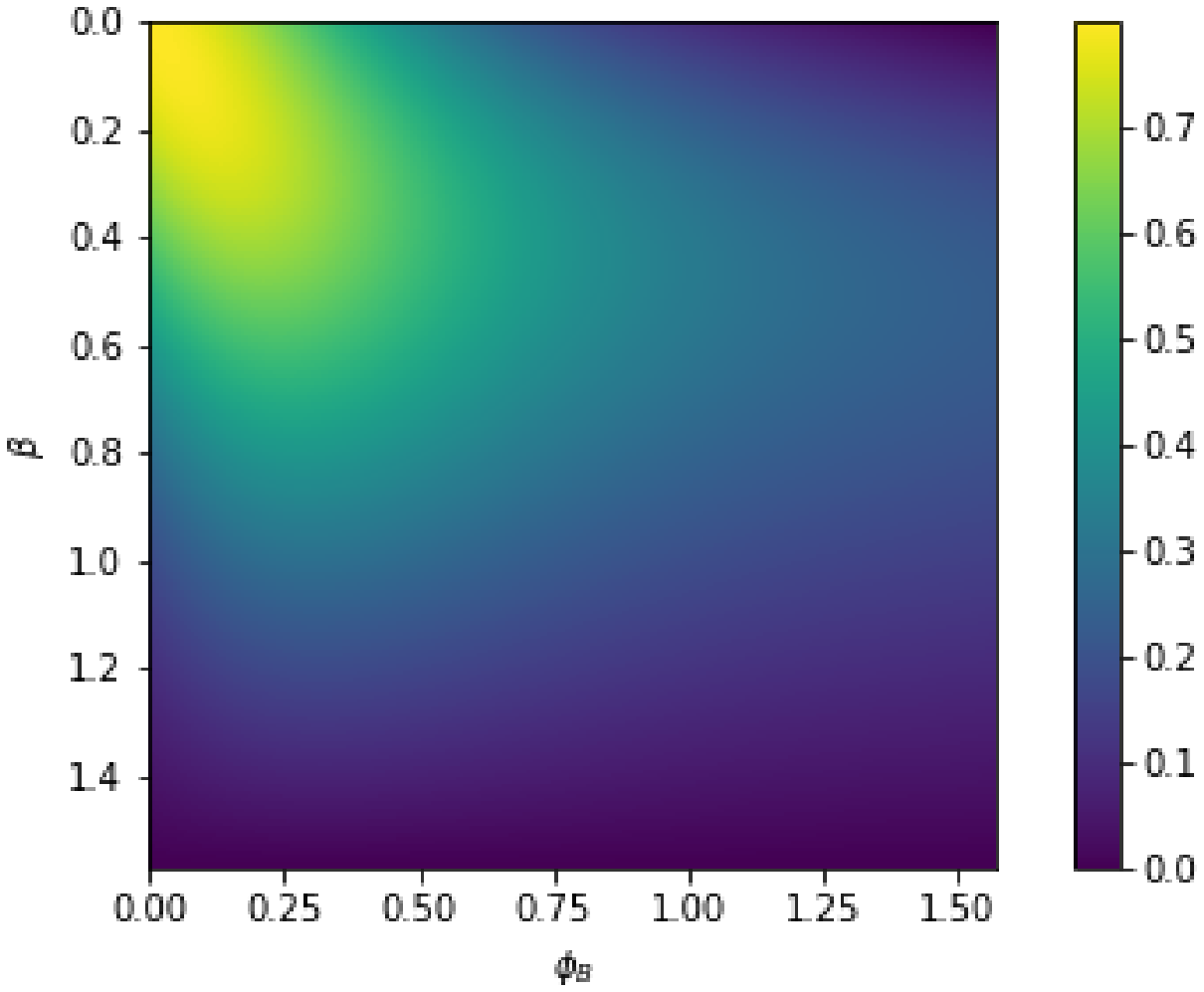

Figure 6.3. Dependence of spin-dependent pumping on relative orientation between the molecular quantization axis and the magnetic field axis.

$|\uparrow\rangle$ and $|\downarrow\rangle$ states. In the case that the magnetic field is perpendicularly aligned to the quantization axis, the eigenbasis should become an equal superposition of $|\uparrow\rangle$ and $|\downarrow\rangle$:

$$\psi_{\pm} = \frac{1}{\sqrt{2}}(|\uparrow\rangle \pm |\downarrow\rangle) \tag{6.28}$$

Note that this analysis applies to the mixing of both the ground and excited states. Additionally, the mixing of these states by an off-axis field implies that spin-dependent pumping under circularly polarized excitation is completely suppressed for $\mathbf{B} \perp \hat{z}$.

Finally, we can also construct the g-tensor following the procedure in [109]. The principal values of the tensor are the g-factors, which can be measured directly via conventional ESR.

For the excited state, if only the $|d_{z^2}\rangle$ orbital is occupied directly, the orbital component does not contribute to the Zeeman splitting ($M_L = 0$) and the system appears just as a free electron spin. Therefore we would expect an excited state g-factor of approximately $g_e \sim 2$. In addition, measurement of the excited state g-factor provides a way to determine the mixing of other orbital states, as these would result in deviations away from the free electron value.

6.4 Experimental results - Ce:YAG

In this section, we present optically detected magnetic resonance and polarization-resolved lifetime measurements of Ce:YAG as a proof-of-concept demonstration of these principles. We expect that similar measurements could be performed on a suitable Ce^{3+} molecular system through small adaptations of the experimental protocol and apparatus.

6.4.1 Experimental setup

Our experimental setup is comprised of a laser scanning confocal microscope with polarization-resolved detection. For experimental flexibility, the setup (with the exception of the imaging optics) is built into cage optics. A more detailed description of the experimental apparatus is provided in Appendix A. All measurements were performed under ambient conditions.

6.4.2 Polarization resolved lifetime

We start by presenting polarization-resolved lifetime measurements of [111]-oriented Ce:YAG under different magnetic field conditions. In general, the six sites that the cerium ion can occupy in the YAG lattice are magnetically inequivalent, but they are magnetically equivalent along the [111] direction. Each measurement is performed by applying a short (~ 1ns) circularly polarized laser

pulse to pump the Ce^{3+} ion into the excited state. When reasonably well-aligned to the molecular frame, σ_+ excitation pumps population from $|g,\downarrow\rangle \rightarrow |e,\uparrow\rangle$ at a rate g_+ as depicted in Figure 6.1.

Once population is pumped into the excited state there are several processes that can occur:

1. Population is equilibrated by spin-lattice relaxation (T_1). If population is initialized into $|e,\uparrow\rangle$, this strictly results in a net population transfer from $|e,\uparrow\rangle \rightarrow |e,\downarrow\rangle$.

2. Population decays into the ground state through spin-conserving processes (radiative or non-radiative).

3. Population decays to the ground state through a spin-flip radiative process. Importantly, this spin-flip process is polarization-dependent depending on the initial state (i.e. σ_+ is emitted for $|e,\downarrow\rangle \rightarrow |e,\uparrow\rangle$ and σ_- for $|e,\uparrow\rangle \rightarrow |e,\downarrow\rangle$).

4. A resonant microwave field coherently drive transitions between $|e,\uparrow\rangle \leftrightarrow |e,\downarrow\rangle$ at a rate $g_{\mathrm{MW},e}$.

For the polarization-resolved lifetime measurements, we don't apply a microwave drive, so we neglect the last process here. As process (3) is spin-dependent, we can monitor the excited state spin-polarization by performing polarization-resolved luminescence measurements. These measurements are presented in Figure 6.4. Crucially, the results depend on the strength and orientation of an applied magnetic field.

Figure 6.4 shows the result of these measurements under different magnetic field conditions. For the $\mathbf{B} \parallel \hat{k}$ case, the magnetic field is aligned to the light quantization axis. If the Ce ion frame is reasonably well aligned to the lab frame, the ground and excited state eigenstates are approximately $|\uparrow\rangle$ and $|\downarrow\rangle$. σ_+ excitation then initializes into $|\uparrow\rangle_e$. In contrast $|e,\downarrow\rangle$ is only populated by spin-lattice relaxation from $|e,\uparrow\rangle$, which acts in an attempt to equilibriate the populations of the excited state spins. After the initial polarizing pulse, we see more σ_- emission, but an additional decay channel which reduces the excited state lifetime is present for one of the collected polarizations, as shown in Figure 6.4A. Although we cannot ascertain the nature of this channel directly from our

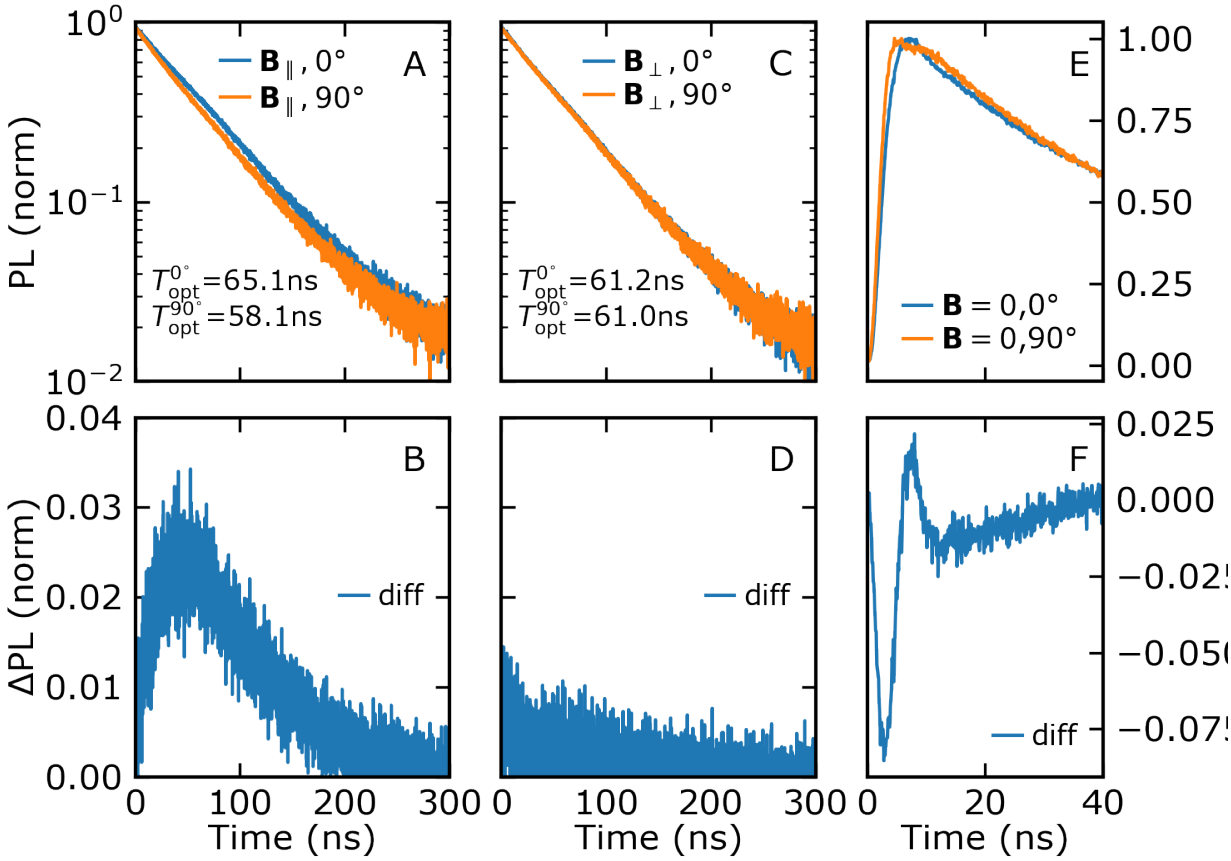

Figure 6.4. Polarization-resolved lifetime measurements of Ce:YAG under different magnetic field conditions. σ_+ polarization spin-selectively pumps $|g,\downarrow\rangle \rightarrow |e,\uparrow\rangle$. The 0° and 90° traces correspond to the two orthogonal collected polarizations. (A) A large magnetic field aligned to the light quantization axis yields two distinct lifetimes depending on the collected light polarization (~65ns for 0°, ~58ns for 90°), which is apparent in the differential signal (B). (C) $\mathbf{B} \perp \hat{k}$ rapidly mixes $|e,\uparrow\rangle \leftrightarrow |e,\downarrow\rangle$, yielding the same intermediate lifetime of ~62ns for both collected polarizations. No differential signal is observed, as shown in (D). (E) At zero field, the magnetic field produced by the YAG nuclear spin bath introduces coherent oscillations, which is also evident in the differential trace (F). Each of these results is good agreement with data presented in [104] on single centers.

experiment, this could result from spin-lattice relaxation, or an enhanced radiative or non-radiative decay channel.

For the $\mathbf{B} \perp \hat{k}$ case, the magnetic field mixes the Kramers' doublets, with the result that the eigenstates then become $\frac{1}{\sqrt{2}}(|\uparrow\rangle \pm |\downarrow\rangle)$ for a perpendicular field. The net result of this mixing is that both polarization channels exhibit nearly identical lifetimes as shown in Figure 6.4B. Finally, the $B = 0$ case allows some spin polarization, and we resolve some oscillatory behavior due to hyperfine interaction between the spin and lattice ^{27}Al ($I = 5/2$) nuclei.

6.4.3 Excited state ODMR

Finally, we can introduce a radio frequency (RF) drive field to perform excited state optically detected magnetic resonance measurements. Applying a fairly large magnetic field aligned to the light quantization axis introduces a Zeeman splitting between $|e,\uparrow\rangle$ and $|e,\downarrow\rangle$. When the RF drive frequency matches the Zeeman splitting energy, population can be driven between $|e,\uparrow\rangle \leftrightarrow |e,\downarrow\rangle$, leading to a change in optical emission signal. Notably, the sign and magnitude of this signal changes according to the polarization of light collected, and whether emission into the $J = 5/2$ or $J = 7/2$ manifold is selected through spectral filtering.

6.5 Conclusion and Outlook

Future efforts in this area will extend our demonstration of optically-detected magnetic resonance of Ce^{3+} to molecular systems and push down to the single molecule limit. Several outstanding challenges remain to reach this goal. First, and most crucially, identification and chemical synthesis of molecular systems that are direct photophysical analogs of Ce^{3+} in the solid state is necessary. These experiments require radiatively efficient compounds, where absorption and emission primarily involve the metal center. The coordinating ligands must be carefully chosen to avoid antenna effects or metal-ligand charge transfer processes, as these will relax circular polarization selection rules away from the metal-centered processes described in this chapter. This is especially

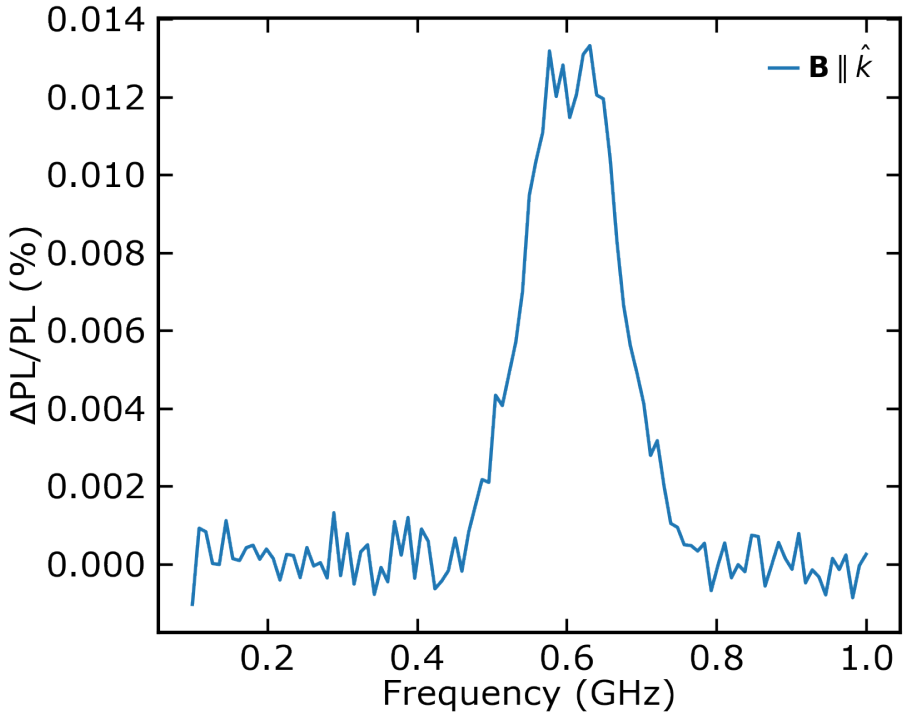

Figure 6.5. Excited state optically detected magnetic resonance of [111]-oriented Ce:YAG under ambient conditions. Applying $\mathbf{B} \parallel \hat{k}$ splits the excited state Kramers' doublet into $|e,\uparrow\rangle$ and $|e,\downarrow\rangle$ through the Zeeman interaction. For the sample Ce^{3+} ions are magnetically-equivalent, so only a single, broad peak is observed. Pumping with σ_+ light drives the spin-flip transition $|g,\downarrow\rangle \rightarrow |e,\uparrow\rangle$. When the microwave drive is on resonance with the Zeeman energy, transitions are driven between $|e,\uparrow\rangle \leftrightarrow |e,\downarrow\rangle$. Large drive fields are necessary to sufficiently rotate the spin during the short excited state spin-lattice relaxation time $T_{1,e}$.

important given the near-UV excitation energies used, which can be sufficiently high energy to interact with ligand excited states.

One initial compound (described in Reference [110]) we studied appears to have significant involvement of the ligand in the photoexcitation process, which we suspect has prevented observation of optically-detected magnetic resonance. However, strategies to synthesize radiatively efficient Ce^{3+} compounds have been demonstrated in the literature [111,112], and it appears that several of these compounds may have the correct geometry to stabilize a predominately $M_J = \pm\frac{1}{2}$ $4f$ ground state and isolated $5d_{z^2}$ excited state. We plan to co-crystallize these compounds with their Ln-based diamagnetic analogs to reduce the dipolar coupling between nearby molecules and produce dilute crystals that may be a close analog of the Ce-doped oxides.

Single molecule experiments Reaching the single molecule limit also introduces several important practical experimental challenges. The first is reduction of background fluorescence due to impurities in the organic solvents used during chemical synthesis. Residual solvent impurities are known to be a problem in analytical chemistry, and our experimental apparatus should be similarly sensitive due to the low photonic limit of detection. When pushing towards the single molecule limit (where overall sample brightness becomes low), it may become important to reduce the background emission of any luminescent impurities in the chemical solvents used in sample preparation. In addition, this impurity background can introduce ambiguity into the interpretation of experimental results, as these impurities may introduce additional decay terms into lifetime measurements (which may account for biexponential behavior, rather than the Ce).

Second, the relatively low contrast observed in our experiments on YAG will pose a challenge for ODMR signal detection. The time-averaged signal-to-noise ratio is given by [113]:

$$\langle SNR \rangle = \sqrt{\alpha_0}\frac{C}{\sqrt{2-C}}\sqrt{N} \underset{C<<1}{\longrightarrow} C\sqrt{\frac{\alpha_0}{2}}\sqrt{N} \tag{6.29}$$

where α_0 is the average number of detected photons, C is the spin-dependent contrast, and N is the number of experiment repetitions. The experimental contrast is set by the spin-dependent

pumping η defined in Equation 6.13, as well as the proportion of the spin ensemble driven by the microwave pulse (which depends on the spin linewidth $\sim 1/T_2^*$ and the Rabi frequency Ω_R). Shortened spin-lattice relaxation times may broaden transitions further, reducing optical contrast. In YAG, the linewidth is quite broad due to the short spin-lattice relaxation time. We expect similar or increased broadening in molecular systems due to shorter spin-lattice relaxation times or interaction with other nearby spins.

Ground state experiments Finally, optically detected magnetic resonance experiments on the ground state spin may be useful for enabling applications in molecular quantum science. In addition, optical readout of a single ground state molecular spin would be an important technological milestone. These experiments will likely require low temperatures, given the already short ground state spin-lattice relaxation time $T_{1,g}$ of trivalent cerium in comparably more rigid solid-state materials. Pulsed ESR experiments can elucidate the temperature-dependence of the ground state spin lifetime and identify the temperatures required for feasible operation. In addition, it is important to disentangle magnetic resonance of the ground state versus the excited state. One scheme to accomplish this could follow a pulsed excitation scheme (see Reference [44]), where (1) a laser pulse initializes the spin (2) a wait time allows the spin to decay into the ground state (3) microwave manipulation drives the spin and (4) emission is detected following a final readout pulse.

CHAPTER 7

CONCLUSIONS AND FUTURE WORK

Here, I offer a short recap of the content of this thesis and a brief discussion of future research avenues in this area. I opened Chapter 1 with an broader introduction to quantum technologies, with a focus on spin qubits. In Chapter 2, I presented an outline of crystal and ligand field theory as a framework to understand the electronic structure of molecular complexes of transition metals and rare earth ions. In Chapter 3, I discussed photophysics and spin dynamics, and how consideration of these areas in tandem allows us to develop optical readout schemes for molecular spins. Following these introductory chapters, the remainder of the thesis was focused towards implementation of various strategies to optically readout molecular spins. In Chapter 4, I presented a frequency-selective scheme to read out the spin state of a set of Cr^{4+} compounds. Chapters 5 and 6 focused on the application polarization selection rules to realize spin-dependent pumping in order to read out Cr^{4+}(2,3-dimethyphenyl)$_4$ and appropriately designed Ce^{3+} complexes respectively.

Still, it is clear that we are only scratching the surface of what's possible with optically addressable molecular spins. For starters, we have only explored a small set of the accessible design space, examining only organometallic complexes of chromium, vanadium (see [99]), and cerium. The electronic structure framework presented here can be applied to other metal species or oxidation states, allowing the exploration of compounds with other spin multiplicities or energy level structures. Essentially, as long as complexes have long spin lifetimes and are sufficiently photostable, it should be possible to develop molecular analogs of other transition metal (molybdenum [39]) and rare earth ions (europium [101,114], praseodymium [115], erbium [42], holmium [116], and more) in solids. In addition, prior work in the field of spin-bearing color centers provides a robust roadmap of technical demonstrations that can be duplicated with molecular systems. Further maturation of optically addressable molecular spins may see their application in areas such as quantum sensing [117], hyperpolarization [118], and quantum information processing enhanced via molecular design.

Beyond merely emulating optically addressable spins in solid-state materials, I anticipate that the toolbox provided by chemistry will introduce new developments for spin qubits. Molecular spins offer unique features such as chemical tunability [52,100,119], the ability to produce larger scale arrays through self-assembly [55,56], and the ability to integrate multiple centers into larger quantum systems [54] that are typically inaccessible to solid-state spins. These systems should also be readily compatible with chemical functionalization methods (which can be challenging for solid-state spins [120]), permitting the exploration of new avenues in biophysics or enabling integration with conventional electronic or photonic [121] devices. Our development of an optical interface for this class of systems adds an additional experimental knob by which we can polarize and sensitively read-out molecular spins, even pushing down to the single molecule limit in the future.

Finally, beyond the scope of quantum technologies, I anticipate that the methods described in this thesis will also provide novel insights into physical chemistry. At the single molecule limit, the electronic spins hosted by these metal centers act as a highly sensitive probe of their local environment. Much like fluorescent single molecules, these spin-bearing molecules can also act as a probe of local phenomena such as intermolecular interactions or disorder. Furthermore, their metal-centered emission may offer some additional advantages, such as improved photostability or the ability to develop heterometallic complexes with multiple emissive sites.

Having outlined several potentially fruitful avenues for future work, one final question to consider is the broader technological outlook for this area (and perhaps quantum technologies more generally). In addition to meeting future technological requirements, several non-technical considerations will be equally critical. First, experimental tools and hardware will require increased robustness, scalability, and cost-effectiveness to meet the application constraints of advanced quantum information technologies. Secondly, we will need to train a diverse, skilled quantum workforce to implement and drive these technologies forwards [122]. Though promising corporate and startup activity exists, more companies will need to become early adopters of quantum technolo-

gies. Finally, these companies will need to realize significant value from this early adoption to drive future growth and investment in this area.

Though the road ahead may look challenging, I am optimistic that the quantum technology field will rise to the challenge. In addition to achieving the technological goals of today, I hope that we can find additional applications and use cases for quantum technologies far beyond what is imaginable now.

APPENDIX A

CERIUM OPTICAL SETUP

The experiments in Chapter 6 were performed in a custom-built confocal microscopy setup that provides polarization-resolved collection of Ce^{3+} optical emission. Samples were mounted on a custom-designed grounded coplanar waveguide printed circuit board to provide microwave access. A large permanent magnet on a motorized stage (Zaber X-LSM Series) could be used to provide a variable magnetic field.

A.1 Electronics

For pulsed experiments, a digital delay generator (Stanford Research Systems DG645) was used as a master clock and to produce multiple programmable pulses. A pulse pattern generator (Hewlett-Packard 81130A series) was operated in external trigger mode to provide ultrashort pulses for AC-coupled modulation of diode laser sources (see discussion below). For quasi-CW microwave experiments, a RF signal generator (Agilent E4400B) was used to produce microwave signals up to 1 GHz, which were square-wave modulated at a slow frequency to enable lock-in measurements.

A.2 Optics

The experimental setup can be broken down into several modular components as follows:

1. Imaging: enable finding and imaging crystalline samples
2. Polarization-resolved excitation: provides circularly-polarized σ_+ light to excite the sample.
3. Polarization-resolved collection: collect sample optical emission and resolve into σ_+ and σ_- components.
4. Detection - sensitively measure quasi-CW intensity, spectroscopic, or temporally-resolved properties of optical emission

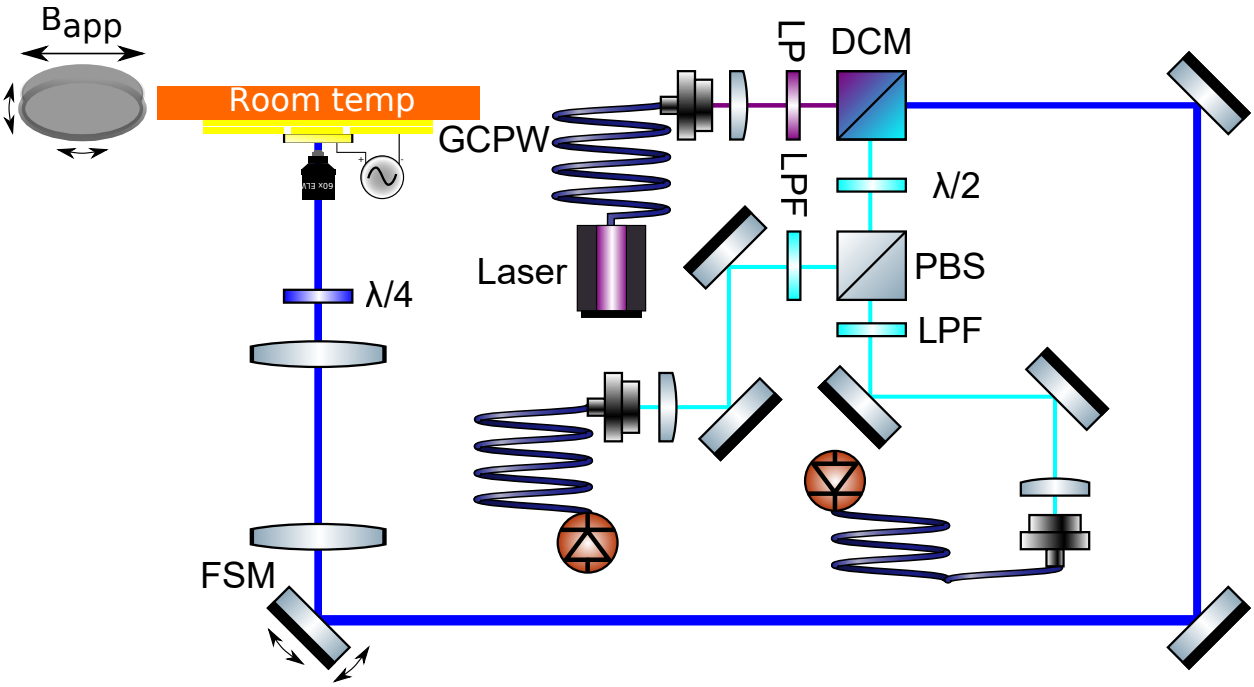

Figure A.1. Schematic of setup used for Cerium experiments. The experimental apparatus constitutes a laser scanning confocal microscope with circular polarization-selective excitation and collection. Drawings of optical components for the schematic were obtained from GW Optics ComponentLibrary set [123].

Imaging Sample imaging was accomplished using a long working distance objective (Nikon CFI S Plan Fluor ELWD 60XC) with a scanning confocal microscopy setup comprised of a $4f$-imaging pair and a fast galvo-galvo steering mirror (Newport FSM-300 Series). The optical imaging setup can be calibrated using a microscope slide hosting fluorescent microsphere beads (Polysciences StarLight series). Additionally, a flip-mounted pellicle combined with a white light source and imaging camera also permitted visual inspection of the sample.

Cage Construction For experimental flexibility, the remainder of the setup was constructed using cage optics, enabling the experimental apparatus to be moved to accommodate different imaging optics or sample configurations. Additionally, the use of cage components ensures mirror incidences close to 45° which is optimal for polarization-resolved experiments. By carefully designing and assembling the apparatus, a rigid cage optics assembly can be built that supports basic

confocal microscopy experiments. As a reference, we share a few suggestions that might assist with the design/build of future cage systems:

- Avoid long sections of cage rods where possible, as these can introduce flexion
- During assembly, ensure that all sets cage rods are matched in length and all screws are appropriate length
- Use threaded joints between cage elements wherever possible, and ensure that mates between cage rods are flush to ensure proper alignment
- Mate all connections between elements first to ensure proper alignment, then tighten all joints in a star pattern gradually until rigid connections are made

Excitation sources The experiments in Chapter 6 operated in two illumination modalities:

1. Continuous-wave laser operation - accomplished by steady-state operation of diodes in constant current mode.
2. Short (ns-scale) optical pulses - accomplished by fast current modulation of diodes above the lasing threshold. Some bias current is used to push the laser close to the lasing threshold, and then some additional modulation current is applied to transiently drive the laser above lasing threshold. Depending on the frequency response of the laser diode, this can be used to produce short (~ns-scale) optical pulses, often limited by the modulation pulse source.

Longer, μs-scale optical pulses of constant intensity may also be desirable for future hole-burning experiments (at cryogenic temperatures), but due to phenomena such as diode self-heating, these might be best accomplished by external modulation of the laser through an acousto-optic modulator (AOM), for example.

We used three separate diode / driver combinations for experiments:

1. QPhotonics QFLD-405-20S-PM diode (λ =402nm) and AlPhANov CCS-Std driver - provides an internal pulsed current modulation

2. Thorlabs LP405-SF30 diode (λ =405nm) and Thorlabs CLD1015 driver (AC-coupled current modulation)

3. Thorlabs LP462-MF1W(λ =462nm) and Thorlabs CLD1015 driver (AC-coupled current modulation) for Ce:YAG experiments.

All laser sources were coupled into a small-core multi-mode fiber to allow straightforward swapping of excitation sources without changing optical alignment. This fiber was then coupled into the experimental apparatus through a reflective collimator (Thorlabs RC02APC-F01) to allow a broad range of excitation wavelengths to be used.

Collection Polarization-resolved detection was accomplished by using a variable beamsplitter (Thorlabs VA5-PBS251), where the adjustable half waveplate defines the polarization basis for collection. Each arm (V and H) then hosts independent collection arms, comprising a removable magnetic filter insert (Thorlabs CP44F), steering mirror pairs, a cage-mounted variable z-stage (Thorlabs SM1Z) holding an aspheric lens (Thorlabs A280TM-A) to set the lens-fiber distances, and adjustable xy-flexure plates (Thorlabs CP1XY) to position the fiber and optimize collection into a light-tight, 50μm core multi-mode fiber. Collection into fiber is advantageous in that it allow different detectors to be used, without requiring realignment of optical setup.

The magnetic filter insert could be loaded with various long- and short-pass filters to spectrally select optical emission for a given experiment.

Detectors Depending on the experiments, we used one of the following detectors:

1. **High-sensitivity, differential measurements:** a low-noise, adjustable-gain photoreceiver (Femto OE-200-SI-FC), which provides an analog voltage used for direct digitization (National Instruments USB-6343 BNC) and lock-in detection (Signal Recovery 7265).

2. **High temporal resolution measurements:** single photon avalanche detectors (Excellitas SPCM-AQRH Series, -FC option), which provides the highest temporal resolution. The resulting TTL pulse edges can be counted (National Instruments USB-6343 BNC, Swabian

Instruments Time Tagger) or used for two-channel correlation measurements (Swabian Instruments Time Tagger).

3. **Spectrally-resolved measurements:** a Czerny-Turner spectrometer (Princeton Instruments PIXIS camera with SP2500 spectrometer), which provides spectroscopic information. The SP2500 grating turret holds three gratings with different grove spacings, allowing spectral acquisition across a variable range. Appendix D provides more details about the setup and optimization of spectroscopic hardware.

APPENDIX B

CHROMIUM OPTICAL SETUP

The experiments in Chapter 5 were performed in a custom-built confocal microscopy setup to provide time- and polarization-resolved excitation of Cr^{4+} molecular samples. Samples were placed in a custom-made closed-cycle cryostat with optical access (Montana Instruments) with a base temperature of < 4 Kelvin. The sample mount was a custom-designed, grounded coplanar waveguide printed circuit board with a low-loss, ultra-thin dielectric (.203mm thick Rogers 4350) matched to a 50Ω impedance to ensure good thermalization and efficient delivery of microwave pulses.

Microwave Electronics An arbitrary waveform generator (Tektronix AWG5000) served as the master clock for experiments and provides TTL outputs for modulation of optical and microwave signals. For microwave pulse generation, a vector signal generator (Stanford Research Systems SG396) outputs a constant frequency microwave drive signal, which was on/off modulated using a high-isolation RF switch (MiniCircuits ZASWA-2-50DR+). The modulated signal was then amplified using an RF amplifier (Mini Circuits) and delivered to the sample through the custom-built coplanar waveguide sample mount, using a through configuration with a matched termination RF dump outside the cryostat.

Excitation Experiments used time-gated and linearly-polarized off-resonant and resonant excitation sources.

Off-resonant excitation was provided by a 785nm laser diode (Thorlabs FPL785S-250) housed in a precision laser current driver (AlPhANov CCS-Std). This beam was time-gated with a fiber-coupled acousto-optical modulator (Gooch and Housego) to provide high optical extinction (>50 dB) and fast rise / fall times. Of note, the AlPhANov diode driver also provides direct pulsed current modulation of the diode, but in practice nonlinearities such as diode self-heating mean that external modulation is preferable to produce output laser pulses of constant power.

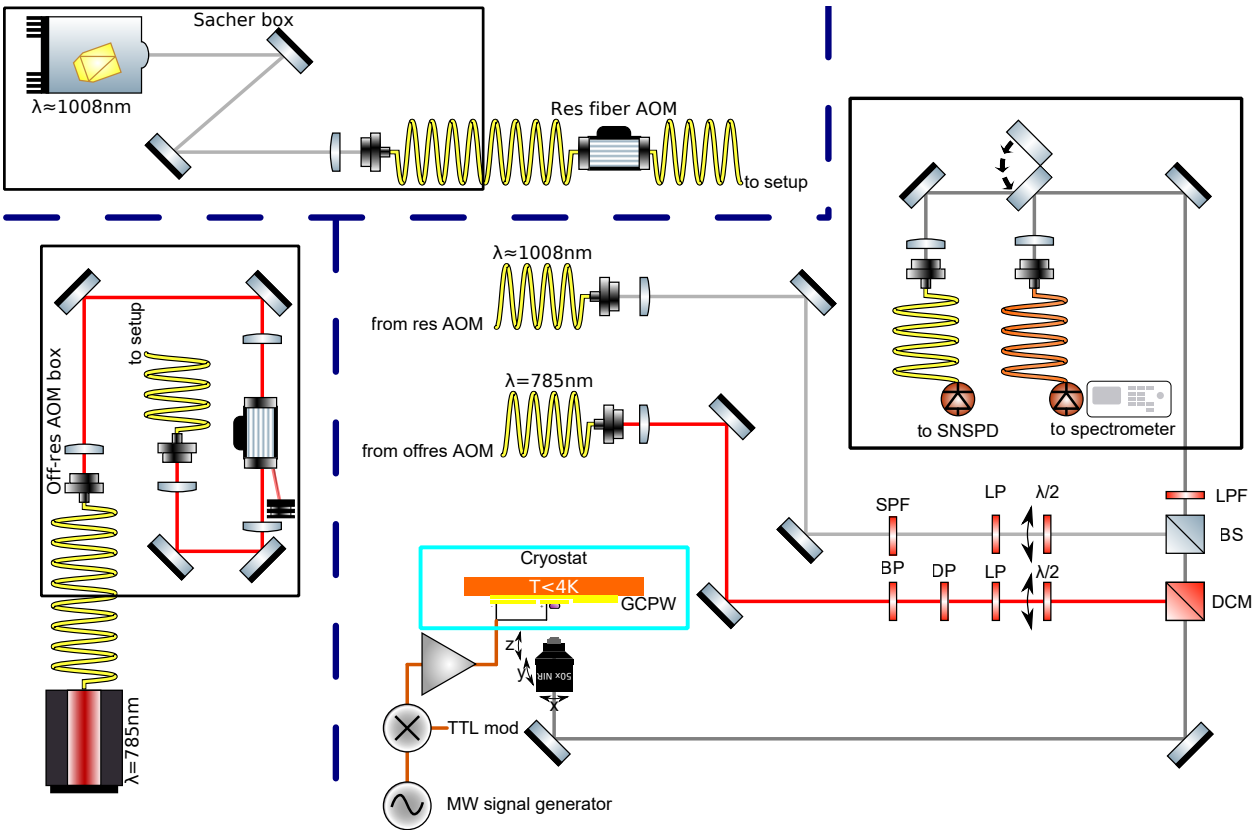

Figure B.1. Schematic of setup used for Chromium experiments. The experimental apparatus is divided up into modules for modulating the off-resonant laser, fiber coupling and modulating the resonant laser, and exciting the sample (with excitation polarization control) and collecting the resultant optical emission. Drawings of optical components for the schematic were obtained from GW Optics ComponentLibrary set [123].

The excitation beam was coupled into the experimental apparatus using a collimator (Thorlabs F280APC-780) and spectrally filtered using a bandpass stack (Thorlabs FESH0800 / Thorlabs FELH0750). To avoid polarization noise (resulting from the use of non-polarization-maintaining fiber) the beam passed through a depolarizer (Thorlabs DPP25-B) to randomize the polarization prior to passing through the linear polarizer (with the consequence that half the power is lost).

Resonant excitation was provided by a tunable diode laser with a Littman-Metcalf cavity configuration (Sacher LION), with a short-pass filter used to clean up the resulting output beam. This diode was coupled into single-mode fiber using a custom cage-component fiber launch (analogous to the multi-mode collection setup outlined below) for experimental convenience. In addition, this configuration allows monitoring of the output frequency using a wavemeter (Bristol 621A) and a scanning Fabry-Perot interferometer (Thorlabs SA200-8B) to verify single mode output.

For both beams, a linear polarizer (Thorlabs GTH10M-B) and a $\lambda/2$ waveplate (Thorlabs AHWP10M-980) mounted in a motorized rotation stage (Thorlabs PRM1Z8) provide control of the linearly-polarized excitation at the sample. The beams then pass through a window-corrected objective (Olympus LCPLN50XIR), to excite the sample and collect the resulting optical emission.

Collection For off-resonant excitation experiments, the resulting optical emission was filtered with a dichroic mirror (Semrock Di02-R980) and a long pass filter (Thorlabs FELH1000). For resonant excitation experiments, the excitation beam passed through a 50:50 plate beamsplitter, and the resonant laser scatter was rejected using an angle-tuned longpass filter. After passing through the filter set, the emission was steered using a mirror pair and collected into optical fiber using an aspheric lens. A motorized flip mirror (Thorlabs MFF101) allowed diversion of the beam into a light-tight, 50μm core fiber for using a home-built fiber launch. The launch was comprised of an aspheric lens (Thorlabs A280TM-B) held in a cage-mounted variable z-stage (Thorlabs SM1Z) which sets the lens-fiber distances, and an adjustable xy-flexure plates (Thorlabs CP1XY), holding the fiber, allowing precise lateral positioning of the fiber. To maximize total optical signal, multi-mode fiber collection was used for lock-in and spectroscopic experiments. For collection into

single-mode fiber, we used an aspheric lens combined with a FC-connectorized fiber launch system (Thorlabs MBT613D).

Detectors Depending on the experiments, we one of the following detectors:

1. a low-noise, adjustable-gain InGaAs photoreceiver (Femto OE-200-IN2-FC), which provides an analog voltage used for digitization (National Instruments USB-6343 BNC) and lock-in detection (Signal Recovery 7265).

2. Superconducting nanowire single photon detector (Single Quantum) which provides single photon detection in the NIR with high temporal resolution and low dark counts. This detector was located at the end of 100m of light-tight single-mode optical fiber. The resulting TTL pulses were then amplified (Single Quantum pulse amplifier) and split using a TTL pulse splitter (Pulse Research Labs PRL-414B), allowing for simultaneous counting (National Instruments USB-6343 BNC) or for correlation measurements to be performed (Swabian Instruments Time Tagger).

3. a Czerny-Turner spectrometer (Princeton Instruments PyLoN IR camera with SP2500 spectrometer), which provides spectroscopic information. The SP2500 grating turret holds three gratings with different grove spacings, allowing spectral acquisition across a variable range.

APPENDIX C

SIMULATION CODE

The code used for simulations in this thesis are available in the GitHub repositories indicated by the citations below.

C.1 Metal-Ion

The Metal-Ion Github repository [124] is a Python software package that was used for the electronic structure calculations presented in Chapter 2.

The heart of this software tool is the `metal_ion.py` file, which first enumerates the $|vSLJ\rangle$ states for a given electronic configuration. Next, the package can the compute the matrix elements / Hamiltonians for the electrostatic, spin-orbit, crystal field, and Zeeman interactions. These calculations leverage the spherical tensor formalism to determine the matrix elements of angular momentum eigenstates in terms of Wigner 3j symbols and reduced matrix elements. For computational efficiency (especially where many states are considered, such as the middle rows of the lanthanide series), precomputation and caching of results is used to prevent repeated calculation of computationally expensive matrix elements and Wigner symbols. The reduced matrix elements are constructed with the assistance of a digitized version [125] of the Nielson and Koster tables [68]. The electronic structure for a given metal ion can then be determined by numerically calculating the eigenvalues of the total system Hamiltonian.

The repository includes two files which provide examples of typical usage, and were used to generate the figures in Chapter 2.

1. `tanabe_sugano.ipynb` - calculates the Tanabe Sugano diagrams for $d^2 - d^8$ by considering the electrostatic and crystal field interactions.

2. `dieke.ipynb` - calculates the Dieke diagram for the Lanthanide series $f^1 - f^{14}$ by considering the electrostatic and spin-orbit interactions.

These methods can be extended to determine the splitting of various spectroscopic multiplets under symmetry lowering (introducing additional non-zero crystal field parameters) and magnetic fields (introducing Zeeman interaction).

C.2 QuTiP spin simulation

The Spin-Simulator Github repository [126] uses the QuTiP [78,79] software package to simulate the dynamics of a $S = 1$ spin under microwave drive field. The general setup is:

1. Define an initial polarized density matrix $\hat{\rho} = |0\rangle\langle 0|$

2. Define the system Hamiltonian as $H(t) = H_0 + H_1(t)$, where H_0 is the steady-state system Hamiltonian (incorporating the zero-field splitting and Zeeman interactions) and $H_1(t)$ is a time-dependent microwave drive field (which can be designed to match the pulse sequence for a particular experiment).

3. Incorporate decoherence in the form of collapse operators with $\hat{C_{\text{dephasing}}} = \sqrt{\frac{1}{T_2}} S_z$ and $\hat{C_{\text{depolarizing}}} = -i\sqrt{\frac{2}{T_1}} S_y S_z$. This form of depolarizing operator corresponds to the the $T = 0$ limit (as this forces all population into $|0\rangle$); a more phenomenological collapse operator would drive steady state populations to match a Boltzmann distribution. Though useful for phenomenological understanding, this model is imperfect in that it neglects coherent interactions between the central spin and the lattice spin bath. In principle, this could be modeled by adding in hyperfine interaction with multiple bath spins, but this would greatly increase simulation complexity.

The Lindblad master equation formalism is then used to simulate the time evolution of system observables S_z and S_z^2 (related to populations in $|0\rangle$ vs. $|\pm 1\rangle$ and corresponding to optical contrast).

APPENDIX D

SPECTROMETER

This appendix is adapted from a living version hosted at: Awschalom Group Wiki - Princeton Instruments Spectrometers

A spectrometer characterizes the spectral components of a light source. The only required components are (1) a dispersive optical element (a prism, for example) and (2) a detector sensitive to the wavelengths of interest. The dispersive optical element is used to separate light into its component wavelengths, which permits spectrally selective detection.

D.1 Czerny-Turner Spectrometer

The Princeton Instruments spectrometers typically used in our group use a Czerny–Turner design. In general, there is a tradeoff between spectral resolution and throughput, as a system with higher spectral resolution spreads a unit bandwidth over a larger number of detector pixels. Thus, it's best practice to iteratively adjust the measurement parameters that maximizes light intensity while maintaining sufficient spectral resolution to accurately characterize the input light source.

We can break down the system into its components and discuss a few of the system tradeoffs:

1. Input slit (B) - the image of the slit is mapped onto the detector. Narrowing the slit width decreases the size of the image and thus improves the spectral resolution. This increased spectral resolution comes at the expense of light throughput, as a narrower slit lets less light into the system.

2. Reflective mirrors - these collimate the input light prior to striking the grating (C) and focus the diffracted light on the detector (E). Reflective optics are used as they do not introduce any additional dispersion. Using reflective mirrors with larger focal lengths increases the spectral resolution, as the dispersed light is spread out over a larger range on the detector.

3. Grating - this serves as the dispersive optical element. A grating with a high spatial frequency (i.e. many grooves per unit length) offers high dispersion and thus high spectral resolution. Gratings are preferable to prisms as the dispersion is constant per wavelength (we will discuss this in more detail below)

4. Detector - you can think about the detector as a linear array of pixels, where each "x" position in the array corresponds to a different wavelength. It's important to use a detector that is sensitive to your input light source! We generally use two different types of detectors (silicon, visible light <400nm - 1100nm, depending on the specifics) and InGaAs (near infrared, 800nm - 2000+nm). The fabrication techniques for InGaAs detectors are less mature, so the detectors are typically a 1D linear array. Si has better manufacturing processes and thus high aspect ratio detectors (100x1300 or 400x1300) are used – spectral information is then determined by integrating over the "y" axis. These detectors are typically cooled using liquid nitrogen or a TEC to reduce dark counts (allowing for longer integration times).

The grating equation for a Czerny-Turner spectrograph is given by:

$$\frac{m}{d}\lambda = \sin(\alpha) + \sin(\beta) \tag{D.1}$$

where m is the diffraction order, d is the groove spacing, λ is the wavelength, and α (β) is the angle of the incident (exit) beam relative to the normal.

Note that this equation assumes the groove spacing is large relative to the wavelength. Note that 1200g/mm corresponds to ~ 833nm groove spacing, which explains why you don't see high density gratings that go far out into the NIR!

For $m = 0$ (i.e. the 0-th order diffraction), this relation is satisfied for all λ provided that $\alpha = \beta = 0$. Thus, at normal incidence, the diffraction grating just acts as a mirror (we use this property when aligning gratings later on).

Substituting in:

$$\alpha = \psi - \gamma/2, \text{ and } \beta = \psi + \gamma/2 \tag{D.2}$$

where γ is the inclusion angle and ψ is the grating rotation angle, we can reach the equation for the grating angle:

$$\psi = \arcsin\left(\frac{m\lambda}{2d\cos(\gamma/2)}\right) \tag{D.3}$$

From this, we can extract some important information:

1. Harmonics can be picked up at higher order diffractions as they have the same grating angle (i.e. $(2m)\lambda = m(2\lambda)$) – **this can introduce spurious signals into spectra and is something to be aware of!**

2. Decreasing the groove spacing increases the grating angle (so higher groove density means less light will fit on the image sensor) There's a more detailed set of calculations on this and why the Czerny-Turner configuration is good here.

D.2 Princeton Instruments Spectroscopy Hardware

Having introduced the general principles of spectroscopy and the different components of a spectrometer, this next section is more specific to Princeton Instruments hardware and hopefully identifies some of the quirks / challenges of setting up and using these systems.

Princeton Instruments separates the hardware into a spectrograph, which has the gratings / mirrors / input slit, and a camera, which is typically cooled to improve performance.

Useful links / support articles: Manuals: Note that as of this writing (11/2020), Chrome no longer supports ftp browsing, but you should be able to browse these directories with other browsers such as Firefox. The information is divided up – spectrographs are under Acton and cameras under PrincetonInstruments

Wavelength calibration chart

Gratings

Calculators: Grating dispersion calculator: This calculator allows you to determine spectral resolution and range for a given combination of spectrograph / grating spacing / camera / slit width. Can be useful for figuring out what gratings correspond to what spectral range in a given frame.

Signal to noise calculator: :This allows calculation of the SNR for a given input photon flux, based on detector quantum efficiency, exposure time, and amplifier readout modes for different detector hardware

Software downloads: Princeton Instruments

Monocontrol

D.2.1 Getting Started

You can roughly divide the setup process into a few steps:

1. Connect software to spectrograph and camera
2. Initial alignment (ideally using an existing grating):
   (a) Camera focus and orientation
   (b) Light input - fiber input, lens pair focus
3. Replace and realign gratings (if necessary)
4. Calibrate gratings using white light source

D.2.1.1 General quirks

1. **The older cameras only support 32-bit operating systems (and may require a dedicated computer to operate them – please update if there's a workaround!). Newer cameras**

also support 64-bit operating systems, but our Winspec license is 32-bit, so you may want to use a separate computer for that reason. There's a 64-bit license for Lightfield, but a single license key runs about $2-2.5k (the physical key can be removed and shared between computers, they just can't operate simultaneously).

2. Some cameras (Pylon series) have separate modules hosting the camera and a controller unit. According to the manual, the controller units and the camera must match for proper operation

3. It appears that there are different standards used for mounting cameras by different spectrographs. You may need to contact Princeton Instruments to get an adapter plate to mount a given camera onto the spectrograph.

4. Some cameras have a shutter which blocks light when the exposure is not running. Different types of shutters may expect different TTL signals to open the shutter. If using a shutter, make sure that the shutter is doing what you think it is (i.e. your counts should increase linearly with exposure time if this is configured correctly). There should be buttons with a number on the back of the camera controller which change between different shutter signal conventions.

D.2.1.2 Connecting software

You'll need to install either Winspec or Lightfield:

- We have a Winspec license on tank, but it requires a 32-bit computer.

- Lightfield requires a license (there is a 60-day trial to demo it) but works on 64-bit machines. The 64-bit license doesn't appear to work with older camera hardware, however.

Once you have the software installed, you should be able to connect to the spectrograph through serial (RS-232) and the camera (or camera controller box) using USB.

If everything's working correctly, you should be able to take an exposure with the camera, and change the nominal center wavelength of the grating (you should be able to hear the motor moving).

D.2.1.3 Initial alignment - camera

There are two degrees of freedom that need to be aligned to optimize the spectra resolution, the focal point and the rotational alignment.

Unfortunately, Princeton Instruments doesn't seem to have done a great job of standardizing this process of mounting cameras, so the specific details of this process may vary a lot. In general, you want to:

1. Mount the camera using some adapter plate.

2. Loosely secure the camera so it's held securely, but the angular orientation and focal plane can be carefully adjusted

3. Use a bright, spectrally narrow source (I recommend fiber coupling the calibration lamp) at the input.

   (a) You should be able to just put the bare fiber up on the calibration source and get enough signal to do initial alignment

   (b) Do a coarse alignment of the input port, so the input light is approximately focused on the center of the slits. We will improve this later on.

   (c) Open the slit to be fairly wide and run a short exposure, and increase the integration time until you see some signal. Once you can see some signal in a short amount of time, you're ready to start aligning. You can decrease the exposure or close the slit if you start saturating the detector

4. Make sure that the grating is aligned such that the first order diffraction peak hits the center of the detector. We'll worry about the wavelength calibration later on.

5. You should be able to go to some center wavelength and see a series of sharp peaks. As you bring the spectrum into focus, the peaks should sharpen – make sure that you're reached the optimum and not just the end of travel. Some of the instruments have a large thumbwheel which allows you to finely push the camera out of the spectrograph body.

6. By adjusting the angular orientation of the camera you should also be able to:

   (a) Sharpen the lines(1D array InGaAs CCD

   (b) Align the image of spectral lines to match the xy-alignment of the CCD pixels (2D Si CCD) so the lines are vertical.This will give the sharpest spectra when integrating over the "y" axis (or some region thereof).

7. Tighten the camera so the camera position is fixed and well-secured.

D.2.1.4 Initial alignment - light input

Now that you have a sharp set of peaks, you want to maximize the light coupled into the spectrometer. To do this, you just need to get the input light focused on the center of the entrance slit:

1. Make the entrance slit as small as possible, while still having a short enough integration time to have feedback

2. Optimize the xy position of the fiber and the two lenses to maximize the intensity

3. Repeat the optimization iteratively until the slit is almost completely closed. If this is done correctly, you should also be able to see that the beam is tightly focused at the input slit.

4. You should be able to acquire good spectra of the calibration lamp with very short acquisition times

D.2.1.5 Replace and realign gratings

Depending on the experiment you want to run, the gratings in the spectrograph may not be well suited to a particular application. You can swap them out for ones with a different blaze wavelength or resolution. The challenging part is getting the grating to be realigned, you need to get the both the zeroth order (i.e normal reflection) diffraction peak and first order diffraction peaks to be approximately centered on the detector when the turret is rotated. For this reason, I recommend performing this step with a laser that's known not to have any spurious harmonics (HeNe works well). The higher order diffraction peaks can make alignment very confusing, as local optima on the camera may just be higher order diffraction peaks.

Please see the instructions on adding or interchanging gratings, but a little additional color commentary:

- Make sure that you update the spectrograph and tell it which gratings it has installed. This can be done using the MonoControl software (you should be able to find the most up to date from the Princeton Instruments ftp)
- **Gratings are very sensitive to dust / particles. Please keep spectrometers closed except for when adjusting, and try to avoid talking / breathing on them. As we now know (thanks 2020), these activities produce lots of particles which can have nasty consequences. Make sure to store them in a manner that the grating surface will be protected.**
- **Only make very small adjustments to the zero adjusting and height adjusting screws when removing the grating.** Ideally, you can reverse this adjustment when loading the new grating so it is close to aligned when it is put back into the turret.
- The alignment is very hard because the grating mount design is poor and the degrees in freedom are very closely coupled. This makes it very hard to return back to the original optimum if you make large adjustments

- The grating is affixed onto the metal posts with very fragile epoxy. Any aggressive tightening or adjustment of screws can easily break the metal posts off the grating
  - If the posts break off, you can reaffix them with vacuum epoxy and carefully clamping them for approximately 24 hours.This is hard and I would recommend not doing this in the first place.
- The manual talks about also adjusting the tangent adjusting screw, but I think this one is generally useless (and often inaccessible for the third grating). So I wouldn't worry much about it.
- You can buy new gratings from PI or from Richardson, just make sure they are the right size and have the correct mounting points.

D.2.1.6 Calibration

At this point, you should have it so that:

1. The camera is well aligned so the calibration source gives sharp spectra
2. The input port is aligned so your light signal is well aligned to the center of the slits and appropriately focused to match the focal length of the first mirror
3. All gratings are aligned such that the 0th (i.e. 0nm reflection) and 1st order diffractions are well centered on the detector.
4. Give yourself a pat on the back for making it this far. I'm guessing it wasn't easy.
5. You're now ready to calibrate the spectrometer in order to accurately determine the wavelength axis for the instrument.
6. We'll cover calibration in the day-to-day operation section, though the calibration shouldn't need to be performed frequently.

D.2.2 Day-to-day operation

Congrats - you got the spectrometer working (or found one that's already set up)! Here's a primer on the day-to-day operation stuff.

Warnings!

- The cameras are very sensitive and not designed to handle large input powers. If you want to characterize a bright source (especially a monochromatic source like a laser) you should try to attenuate it down to a reasonable level.
- If your input source is saturating the detector pixels, you should decrease the source intensity or the integration time to avoid clipping
- Be careful when working with LN2, especially for cameras located on the hanging table.

D.2.2.1 Cooling

LN2 cooled cameras Most cameras in the lab use liquid nitrogen to cool the sensor down to about -100°C to minimize dark counts. As the spectrometer is sensitive to the alignment of the camera, it's best to fill the camera with the minimal amount of potential jostling. One effective procedure is to do the following:

1. **Wear cryogenic gloves and safety glasses to when working with liquid nitrogen. If filling a camera on the hanging table, check for objects below the camera and notify others working in the lab.**
2. Start filling one of the small (~4L) transfer dewars with liquid nitrogen, we usually keep one in the hallway outside sample prep.
3. Once the transfer dewar is full, tilt the transfer dewar so the liquid nitrogen is in contact with the neck of the transfer dewar. Some liquid nitrogen will start to boil out, so it's best

to do this over a wider necked dewar to catch the escaping LN2. The purpose of this is to thermalize the neck of the dewar to minimize boiling of the LN2 when filling the camera.

4. Once the LN2 can be poured out in a steady stream, the dewar neck has been thermalized. You can top off the transfer dewar and prepare to fill the camera.

5. Remove the stopper from the camera and slowly pour the LN2 into the camera dewar. It may boil momentarily as the neck rethermalizes, but you should have a stable stream of LN2 that can be carefully poured into the camera without too much spilling. As you fill the camera, you may see LN2 bubble up to the top momentarily, giving the impression that the camera may be full. This is due to LN2 boiling while thermalizing the camera dewar. Wait momentarily and keep filling the camera until there's a stable LN2 bath that boils near the top of the dewar.

6. Put the stopper back in and close, being careful to watch out for any LN2 spills.

7. Take short acquisitions (~1s) as the camera cools down to minimize background (we don't know if / why it actually works, please update if you have an explanation or evidence to the contrary)

8. The camera should reach the temperature setpoint within about 4 hours. If it doesn't reach about -100∘C, there may be a problem with the camera vacuum, see the LN Vacuum Restoration note for instructions on how to address this. The camera should stay cold for at least 24 hours - it may be best to top it off at approximately the same time each day if using frequently to avoid waiting for cooldown times.

TEC cooled cameras Some of the newer Si detectors have a TEC which can cool down the detector to about -75°C. Note that the TEC does not run unless the software is running and connected to the camera. The camera cools down fairly quickly, but you may want to keep the software open in the background to avoid having to wait to acquire new spectra.

D.2.2.2 Calibration

You'll need a spectroscopic light source with a set of sharp lines at some known spectral wavelength, we have a nice source in lab for this. **I would highly recommend doing this by butt coupling your input fiber to the calibration source – if you remove the coupling lenses it can actually shift the beam laterally on the detector and introduce a small amount of error in the wavelength calibration when you put the lens assembly back on.**

Winspec The big challenge is identifying which spectral lines are which (noting that, depending on the wavelength range of interest, you could be measuring higher order diffraction peaks). Generally, you should look for a series of lines with a distinctive intensity pattern that appear to match the reference source, the Intellical wavelength reference chart is handy for this. For example, the closely spaced, you could try to find the similar intensity lines at 576/579nm and use those as one point of reference. Then follow the offset / adjust procedure until the calibration gives the correct locations for the different spectral lines.

Lightfield The Intellical procedure makes this a snap. Highly recommended and very easy to use. You more or less click "go" with the white light source and it does it.

D.2.2.3 Optimization

Some unsolicited recommendations:

- Background subtraction - acquire a baseline signal with your light source of interest "off". This signal is then stored in memory and subtracted from data. Useful especially for long integration times
  - Si cameras can have low dark count rates, so for reasonably short exposures, just a static background works well

  - For InGaAs cameras, the dark count rate is fairly high so you'll want to acquire a new background file each time you change settings like exposure time, grating center wavelength, or slit width
  - Lightfield's background subtraction takes 6x (maybe 5?) the exposure time, while Winspec's only runs for a single exposure duration.

- Step and glue mode seems to work reasonably well in Lightfield to get high spectral resolution over larger scan ranges

REFERENCES

[1] P. Benioff, *Journal of Statistical Physics* **22**, 563 (1980).

[2] R. P. Feynman, *International Journal of Theoretical Physics* **21**, 467 (1982).

[3] M. Mohseni, *et al.*, Commercialize quantum technologies in five years (2017).

[4] G. Kalai, *arXiv* (2019).

[5] M. Dyakonov, The Case Against Quantum Computing (2018).

[6] J. Pritchard, S. Till, UK Quantum Technology Landscape, *Tech. rep.* (2014).

[7] G. E. Moore, *Electronics* pp. 114–117 (1965).

[8] T. Wright, *Journal of the Aeronautical Sciences* **3**, 122 (1936).

[9] L. M. Smith, *et al.*, *Nature* **321**, 674 (1986).

[10] F. S. Ujager, S. M. Zaidi, U. Younis, *7th International Symposium on High-Capacity Optical Networks and Enabling Technologies, HONET 2010* (2010), pp. 107–111.

[11] H. Lee, *et al.*, Lasers in additive manufacturing: A review (2017).

[12] M. Kjaergaard, *et al.*, Superconducting Qubits: Current State of Play (2020).

[13] W.-L. Ma, *et al.* (2021).

[14] C. D. Bruzewicz, J. Chiaverini, R. McConnell, J. M. Sage, *Applied Physics Reviews* **6**, 021314 (2019).

[15] L. Henriet, *et al.*, *Quantum* **4**, 327 (2020).

[16] S. Slussarenko, G. J. Pryde, Photonic quantum information processing: A concise review (2019).

[17] Y. Chu, *et al.*, *Science* **358**, 199 (2017).

[18] K. J. Satzinger, *et al.*, *Nature* **563**, 661 (2018).

[19] A. Chatterjee, *et al.*, *Nature Reviews Physics* **3**, 157 (2021).

[20] F. Arute, *et al.*, *Nature* **574**, 505 (2019).

[21] H. S. Zhong, *et al.*, *Science* **370**, 1460 (2021).

[22] J. Yin, *et al.*, *Science* **356**, 1140 (2017).

[23] M. Pompili, *et al.*, *Science* **372**, 259 (2021).

[24] G. AI Quantum, *Science* **369**, 1084 (2020).

[25] S. Wengerowsky, S. K. Joshi, F. Steinlechner, H. Hübel, R. Ursin, *Nature* **564**, 225 (2018).

[26] G. Kucsko, *et al.*, *Nature* **500**, 54 (2013).

[27] F. Bloch, *Physical Review* **70**, 460 (1946).

[28] E. L. Hahn, *Physical Review* **80**, 580 (1950).

[29] A. M. J. Zwerver, *et al.* (2021).

[30] S. Baumann, *et al.*, *Science* **350**, 417 (2015).

[31] S. Geschwind, R. J. Collins, A. L. Schawlow, *Physical Review Letters* **3**, 545 (1959).

[32] A. Gruber, *et al.*, *Science* **276**, 2012 (1997).

[33] W. Pfaff, *et al.*, *Science* **345**, 532 (2014).

[34] M. Fukami, *et al.*, *Physical Review Applied* **12**, 014042 (2019).

[35] A. O. Sushkov, *et al.*, *Nano Letters* **14**, 6443 (2014).

[36] G. Wolfowicz, *et al.*, *Nature Reviews Materials* pp. 1–20 (2021).

[37] S. Kanai, *et al.* pp. 1–24 (2021).

[38] W. F. Koehl, *et al.*, *Physical Review B* **95**, 035207 (2017).

[39] T. Bosma, *et al.*, *npj Quantum Information* **4**, 1 (2018).

[40] G. Wolfowicz, *et al.*, *Science Advances* **6**, eaaz1192 (2020).

[41] M. Zhong, *et al.*, *Nature* **517**, 177 (2015).

[42] A. M. Dibos, M. Raha, C. M. Phenicie, J. D. Thompson, *Physical Review Letters* **120**, 243601 (2018).

[43] R. Kolesov, *et al.*, *Nature Communications* **3**, 1 (2012).

[44] P. Siyushev, *et al.*, *Nature Communications* **5**, 1 (2014).

[45] D. G. Cory, A. F. Fahmy, T. F. Havel, *Proceedings of the National Academy of Sciences of the United States of America* **94**, 1634 (1997).

[46] N. A. Gershenfeld, I. L. Chuang, *Science* **275**, 350 (1997).

[47] D. G. Cory, M. D. Price, T. F. Havel, *Physica D: Nonlinear Phenomena* **120**, 82 (1998).

[48] L. M. Vandersypen, *et al.*, *Applied Physics Letters* **76**, 646 (2000).

[49] L. M. Vandersypen, *et al.*, *Nature* **414**, 883 (2001).

[50] W. S. Warren, N. Gershenfeld, I. Chuang, *Science* **277**, 1688 (1997).

[51] G. Aromí, D. Aguilà, P. Gamez, F. Luis, O. Roubeau, *Chemical Society Reviews* **41**, 537 (2012).

[52] M. J. Graham, J. M. Zadrozny, M. S. Fataftah, D. E. Freedman, *Chemistry of Materials* **29**, 1885 (2017).

[53] E. Coronado, Molecular magnetism: from chemical design to spin control in molecules, materials and devices (2020).

[54] S. von Kugelgen, *et al.*, *Journal of the American Chemical Society* **13**, jacs.1c02417 (2021).

[55] A. Urtizberea, *et al.*, *Advanced Functional Materials* **28**, 1801695 (2018).

[56] T. Yamabayashi, *et al.*, *Journal of the American Chemical Society* **140**, 12090 (2018).

[57] J. Wrachtrup, C. Von Borczyskowski, J. Bernard, M. Orritt, R. Brown, *Nature* **363**, 244 (1993).

[58] J. Köhler, *et al.*, *Nature* **363**, 242 (1993).

[59] W. P. Ambrose, W. E. Moerner, *Nature* **349**, 225 (1991).

[60] V. Ahtee, *et al.*, *Journal of Modern Optics* **56**, 161 (2009).

[61] R. Lettow, *et al.*, *Phys Rev. Lett.* **104**, 123605 (2010).

[62] R. Chikkaraddy, *et al.*, *Nature* **535**, 127 (2016).

[63] P. Lombardi, *et al.*, *ACS Photonics* **5**, 126 (2018).

[64] H. Bethe, *Annalen der Physik* **395**, 133 (1929).

[65] M. P. Hehlen, M. G. Brik, K. W. Krämer, *Journal of Luminescence* **136**, 221 (2013).

[66] K. E. Hyde, *Journal of Chemical Education* **52**, 90 (1975).

[67] B. N. Figgis, *Comprehensive Coordination Chemistry 1* (1987), pp. 213–279.

[68] C. Nielson, G. F. Koster, *Spectroscopic Coefficients for the pn, dn, and fn Configurations* (MIT Press, 1963).

[69] B. G. Wybourne, Magnetic and Hyperfine Interactions in Atoms, Ions and Crystals c, *Tech. rep.*, Institute of Physics, Nicholas Copernicus University, Toruń (2003).

[70] R. Boča, *Structure and Bonding* **117**, 1 (2005).

[71] M. Rotter, *et al.*, Symmetry considerations for Crystal Field Parameters (2013).

[72] Y. Tanabe, S. Sugano, *Journal of the Physical Society of Japan* **9**, 766 (1954).

[73] R. J. Lancashire, Tanabe-Sugano diagrams via spreadsheets (2006).

[74] B. N. Figgis, *Ligand Field Theory and Its Applications* (Wiley-VCH, New York, 2000).

[75] C. J. Ballhausen, *Introduction to ligand field theory* (McGraw-Hill, New York, 1962).

[76] G. H. Dieke, H. M. Crosswhite, B. Dunn, *Journal of the Optical Society of America* **51**, 820 (1961).

[77] T. Kornher, *et al.*, *Physical Review Letters* **124**, 170402 (2020).

[78] J. R. Johansson, P. D. Nation, F. Nori, *Computer Physics Communications* **183**, 1760 (2012).

[79] J. R. Johansson, P. D. Nation, F. Nori, *Computer Physics Communications* **184**, 1234 (2013).

[80] R. Mirzoyan, N. P. Kazmierczak, R. G. Hadt, *Chemistry - A European Journal* (2021).

[81] A. M. Ariciu, *et al.*, *Nature Communications* **10**, 1 (2019).

[82] L. Escalera-Moreno, N. Suaud, A. Gaita-Ariño, E. Coronado, *Journal of Physical Chemistry Letters* **8**, 1695 (2017).

[83] M. Atzori, *et al.*, *Journal of the American Chemical Society* **139**, 4338 (2017).

[84] M. S. Fataftah, *et al.*, *Chemical Science* **10**, 6707 (2019).

[85] H. Seo, *et al.*, *Nature Communications* **7**, 1 (2016).

[86] A. Ardavan, *et al.*, *Physical Review Letters* **98**, 057201 (2007).

[87] J. M. Zadrozny, J. Niklas, O. G. Poluektov, D. E. Freedman, *ACS Central Science* **1**, 488 (2015).

[88] F. Lombardi, *et al.*, *Science* (2019).

[89] M. Shiddiq, *et al.*, *Nature* **531**, 348 (2016).

[90] K. C. Miao, *et al.*, *Science* **369**, 1493 (2020).

[91] E. M. Purcell, *Physical Review* (American Physical Society, 1946), vol. 69, p. 674.

[92] W. P. Ambrose, T. Basché, W. E. Moerner, *The Journal of Chemical Physics* **95**, 7150 (1991).

[93] V. M. Acosta, *et al.*, *Physical Review Letters* **108**, 206401 (2012).

[94] T. Schröder, *et al.*, *Nature Communications* **8**, 1 (2017).

[95] C. P. Anderson, *et al.*, *Science* **366**, 1225 (2019).

[96] M. Kasha, Characterization of electronic transitions in complex molecules (1950).

[97] M. A. El-Sayed, *The Journal of Chemical Physics* **38**, 2834 (1963).

[98] M. L. Goldman, *et al.*, *Physical Review B - Condensed Matter and Materials Physics* **91**, 165201 (2015).

[99] M. S. Fataftah, *et al.*, *Journal of the American Chemical Society* **142**, 20400 (2020).

[100] S. L. Bayliss, *et al.*, *Science* **370**, 1309 (2020).

[101] D. Serrano, *et al.* (2021).

[102] R. M. Macfarlane, *The Journal of Chemical Physics* **47**, 2066 (1967).

[103] J. J. Chen, M. G. Zhao, *physica status solidi (b)* **143**, 647 (1987).

[104] R. Kolesov, *et al.*, *Physical Review Letters* **111**, 120502 (2013).

[105] J. D. Rinehart, J. R. Long, Exploiting single-ion anisotropy in the design of f-element single-molecule magnets (2011).

[106] L. J. Mueller, *Concepts in Magnetic Resonance Part A: Bridging Education and Research* **38 A**, 221 (2011).

[107] P. Mintun, PeterMintun/Ce-photophysics.

[108] H. R. Lewis, *Journal of Applied Physics* **37**, 739 (1966).

[109] P. J. Alonso, J. I. Martínez, *Journal of Magnetic Resonance* **255**, 1 (2015).

[110] X. L. Zheng, *et al.*, *Angewandte Chemie - International Edition* **46**, 7399 (2007).

[111] Y. Qiao, *et al.*, *Journal of the American Chemical Society* **140**, 4588 (2018).

[112] Y. Qiao, T. Cheisson, B. C. Manor, P. J. Carroll, E. J. Schelter, *Chemical Communications* **55**, 4067 (2019).

[113] D. A. Hopper, H. J. Shulevitz, L. C. Bassett, Spin readout techniques of the nitrogen-vacancy center in diamond (2018).

[114] K. S. Kumar, *et al.*, *Nature Communications* **12**, 1 (2021).

[115] K. Xia, *et al.*, *New Journal of Physics* **22**, 073002 (2020).

[116] T. Boonyarith (2017).

[117] C. L. Degen, F. Reinhard, P. Cappellaro, *Reviews of Modern Physics* **89** (2017).

[118] J. P. King, *et al.*, *Nature Communications* **6**, 1 (2015).

[119] M. J. Graham, C. J. Yu, M. D. Krzyaniak, M. R. Wasielewski, D. E. Freedman, *Journal of the American Chemical Society* **139**, 3196 (2017).

[120] L. V. H. Rodgers, *et al.* (2021).

[121] A. Gopinath, *et al.*, *Science* **371** (2021).

[122] C. D. Aiello, *et al.*, *Quantum Science and Technology* **6**, 030501 (2021).

[123] A. Franzen, ComponentLibrary (2006).

[124] P. J. Mintun, PeterMintun/Metal-Ion (2022).

[125] B. R. Judd, Text Files of the Multi-Electron Coefficients of Fractional Parentage for p, d, and f Electrons, *Tech. rep.* (2004).

[126] P. J. Mintun, PeterMintun/Spin-Simulator: QuTip simulation of spin dynamics (2022).